THE CAVITY-EMBEDDED-COOPER PAIR TRANSISTOR

A Thesis

Submitted to the Faculty

in partial fulfillment of the requirements for the

degree of

Doctor of Philosophy

in

Physics

by

Fei Chen

DARTMOUTH COLLEGE

Hanover, New Hampshire

May 2013

Examing Committee:

_____

(Chair) Alexander J. Rimberg

_____

Miles P. Blencowe

_____

Kevin Wright

_____

Joachim Ankerhold

_____

F. Jon Kull, Ph.D.
Dean of Graduate Studies

Abstract

Nearly eight decades after Erwin Schrödinger proposed his famous cat paradox, the boundary between classical and quantum physics is becoming accessible to experimental study in condensed matter systems, in which macroscopic and microscopic degrees of freedom interact with each other. The cavity-embedded-Cooper pair transistor (cCPT) is an ideal candidate for such a study in that it is not only strongly and intrinsically nonlinear but also fully quantum mechanical.

A novel technique, based on the circuit quantum electrodynamics architecture, is first introduced for applying a dc bias to a high-Q superconducting microwave cavity. The development and investigation of the cCPT system, in which a Cooper pair transistor acting as a single artificial atom is directly coupled to an on-chip dc-biased high-Q resonator, is then presented. Self-oscillations in the cCPT, internally driven by the ac Josephson effect, demonstrate the strong and phase coherent coupling between matter and light in the cCPT. Meanwhile, photons continually produced by the system are collected and characterized by quantum state tomography, which indicates the non-classical nature of the emitted light and the nonlinear quantum dynamics of the cCPT system.

Acknowledgements

“ Even with these dark eyes, a gift of the dark night

I go to seek the shining light. ”

Gu Cheng, *One Generation*

I have imagined many times how I would finish this dissertation by writing the acknowledgements, which are often the most enjoyable part when I read other people's theses. On a typical rainy spring day in the nicest town of New England, the time has finally come for me. It is not without some nostalgia that I start to thank people who made my thesis possible, and prepare to hand it in at the end of a seven-year long journey.

First, I am very grateful to have the opportunity to work towards my Ph.D. degree under the guidance of Prof. Alex Rimberg. Alex did not only teach me practical research skills, but more amazingly also always provided me ingenious ideas and abundant optimism indispensable for doing cutting-edge research.

I would also like to thank Prof. Miles Blencowe, who certainly became my second advisor. The physical interpretations presented in this thesis would not exist without his marvelous work in the theoretical front.

Over the last six years, I was fortunate enough to work with a diverse group of graduate students and postdoctoral researchers. Juliang Li gave me a tremendous lift in the device fabrication and the experimental setup as soon he joined the lab. As I began running the

cCPT experiments, Joel Stettenheim helped me enormously in operating and diagnosing the dilution refrigerator, showed me the electrical measurement techniques. Feng Pan, Zhongqing Ji, Mustafa Bal, Weiwei Xue and Tim Gilheart led me into the dark arts of fabrication and flawless design of microstructures, when I first joined the lab. I also enjoyed conversations with Mingyun Yuan, Zhen Yang and Chunyang Tang about physics and beyond.

The acknowledgments would not be complete without thanking my parents for their twenty-nine years of wholehearted love and support. Also, I would never have made it through without all the friends I met at Dartmouth and Tsinghua.

Years from now, even if I could not recall the details of this dissertation, one thing I would remember for sure is the amusing incident occurred during my thesis defense. Fifteen minutes into my presentation, the fire alarms of Wilder all went on. The entire building evacuated. The firefighter soon came and left. Everyone went back and I continued my talk on Josephson effects...

Contents

List of Tables

List of Figures

Chapter 1

Introduction

1.1 Quantum-to-Classical Transition

Ever since the 1920s, quantum mechanics has been developed to describe the behavior of the microscopic objects, such as atoms and molecules, which could not otherwise be explained by classical physics. The tremendous success of quantum mechanics over the past century, which lays the foundation of modern technology and the information era, has led to the general belief that it is the fundamental theory of the world. Yet the macroscopic world, composed of atoms and molecules, is well-described by Newton's laws of motion. In many ways, quantum and classical physics are fundamentally incompatible, which perplexed the pioneers of quantum mechanics and their followers, since the advent of the quantum theory and even until today. If quantum physics is really the fundamental theory of our world, then the Newtonian mechanics should emerge from the underlying

quantum physics as an object becomes more macroscopic – the so-called quantum-to-classical transition (QCT).

In 1935, Erwin Schrödinger [1] proposed a famous thought experiment, i.e. Schrödinger's cat, to illustrate the problem of quantum mechanics being applied to everyday objects. This paradox raised questions about whether quantum mechanics breaks down for the macroscopic world. Unlike the smooth transition between special relativity and classical mechanics, the boundary between quantum and classical physics is not clear and the QCT is much more complicated. This section follows the discussion in Bhattacharya *et al.* [2].

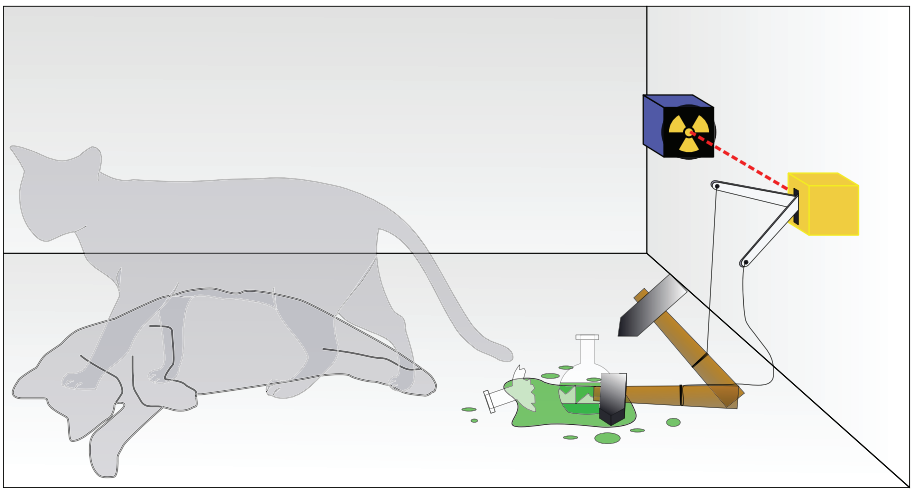

FIGURE 1.1: Schrödinger's cat: a cat, a flask of lethal poison, and a radioactive source are placed in a sealed box. Once triggered by the decay of a radioactive atom, the flask is shattered, releasing the poison that kills the poor cat. The Copenhagen interpretation [3] of quantum mechanics implies that after closing the box for a while, before one reopens it, the cat is simultaneously alive and dead. Yet, when one looks inside the box, one finds the cat either alive or dead, not alive and dead at the same time. [4]

To understand the origin of the incompatibility between classical and quantum physics, let us review the foundation of Newtonian physics. The motion of a classical particle is

governed by Newton's equations:

$$\dot{x} = \frac{p}{m} \tag{1.1}$$

$$\dot{p} = F(x,t) = -\partial_x V(x,t) \tag{1.2}$$

where V is the potential and F is the force on the particle. The evolution of the classical dynamics of this particle is determined by these two equations together. In phase space, the state of a classical particle at any given time corresponds to a point and its motion during a time interval corresponds to a trajectory.

In contrast, the state of a quantum particle can not be described by a point with a definite position and a definite momentum in phase space, because of the Heisenberg uncertainty principle. While classical mechanics deals with trajectories in phase space, quantum mechanics is intrinsically probabilistic. The quantum state of a particle can only be described by some kind of quasi-probability density distribution in phase space. The Wigner function the probability distributions earliest introduced in quantum mechanics and is defined as [5],

$$W(x,p) = \frac{1}{h}\int e^{-ipx'/\hbar}\psi(x+x'/2)\psi^*(x-x'/2)dx' \tag{1.3}$$

where $\psi(x)$ is the wave function. The integral of the Wigner function over position x gives the probability density for momentum p, and the integral over p gives the probability density for x. In spite of this desirable property, the Wigner function is not a true probability distribution because it may be negative in some places, which in fact is a signature of a quantum state.

Taking the time derivative of the Wigner function and using the Schrödinger equation,

$$i\hbar\frac{\partial\psi(x,t)}{\partial t} = \frac{\hbar^2}{2m}\frac{\partial^2\psi(x,t)}{\partial x^2} + V(x)\psi(x,t) \tag{1.4}$$

the quantum Liouville equation can be derived as [6],

$$\frac{\partial W}{\partial t} = -[\frac{p}{m}\partial_x - \partial_x V(x)\partial_p]W(x,p) + \sum_{\lambda=1}^{\infty}\frac{(\hbar/2i)^{2\lambda}}{(2\lambda+1)!}\partial_x^{2\lambda+1}V(x)\partial_p^{2\lambda+1}W(x,p). \tag{1.5}$$

For a quantum particle to resemble the behavior of a classical object, its Wigner function is required to be sharply peaked and stay localized in phase space, so that the centroid of the Wigner function (viz. the mean of x and p, $\langle x\rangle$ and $\langle p\rangle$) can be interpreted as the position and momentum of the quantum particle. From the quantum Liouville equation (1.5), equations of motion for the centroid are given by [2],

$$\langle\dot{x}\rangle = \frac{\langle p\rangle}{m} \tag{1.6}$$

and

$$\langle\dot{p}\rangle = \langle F(x,t)\rangle. \tag{1.7}$$

These are well-known as the Ehrenfest theorem [7]. We expand $\langle F(x,t)\rangle$ in a Taylor series,

$$\langle F(x,t)\rangle = F(\langle x\rangle) + \frac{\sigma_x^2}{2}\partial_x^2 F(\langle x\rangle) + ... \tag{1.8}$$

where σ_x is the standard deviation of x. For potentials containing terms up to quadratic order in x, such as a free particle, a particle under a constant force or a harmonic

oscillator, the last term in both Eq.(1.5) and Eq.(1.7) would be zero. Hence, Eq.(1.5) reduces to the classical Liouville equation and Eq.(1.7) becomes

$$\langle \dot{p} \rangle = F(\langle x \rangle, t). \tag{1.9}$$

In this case, the equations for the centroid $\langle x \rangle$ and $\langle p \rangle$ are the exactly same as the Newton's equations for a classical particle [Eqs.(1.1) and (1.2)] and the time evolution of Wigner function in phase space recovers that of the corresponding classical distribution.

In general, if the potential $V(x)$ has derivatives higher than the quadratic order, i.e. *a nonlinear system*, the last term in Eq.(1.5) will not be zero. Moreover, even if the Wigner function is sharply peaked at the beginning, it has a tendency to spread out over phase space, so that the reduction to Eq.(1.9) remains valid. The associated quantum dynamics of nonlinear systems then become qualitatively different from those of its classical counterparts [2, 8, 9]. The quantum dynamics of nonlinear systems are therefore of particularly interest in the study of the QCT.

In addition, chaos also illustrates the contradiction between classical and quantum mechanics [8]. A classical *nonlinear system* can be chaotic; i.e., it can be is extremely sensitive to initial conditions. Separation between different trajectories in phase space exhibit an exponential growth due to perturbations in initial conditions. On the contrary, owing to Heisenberg uncertainty principle, the evolution of a quantum system is not very sensitive to initial conditions and thus the quantum system is not chaotic in a classical sense. Again, this shows that the nonlinearity plays a central role in QCT.

As an example, we consider in some detail a nonlinear system that has been studied in depth, i.e. the Duffing oscillator. The model of a driven nonlinear Duffing oscillator is widely used in mesoscopic systems, such as Josephson junctions and nanomechanical systems [8–11]. It is described by the equation

$$\ddot{x} + \beta\dot{x} + \omega_0^2 x + \gamma x^3 = A\cos\omega_F t. \tag{1.10}$$

Here, ω_0 is the natural frequency, β is the damping coefficient ($\beta \ll \omega_0$), γ is the strength of nonlinearity ($\gamma > 0$), and ω_F is the driving frequency. The corresponding Hamiltonian is,

$$H(x,p,t) = \frac{1}{2}p^2 + \frac{1}{2}\omega_0^2 x^2 + \frac{1}{4}\gamma x^4 - xA\cos(\omega_F t). \tag{1.11}$$

This describes a double well potential with two stable states. For small driving amplitude A, the driven oscillations are nearly sinusoidal, $x(t) = a\cos(\omega_F t + \phi)$. We assume that the detuning $\delta\omega = \omega_F - \omega_0$ of the driving frequency ω_F from ω_0 is small and $\delta\omega > 0$. Under these conditions, the system displays bistability for certain amplitudes. At the bifurcation points $A_{B1,2}$, one of the stable states disappears. As one stable state switches to another, there is a great change in both the amplitude and phase of the driven oscillation. This bistability can be used for sensitive quantum measurement, such as measurement of the states of Josephson junction based qubits [12].

Katz *et al.* [9] calculated the classical and quantum evolution of a driven Duffing oscillator coupled to an environment. They found that at a very early stage of the evolution, the quantum Wigner function and the classical phase space distribution agree with each

other. In the regime where the typical quantum energy scale $\hbar\omega_0$ is comparable with that of thermal energy k_BT and the quality factor $Q \approx 10^3$, the Duffing oscillator is expected to become bistable and one should expect to observe the deviation from classical dynamics to quantum dynamics.

1.2 Quantum Computation

Quantum mechanics, being a century-old branch of physics, has struck an unprecedented interest in scientists and engineers from various fields in the last two decades, by its seemingly unlikely marriage to another revolution in the history of human technology, namely, the invention of integrated circuits and digital computers. The children of this marriage have been named as "quantum information processing" or "quantum computing" [13].

Originally postulated by Richard Feymann in 1982 [14], a quantum computer takes direct advantage of properties unique to quantum mechanics, such as superposition and entanglement to represent data and perform operations on data. While a classical digital computer stores data in classical binary digits (bits, i.e. 0 and 1), information is represented in a quantum computer as superpositions of quantum bits (qubits, viz. $|0\rangle$ and $|1\rangle$ quantum states). Incredible advances in computational power have subsequently been proposed by devising algorithms that are inherently quantum, such as Deutsch–Jozsa algorithm [15], Shor's algorithm [16], Grover's algorithm [17], just to name a few.

Although this dissertation is not directly concerned with building a quantum computer or implementing quantum algorithms, the engineering techniques developed and physics insights gained by the quantum computing field has been a great help for this dissertation, especially recent advances in superconducting circuits. Hopefully this dissertation will in turn shine a light on the development of quantum computer in the near future.

1.3 Superconducting Circuits

Superconducting circuits, the quantum version of integrated circuits [18], are solid-state circuits designed and fabricated using techniques borrowed from conventional integrated circuits. They are commonly used to engineer superconducting quits, which act like coherent artificial atoms. They usually consist of capacitors, inductors and dissipationless nonlinear Josephson junctions. They have several advantages over natural atoms.

First, as the name indicates, superconducting circuits become superconducting below certain critical temperatures. This means they have ultra-low dissipation for carrying and transmitting electrical signals.

Second, utilizing design concepts and techniques from conventional integrated circuits, such as electron-beam or optical lithography, superconducting circuit wires and junctions are reliably and most commonly made on silicon wafers. The micron and sub-micron size of the circuit elements makes possible simplifying the circuits to a transmission line model or even a lumped-element circuit [See Chapter 2 for details].

Third, in contrast to microscopic degrees of freedom, such as spins or atoms, superconducting circuits are easily coupled to conventional electrical circuits. Nonetheless, strong coupling poses another challenge: how does one isolate the circuit from the noisy environment so as to keep the circuit quantum coherent, while maintaining the control and readout channels to the circuit. Fortunately, the circuit quantum electrodynamics (QED) architecture answers the question.

1.4 Cavity Quantum Electrodynamics

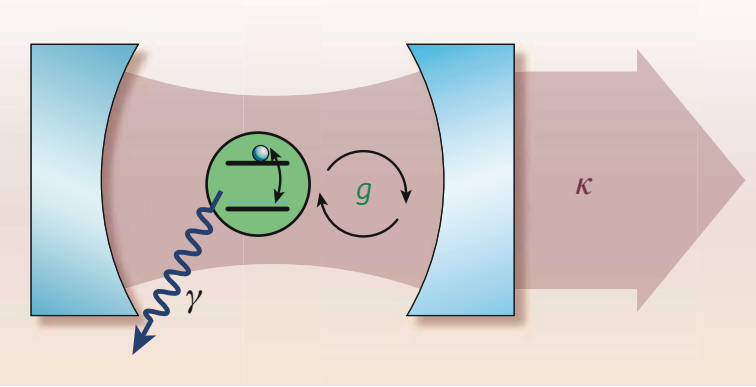

FIGURE 1.2: Schematic representation of a cavity QED system, consisting of a two-level atom interacting with a particular mode of the optical cavity. [19]

Before diving into circuit QED, it is necessary to mention its elder brother, namely, cavity quantum electrodynamics (cavity QED). Cavity QED is the study of the interaction between light and matter confined in a reflective cavity, where the quantum nature of light is significant. The simplest cavity QED system consists of a two-level 'atom' (such as a natural atom, spin or qubit) coupled via a dipole interaction, to a single cavity mode defined by two cavity mirrors, as in Fig. 1.2. The full quantum description of

such a system is given by the Jaynes-Cummings Hamiltonian:

$$H_{JC} = \hbar\omega_r(a^\dagger a + 1/2) + \hbar\omega_a\sigma_z/2 + \hbar g(a^\dagger\sigma^- + a\sigma^+). \tag{1.12}$$

The first term of the model is the cavity energy, which is represented by a harmonic oscillator with angular frequency ω_r. The second term describes the atom as a spin–1/2, with transition energy $\hbar\omega_a$. The last term represents the dipole interaction between light and atom, viz. the atom can either absorb (σ^+a) or emit ($\sigma^-a^\dagger$) a photon from or to the cavity at a rate of g.

In reality, there are always incoherent processes involved in the system, such as photons leaking out of the cavity at a rate of κ, or decay of the photon through other mechanisms at a rate of γ. In the strong coupling regime of cavity QED, the exchange rate between the atom and light is much greater than the combined rate of losses, i.e. $g \gg \kappa, \gamma$. In addition, if the atom is in resonance with the cavity, the system would oscillate between a cavity photon and an excitation in the atom many times, before the photon ever escapes or the atom decays. This is known as vacuum Rabi oscillation, a phenomenon that reveals the quantum nature of the light.

1.5 Circuit Quantum Electrodynamics

By switching the physical incarnation of cavity QED from optical cavity to superconducting microwave circuit and from natural atoms to artificial atoms, a new architecture

for studying quantum information and quantum optics, circuit quantum electrodynamics (circuit QED) has been invented and developed over the last decade [20–22].

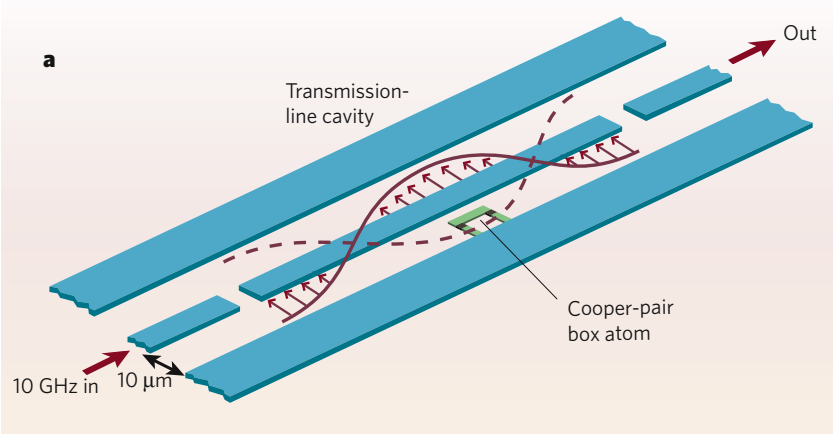

FIGURE 1.3: Schematic representation of a circuit QED system. A Cooper pair box atom is located at the center of the transmission line. [19]

In circuit QED, a superconducting device, such as a quantum two-level system (qubit) is placed inside an on-chip high-Q microwave cavity, as shown in Fig. 1.3. The superconducting microwave cavity can be implemented by a one-dimensional transmission line resonator, in which the photons are confined and can only travel along the center conducting wire, like signals in a TV coaxial cable. Gaps in the wire are in this case "the mirrors" that define the boundary of the cavity.

The key feature of this implementation is the very tight lateral confinement of both the photons and the artificial atom in the on-chip cavity, making ultra-strong coupling between them much easier to reach than its cavity QED counterpart. In addition, the losses in the superconducting wire are so low that a photon can bounce between the mirrors for as many as a million times before it escapes or is absorbed. The simple transmission line geometry also makes the coupling between the cavity and the outside

world easy to adjust and control, thus becoming a promising candidate for solving the problem posed at the end of Section 1.3. The details of the circuit QED are discussed in Chapter 2.

1.6 Dissertation Overview

Although this dissertation has an ambitious title, I have to warn the reader that an exhaustive investigation of the cavity-embedded-cooper pair transistor (cCPT), is by no means to close to finished. I expect that this dissertation to be only a starting point of a series of cCPT experiments carried out in the Rimberg group at Dartmouth and beyond. This dissertation could serve as a reference for future investigations. An outline of this dissertation is as follows: **Chapter 2** introduces the transmission line model of the circuit QED architecture and a reliable physical realization of this model, i.e. the coplanar waveguide resonator. **Chapter 3** presents a technique essential for the development of the cCPT, namely, applying a dc bias to the center conductor of a high-Q superconducting microwave cavity without significantly disturbing selected cavity modes. **Chapter 4** reviews another building block of the cCPT, i.e. the Josepshon junction and its well-known effects. From such junctions, the Cooper pair transistor (CPT) is made and ultimately becomes the cCPT when embedded into the dc-biased circuit QED architecture. **Chapter 5** discusses the design and fabrication process of the cCPT devices, including techniques that are indispensable to nanotechnology and low-temperature experiments. **Chapter 6** describes a variety of cryogenic and measurement setups related to the experiments as well as quantum state reconstruction used to

characterize the cCPT emission fields. **Chapter 7** is the core of this dissertation, where various aspects of measurement and reconstruction results of the cCPT experiments and their implications on quantum dynamics in a strongly nonlinear system are discussed. A brief conclusion of this dissertation is offered at the end of of Chapter 7 .

Chapter 2

Circuit Quantum Electrodynamics

The circuit QED architecture was originally proposed by the Schoelkopf group at Yale University in 2004 [23]. Soon after that, they experimentally demonstrated that a superconducting qubit can be strongly and coherently coupled to a single microwave photon [20]. This possibility of investigating superconducting qubits has lead to a wide range of novel quantum information and quantum optics experiments in the circuit QED architecture [24–29]. More recently, this versatile architecture has also been successfully employed for study of quantum dots [30, 31], electron-spin ensembles [32] and nano mechanical resonators [33, 34].

Given the versatility of the circuit QED architecture and the explosion of new results at

the intersection of condensed matter and atomic physics it has engendered, a comprehensive review of the architecture is beyond the scope of this dissertation. Nevertheless, this chapter introduces the basic model and the building blocks of the architecture. It can serve as a baseline for understanding and implementing the architecture.

2.1 Transmission Line Resonator

The microwave regime refers to frequencies between 300 MHz and 300 GHz, or corresponding wavelengths between $\lambda = c/f = 1$ m and $\lambda = 1$ mm. Because of the relatively short wavelengths, it is difficult to realize ideal lumped element circuits in this frequency regime. Instead, a transmission line resonator can be implemented as a microwave cavity. Compared with lumped element circuits, a transmission line resonator is a distributed circuit with voltages and currents varying in magnitude and phase over its length. It avoids uncontrolled stray capacitance and inductances, which allows for better microwave performance. In addition, the one dimensional transmission line resonator has some similarities to a lumped element circuit and thus can be modeled as an LCR circuit. The discussion in this section follows Chapter 2 and 3 in Pozar[35].

2.1.1 Parallel LCR Resonant Circuit

Starting with a canonical parallel LCR circuit shown in Fig. 2.1(a), the input impedance for the circuit is given by

$$Z_{\text{in}} = (\frac{1}{R} + \frac{1}{i\omega L} + i\omega C)^{-1}. \tag{2.1}$$

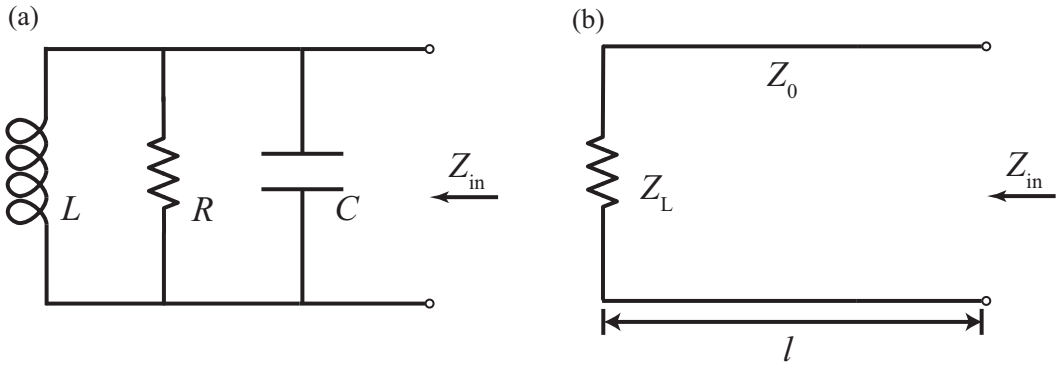

FIGURE 2.1: (a) A parallel LCR circuit. (b) A transmission line terminated in Z_L.

At the resonant frequency, $\omega_0 = 1/\sqrt{LC}$, the input impedance is purely real: $Z_{\text{in}} = R$. Near resonance ($\Delta\omega/\omega \ll 1$), our main regime of interest, Eq.(2.1) can be expanded in $\Delta\omega = \omega - \omega_0$ to the first order,

$$Z_{\text{in}} \approx \frac{R}{1 + 2iQ\Delta\omega/\omega} \tag{2.2}$$

where the quality factor of the resonant circuit is $Q = \omega_0 RC$. From Eq.(2.2), it is clear that the input impedance for the parallel circuit is sharply peaked at resonance, and its maximum value is given by R.

2.1.2 Transmission Line Resonator as LCR Circuit

Now we focus on the transmission line as in Fig. 2.1(b). The effective input impedance of a lossy transmission line with characteristic impedance Z_0, terminated in a load Z_L at a distance l is

$$Z_{\text{in}} = Z_0 \frac{Z_L + Z_0 \tanh \gamma l}{Z_0 + Z_L \tanh \gamma l} \tag{2.3}$$

where $\gamma = \alpha + i\beta$, α is the attenuation constant, and $\beta = 2\pi/\lambda$ is the propagation constant of the line.

We are mostly interested in transmission lines terminated by nearly open or ideally open circuits ($Z_L = \infty$). In this case,

$$Z_{\text{in}} = Z_0 \coth \gamma l = Z_0 \frac{1 + i \tan \beta l \tanh \alpha l}{\tanh \alpha l + i \tan \beta l}. \tag{2.4}$$

Considering a transmission line with a full wavelength at the resonant frequency ω_0, we have the length $l = \lambda = 2\pi v/\omega_0$, where $v = 1/\sqrt{L_l C_l}$ is the phase velocity and L_l, C_l are the inductance and capacitance per unit length of the transmission line respectively. Again let $\omega = \omega_0 + \Delta\omega$, $(\Delta\omega/\omega \ll 1)$. We have

$$\beta l = \frac{\omega l}{v} = \frac{\omega_0 l + \Delta\omega l}{v} = 2\pi + \frac{2\pi\Delta\omega}{\omega_0} \tag{2.5}$$

and

$$\tan \beta l = \tan 2\pi \frac{\Delta\omega}{\omega_0} \approx 2\pi \frac{\Delta\omega}{\omega_0}. \tag{2.6}$$

In practice, most transmission lines, superconducting lines in particular, have a very low loss, hence we can assume that $\alpha l \ll 1$, and thus $\tanh \alpha l \approx \alpha l$. Applying these results

to Eq.(2.4) gives,

$$\begin{aligned} Z_{\text{in}} &\approx \frac{Z_0}{\alpha l + i\frac{2\pi\Delta\omega}{\omega_0}} \\ &= \frac{Z_0/\alpha l}{1 + 2i(\frac{\pi}{\omega_0 Z_0})(\frac{Z_0}{\alpha l})\Delta\omega}. \end{aligned} \tag{2.7}$$

Comparing with the input impedance of a parallel resonant circuit given by Eq.(2.2), it is easy to see that an open-circuited full-wave transmission line resonator looks very much like a parallel LCR resonant circuit for which,

$$C = \frac{\pi}{\omega_0 Z_0}, \quad R = \frac{Z_0}{\alpha l}. \tag{2.8}$$

We also find that

$$L = \frac{1}{\omega_0^2 C}, \quad Q = \omega_0 RC = \frac{\pi}{\alpha l}. \tag{2.9}$$

Using the relation $\omega_0 = 2\pi v/l = \frac{2\pi}{l\sqrt{L_l C_l}}$, we can then express L and C in terms of L_l and C_l as

$$C = \frac{C_l l}{2}, \quad L = \frac{L_l l}{2\pi^2}. \tag{2.10}$$

The LCR model of the transmission line resonator presents an intuitive means of understanding the resonator properties. Its input impedance $|Z_{in}|$ should be sharply peaked near resonance, with a maximum value given by $Z_0/\alpha l = Z_0 Q/\pi$ and a bandwidth given by ω_0/Q. The LCR model also simplifies analyzing the effect of coupling the resonator to input and output lines as discussed in the next subsection.

2.1.3 Capacitively Coupled Transmission Line Resonator

A perfectly isolated transmission line resonator is only a mathematical model and is of no practical use. It has to be somehow coupled to the outside world and yet without losing its high loaded quality factor Q_L, the key property one wants to take advantage of for implementing such a resonator. In practice, it is most often coupled to input and output lines via small capacitors, whose values can be accurately estimated and reliably engineered. The input and output capacitors acts like two face-to-face mirrors, reflecting the photons inside the cavity back and forth for a large number of times, before any of them can escape through either of the mirrors.

For simplicity, the input and output coupling capacitors are assumed to be identical and small, i.e. $C_{int} = C_{out} = C_\kappa$, and we stick to our focus around the full wave resonance ω_0. Once we understand this simplest scenario, the case for asymmetric couplings and higher harmonics will be straightforward.

To analyze the effect of the series connections of capacitors C_κ and typical loaded impedance $Z_L = R_L = 50\Omega$, we can transform the circuit as in Fig. 2.2(a) into a Norton equivalent circuit [36, 37] with parallel connections of resistors R^* and capacitors C^* as illustrated in Fig. 2.2(b) with

$$R^* = \frac{1 + R_L^2 C_\kappa^2 \omega_0^2}{R_L C_\kappa^2 \omega_0^2} \tag{2.11}$$

$$C^* = \frac{C_\kappa}{1 + R_L^2 C_\kappa^2 \omega_0^2}. \tag{2.12}$$

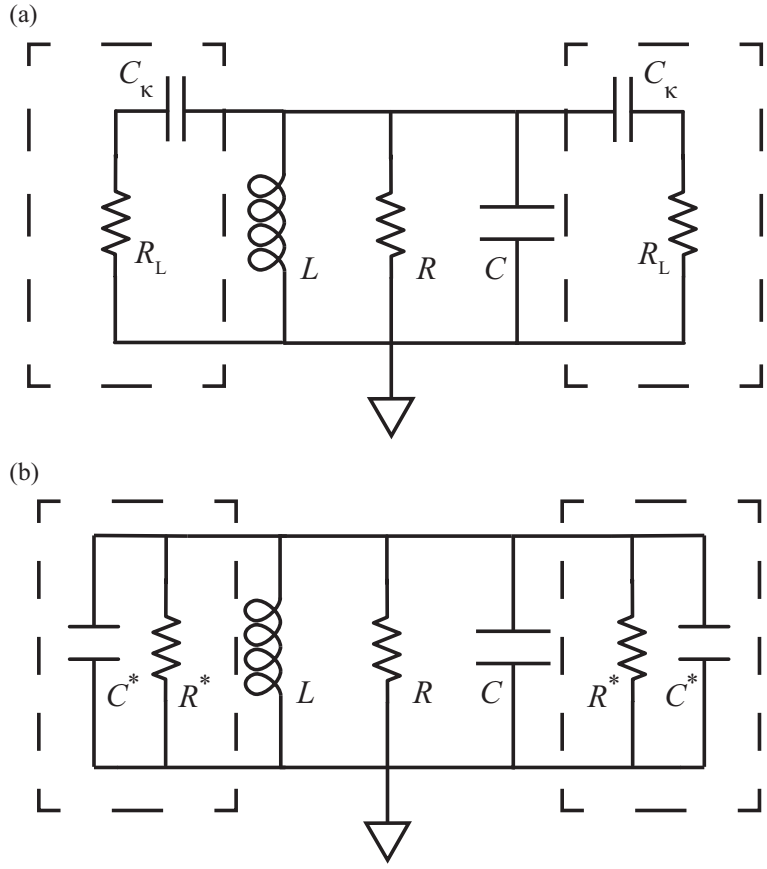

FIGURE 2.2: (a) Effective parallel LCR model of transmission line resonator coupled with symmetric input/output capacitors. (b) Norton equivalent circuit of (a).

The transformed circuit is still essentially a parallel LCR circuit and therefore the loaded quality factor Q_L is given by

$$Q_L = \omega_0^* \frac{C + 2C^*}{1/R + 2/R^*} \tag{2.13}$$

$$\approx \omega_0 \frac{C}{1/R + 2/R^*} \tag{2.14}$$

where

$$\omega_0^* = \frac{1}{\sqrt{L(C + 2C^*)}} \tag{2.15}$$

which indicates that the modified resonant frequency ω_0^* is slightly pulled down by each coupling capacitor.

Eq. (2.14) is derived using the assumption that $R_L C_\kappa \omega_0 \ll 1$ and $C_\kappa \ll C$, which indicates $R^* \approx 1/R_L C_\kappa^2 \omega_0^2$ and $C^* \approx C\kappa \ll C$. Hence to the first order, $\omega_0^* \approx \omega_0$ and $C \approx C + 2C^*$. For small capacitors, the frequency shift induced by coupling can often be neglected.

To better understand the effects of external couplings and internal loss on the loaded quality factor Q_L, Eq. (2.14) can be transformed to

$$\frac{1}{Q_L} = \frac{1}{Q_{\text{int}}} + \frac{1}{Q_{\text{ext}}} \tag{2.16}$$

where the external quality factor is

$$Q_{\text{ext}} = \omega_0 C R^* \tag{2.17}$$

and the internal quality factor is the same as the quality factor of an open-circuited transmission line resonator as in Eq. (2.9),

$$Q_{\text{int}} = \omega_0 C R_{\text{int}} = \frac{\pi}{\alpha l}. \tag{2.18}$$

This confirms the idea that the loaded Q_L depends on both the internal quality factor Q_{int}, and its capacitive coupling to the input and output lines.

There are two possible regimes for capacitive coupling of the resonator. When C_κ is very small, the effect of Q_{ext} on Q_L is negligible, $Q_L \approx Q_{\text{int}}$, and the resonator is in the undercoupled regime. These resonators with large quality factors can be used to store photons in the cavity on a long time scale. On the other hand, the resonator can be overcoupled when C_κ is relatively large and then Q_L is governed by Q_{ext}, $Q_L \approx Q_{\text{ext}} \approx C/2\omega_0 R_L C_\kappa^2$, whose value is reliably controlled by the coupling capacitors. It is then convienient to engineer the Q_L for performing fast measurement of the cavity state [20].

Another measurable transmission quantity that demonstrates the competition between the internal and external Qs is, the insertion loss L_0, i.e. the deviation of peak transmission from unity. It is defined as [37]

$$L_0 = -20 \log(\frac{g}{g+1}) \text{ dB} \tag{2.19}$$

where $g = Q_{\text{int}}/Q_{\text{ext}}$ is the coupling coefficient of the resonator. In the undercoupled regime where C_κ is small, $g > 1$ and L_0 is significantly greater than zero. This makes sense in that for small coupling capacitors, it is difficult for the photons inside the cavity to escape via the capacitors and some photons are thus lost to other internal dissipation, making the number of the transmitted photons significantly less than the number of incoming ones. On the other hand, in the overcoupled regime where C_κ is large, $g \ll 1$, $L_0 \approx 0$ and nearly all photons entering the cavity are able to escape through the capacitors. One must be aware of the existence of the insertion loss, when calibrating the gains and losses of the whole microwave transmission setup.

2.2 Coplanar Waveguide (CPW) Resonator

The coplanar waveguide (CPW) geometry is chosen to realize the transmission line resonator for several reasons. First, CPW has its ground on the same plane with the center conductor, separated by gaps as in Fig. 2.3. This simple single-sided geometry is ideal for surface mounted components, such as a Cooper pair box or transistor. Second, we can easily control the lateral scales of the center conductors and gaps from micrometers to millimeters while keeping the impedance constant. The small lateral dimensions indicate large electromagnetic fields are well constrained within the gaps thus enabling ultra-strong coupling between the cavity and the device placed in the gaps. Meanwhile, millimeter dimensions also facilitate integration with printed circuit boards. Last but not the least, CPW resonators with loaded Qs in a wide range from $\sim 10^2$ to $\sim 10^6$ have been readily realized [36, 37].

2.2.1 Geometry

As illustrated in Fig. 2.3, the length l of CPW is defined by capacitors at both ends. The the resonant frequency f_0 of a full-wave CPW is given by

$$f_0 = \frac{c}{\lambda\sqrt{\varepsilon_{\text{eff}}}} = \frac{c}{l\sqrt{\varepsilon_{\text{eff}}}} \tag{2.20}$$

with the phase velocity $v = c/\sqrt{\varepsilon_{\text{eff}}}$.

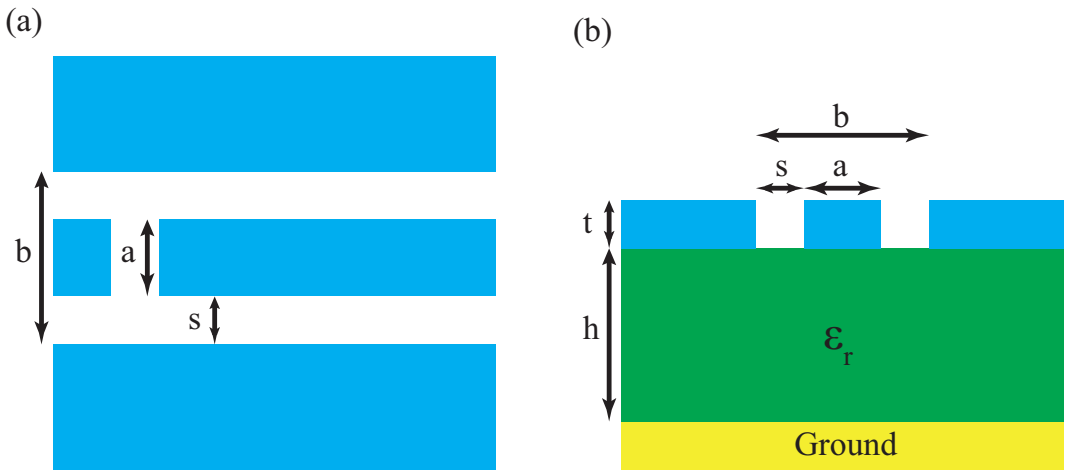

FIGURE 2.3: (a) Top view of a CPW resonator with a gap capacitor. (b) Cross section of a CPW resonator with a backing ground.

Here the the relative effective dielectric constant ε_{eff} and the impedance of the CPW are controlled by its dimensions [38],

$$\varepsilon_{\text{eff}} = \frac{1 + \varepsilon_r \widetilde{K}}{1 + \widetilde{K}} \tag{2.21}$$

$$Z_0 = \frac{60\pi}{\sqrt{\varepsilon_{\text{eff}}}} \left(\frac{K(k)}{K(k')} + \frac{K(k_1)}{K(k_1')} \right)^{-1} \tag{2.22}$$

where K denotes the complete elliptic integral of the first kind with

$$\widetilde{K} = \frac{K(k')K(k_1)}{K(k)K(k_1')} \tag{2.23}$$

$$k = \frac{a}{b} \tag{2.24}$$

$$k' = \sqrt{1 - k^2} \tag{2.25}$$

$$k_1 = \frac{\tanh(\frac{\pi a}{4h})}{\tanh(\frac{\pi b}{4h})} \tag{2.26}$$

$$k_1' = \sqrt{1 - k_1^2} \tag{2.27}$$

and ε_r is the relative dielectric constant of the substrate with height h, center conductor width a, gap width s, and separation of the ground planes $b = 2s + a$. The ground plane should extend a distance greater than $5b$ on each side of the gap in order for the above equations to be a proper model of the distributed circuit. The inductance and capacitance per unit length can also be calculated [39] from

$$L_l = \frac{\mu_0}{4} \frac{K(k_0')}{K(k_0)} \tag{2.28}$$

$$C_l = 4\varepsilon_0 \varepsilon_{\text{eff}} \frac{K(k_0)}{K(k_0')} \tag{2.29}$$

where the permeability constant μ_0, also known as the permeability of free space, is $\mu_0 = 4\pi \cdot 10^{-7}\text{H/m}$.

2.2.2 Kinetic Inductance in Superconducting CPW

Another factor that could play a important role in calculating the resonant frequency of superconducting resonators is kinetic inductance. In a normal metal and at low frequencies, the kinetic energy of electrons dissipates quickly into the metal through collisions, so it does not need to be taken into consideration when calculating inductance. However, in superconductors, the kinetic energy of the moving Cooper pairs in an ac field, is equivalent to a series inductance, and is known as the kinetic inductance.

Thus the total inductance per unit length of a superconductor consists of the magnetic (geometric) inductance and kinetic inductances, $L_l = L_m + L_K$. L_K is proportional to λ_L^2/A [39], where $A = at$ is the cross sectional area of the center conductor as in Fig. 2.3 and λ_L is the London penetration depth of the thin film, which characterizes the distance a magnetic field penetrates into the superconducting film[40]. The kinetic inductance becomes a dominant part in total inductance when the film thickness is less than its London penetration depth. Fortunately, in our case, we use aluminum or niobium films, which have a relatively short London penetration depth, i.e. 16 nm and 39 nm respectively [41]. So as long as we deposit a film thicker than 100nm and have the center conductor width $a = 10\,\mu m$, the fraction of the total inductance attributing to the kinetic inductance L_K/L_l is estimated and experimentally verified to be $\sim 1\% - 10\%$ [21, 36, 42]. Since the resonant frequency $f_0 \propto 1/\sqrt{L}$, the resulting downward shift in the resonance is less than 5%.

2.2.3 Losses in CPW

Conventional coplanar waveguide resonators have three types of intrinsic losses: dielectric, resistive, and radiative. Among these, the dielectric loss is generally believed to be the limiting factor [37, 42] for the internal Q of superconducting resonators. Nevertheless, if one uses a low-loss dielectric substrate, such high-resistivity silicon and sapphire, a Q as high as $\sim 10^6$ can still be readily achieved. Also, most of the experiments in this dissertation are conducted in the overcoupled regime of the resonators so that the dielectric is not a major concern.

Another possible loss mechanism in superconducting thin films is dissipation due to the trapping of magnetic vortices. In sufficiently large magnetic magnetic fields, trapped flux exists in the form of vortices for both Type I (e.g. aluminum) and Type II (e.g. niobium) superconducting thin films [40] . This contributes additional loss to the resonator and can result in potentially substantial reduction in Q.

The loss associated with vortices depends strongly on sample preparation and geometry. For a simple superconducting strip with width w, there exist a threshold field B_m [43, 44], below which all the magnetic flux is expelled from the strip and the Meissner effect is complete. This threshold field has also been experimentally demonstrated to scale as $B_m \sim \Phi_0/w^2$ [43], where $\Phi_0 = h/2e$ is the flux quantum. For a 12 μm wide Al strip and a 10μm wide Nb strip, the threshold fields have been measured to be about 20 μT [44] and 62 μT [43], respectively.

In all the experiments performed in this dissertation, no external magnetic field is ever applied. However, we still need to take into account Earth's magnetic field, whose magnitude at the Earth's surface ranges from 25 to 65 μT. Located in Hanover, New Hampshire, our lab has an Earth's field about 55 μT, due to its relatively high latitude. So even if we just consider the center conductor of the CPW, which is usually 10 μm wide in our designs, the Earth's field is larger than the threshold field of Al and very close to that of Nb. Since the ground planes of the CPW is at the very least hundreds of microns wide, flux will be trapped into the films for either Al or Nb. Therefore, magnetic shields have to be installed in order to reduce the ambient field of the samples and thus avoid substantial reduction in Q. The details of magnetic shielding is discussed in Chapter 5.

Chapter 3

Introduction of a dc Bias into a High Q Microwave Cavity

The existing circuit QED architecture has provided the quantum information community with great flexibility and control in integrating superconducting quits and other interesting systems as discussed in previous chapter. Although it is quite versatile as it is, the ability to apply a dc bias to its center conductor would make it more so. For instance, a nano mechanical resonator strongly coupled to a quit can also be embedded within such a cavity to allow the study of decoherence of macroscopic objects [45].

In this chapter[1], we demonstrate a potentially very useful technique that builds on the circuit QED architecture, namely, applying a dc voltage or current bias to the center

[1]This chapter is adapted from [46]

conductor of coplanar waveguide cavity without significantly disturbing a particular cavity mode or degrading the cavity quality factor Q at high frequencies.

3.1 Design

The limitation of the standard architecture is caused by the need to define the cavity through coupling capacitances at either end [see Subsection 2.1.3]. Direct electrical contact there would destroy the cavity Q. Wire bonding to the center conductor is also made prohibitively difficult by its narrow width (typically a few microns) and in any case would seem likely to have similarly deleterious consequences for the cavity Q.

However, low-impedance dc contact to the interior of a circuit QED cavity is in fact possible. The dc biasing scheme is shown schematically in Fig. 3.1. We choose the main transmission line length l to be a full wavelength ($l = \lambda$) at the resonant frequency $f = f_0$. To allow application of a dc bias, two sections of $\lambda/2$-long transmission lines are added to the main full-wave resonator at points a distance $\lambda/4$ from either end (marked with the red dots), forming two "T" junctions. Each of the $\lambda/2$ shunt transmission lines is connected via an inductor L to a dc voltage or current source.

To understand the idea behind this arrangement, we first assume the main full-wave transmission line is lossless and terminated in an open circuit. The current at the end of the line is then zero and the voltage is a maximum, making this a high impedance point. The $\lambda/4$ point is then a voltage node (current antinode) and a low impedance point. From Eq.(2.4), the input impedance of a lossless transmission line terminated in an open

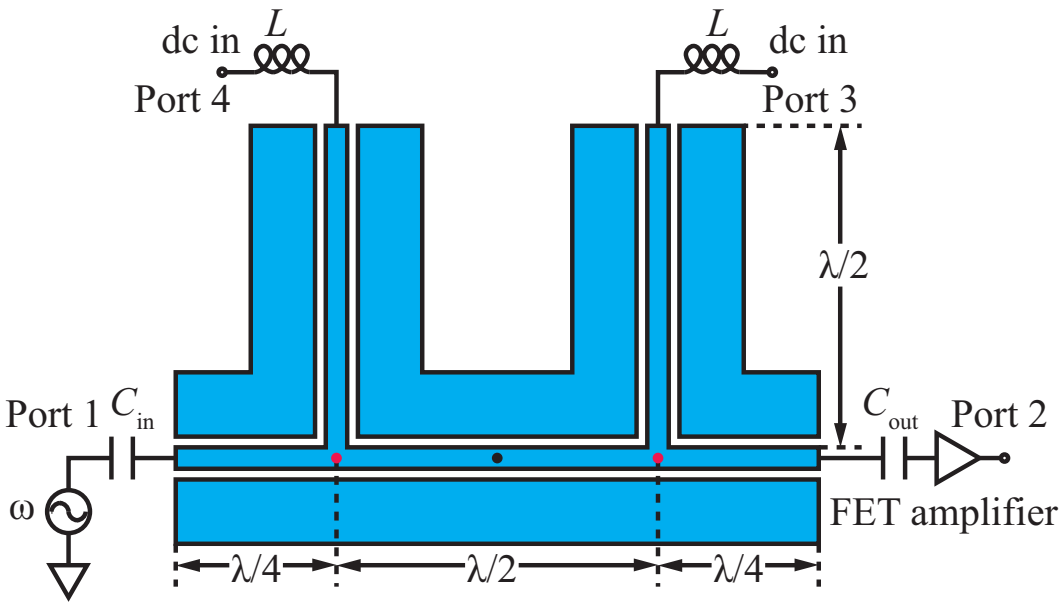

FIGURE 3.1: Schematic diagram for introduction of a dc bias into a high-Q microwave cavity of length λ. The red dots are the low impedance points and the black dot is a high impedance point. A Cooper pair box, transistor, or other structures can be located at the high impedance point.

circuit is given by $Z_{\text{in}} = Z_0 \coth i\beta l = -iZ_0 \cot \beta l$. If the length of the line is either $\lambda/4$ or $3\lambda/4$, then $Z_{\text{in}} = 0$. Sitting at one of the low impedance points, and looking towards either end of the transmission line, one sees a short. We want this condition to remain unchanged by the addition of the dc feed lines; so we want the impedance they present at the low-impedance point to be as large as possible.

One way to achieve this is to use $\lambda/2$ length of transmission line terminated in an inductor. The reason for using a half-wave transmission line is, from Eq.(2.3), the input impedance of a lossless transmission line of length l terminated in a load Z_L is given by

$$Z_{\text{in}} = Z_0 \frac{Z_L + iZ_0 \tanh \beta l}{Z_0 + iZ_L \tanh \beta l} \tag{3.1}$$

so that if $l = \lambda/2$, we have $Z_{in} = Z_L$: a $\lambda/2$ length of transmission line has an input impedance equal to that of its terminating impedance. The inductively terminated $\lambda/2$ dc bias lines therefore, present a high impedance $i\omega_0 L$, where $\omega_0 = 2\pi f_0$, to the main transmission line at the resonant frequency f_0. A microwave photon approaching the $\lambda/4$ points from the center of the cavity will therefore, still see a short (the $\lambda/4$ and $3\lambda/4$ lines to the ends of the cavity) in parallel with a high impedance $i\omega_0 L$ (the $\lambda/2$ bias line). To a first order approximation, the bias lines will have no effect on the full-wave cavity resonance.

In reality, the transmission line is not completely lossless, and the main line is terminated with small capacitors (on the order of a few fF) leading to 50 Ω rather than an open circuit. The impedance looking from a low impedance point towards either end of the line is still small but not identically zero. Reasonable values of inductance L must ensure the dc feed lines present a sufficiently large impedance to the main line, for the approximate picture described above to be valid.

While a shorter feed line (much less than $\lambda/2$, e.g. $\lambda/10$) can also work, the terminating impedance is transformed in a less understandable way and maybe harder to implement. In contrast, using a $\lambda/2$ feed line, the T junctions in our design are easy to understand; they are essentially the conventional bias tees applied to a distributed element circuit.

3.2 Device and Measurement Setup

Fig. 3.2 shows a Nb CPW resonator with dc feed lines. The CPW center conductor width is 10 μm and its separation from the ground planes is 5.5 μm, giving a wave impedance of approximately 50 Ω. It is fabricated from a 100 nm thick Nb film on a 10.5$\times$ 5.5 mm^2 high resistivity silicon substrate using sputtering, photolithography and dry etching, with an overall length l = 24 mm, giving $f_0 \approx$ 4.8 GHz. The resonator is coupled via identical capacitors $C_{\text{in}} = C_{\text{out}} = C_\kappa$ at each end to input and output microwave lines. Two coupling capacitors with different geometries are used to test the cavity design, namely, 4-finger ($C_\kappa \approx$ 4.5 fF) and 8-finger ($C_\kappa \approx$ 11.1 fF) capacitors. A 3-turn spiral inductor (linewidth of 5 μm, spacing of 10 μm, $L \approx$ 6 nH) is used to terminate the $\lambda/2$ shunt transmission lines.

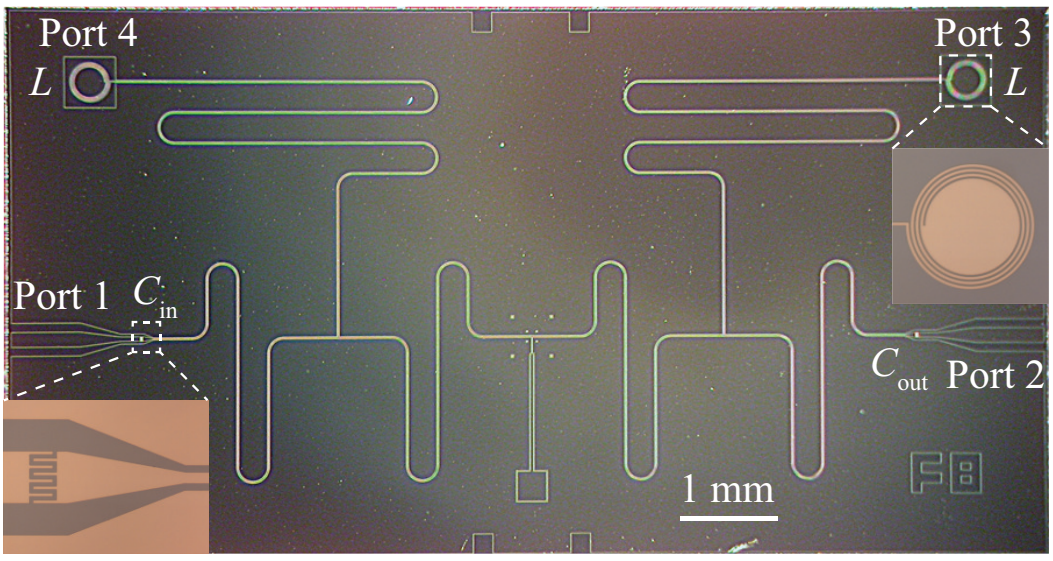

FIGURE 3.2: Optical micrograph of a 4.8 GHz superconducting niobium CPW resonator with dc feed lines. The insets show an 8-finger coupling capacitor and a 3-turn spiral inductor.

Using a signal generator and a spectrum analyzer, transmission measurements of resonators A and B (with 4- and 8-finger coupling capacitors, respectively) were performed at 4.2 K in a Helium dunker with an Amumetal 4K magnetic shield. A room temperature field-effect transistor (FET) amplifier (gain ∼45 dB at around 5 GHz) was used to amplify the signal prior to measurement by the spectrum analyzer. Losses in the cables (roughly 13 dB in each) leading to and from the sample were carefully measured and accounted for in the transmission measurements, and additional cold attenuation was not used. For all measurements unused ports were terminated by a 50 Ω impedance.

3.3 Characterization of Cavity Transmission

To estimate the intrinsic Q of Nb films at 4.2 K, we also fabricate a bare resonator C with symmetric 10 μm gap input/output capacitors and without the presence of the dc feed lines. Its transmission spectrum S_{21} is shown in Fig. 3.3, in which we can clearly see a sharp resonant peak at f_0 =4.864 GHz. The loaded quality factor $Q_L = f_0/\delta f$ is obtained by curve fitting a Lorentzian line shape:

$$S = A\frac{\delta f}{(f - f_0)^2 + \delta f^2/4} + A_0 \tag{3.2}$$

where δf is the full width half maximum of the resonance.

The loaded Q_L of resonator C is thus determined to be $Q_L = 6075$ by fitting a more finely sampled transmission spectrum around f_0. Since the 10 μm gap capacitor has a relatively small capacitance $C_\kappa \approx 0.42$ fF, and from Eq. (2.12), we get the coupling

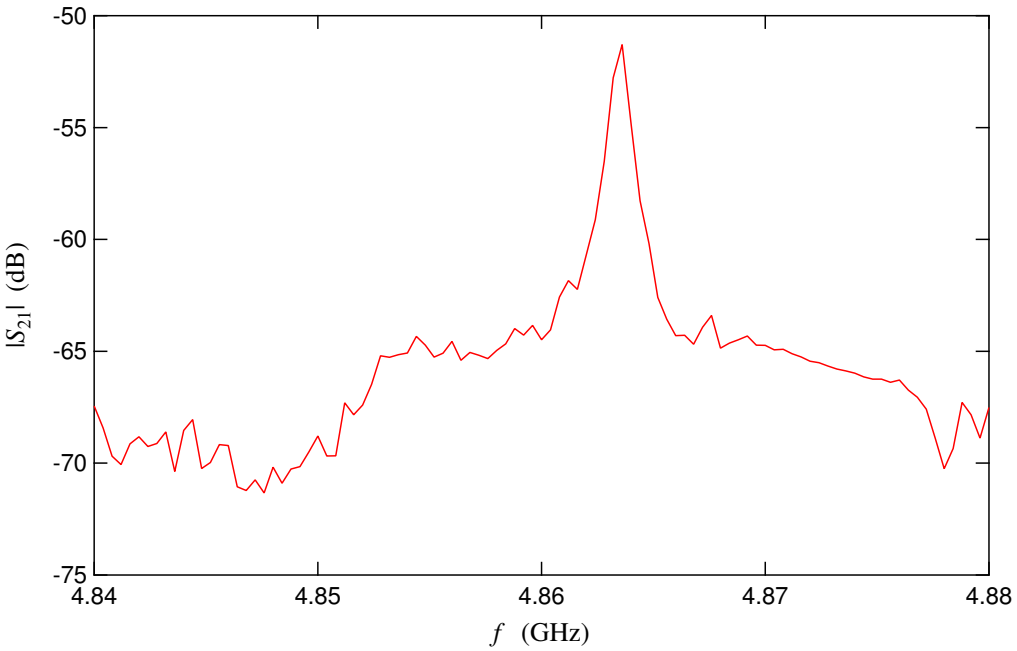

FIGURE 3.3: Measured transmission spectrum S_{21} of the bare resonator C without the dc feed lines.

$Q_{ext} \approx 3.7 \times 10^6$ at the resonant frequency and the resonator is well in the undercoupled regime. A intrinsic $Q \approx 6100$ is therefore estimated from Eq. (2.16). It is likely limited by losses in the Nb films at relatively high temperature (4.2K) of the measurements.

We now proceed to characterize the microwave performance of the system with bias lines. We measure transmitted power from the input port (Port 1) through the output port (Port 2) via coupling capacitors as well as power through spiral inductors (Port 3 and 4). Fig. 3.4(a) shows measured S-matrix parameters S_{21}, S_{31} and S_{41} of resonator A from 2 GHz to 6 GHz. Due to the presence of dc feed lines, the fundamental $\lambda/2$ resonance around 2.4 GHz is strongly damped and is not visible in S_{21}. This is to be expected since for the fundamental resonance, the bias lines are not located at a low

impedance point. In contrast, the first harmonic at 4.8 GHz corresponding to a full-wave excitation still exists as predicted by the simple impedance-based argument above. Futhermore, additional broad resonance are visible at around 3.6 GHz in S_{21}, S_{31} and S_{41}, as well as more weakly in S_{41} at about 3.2 GHz.

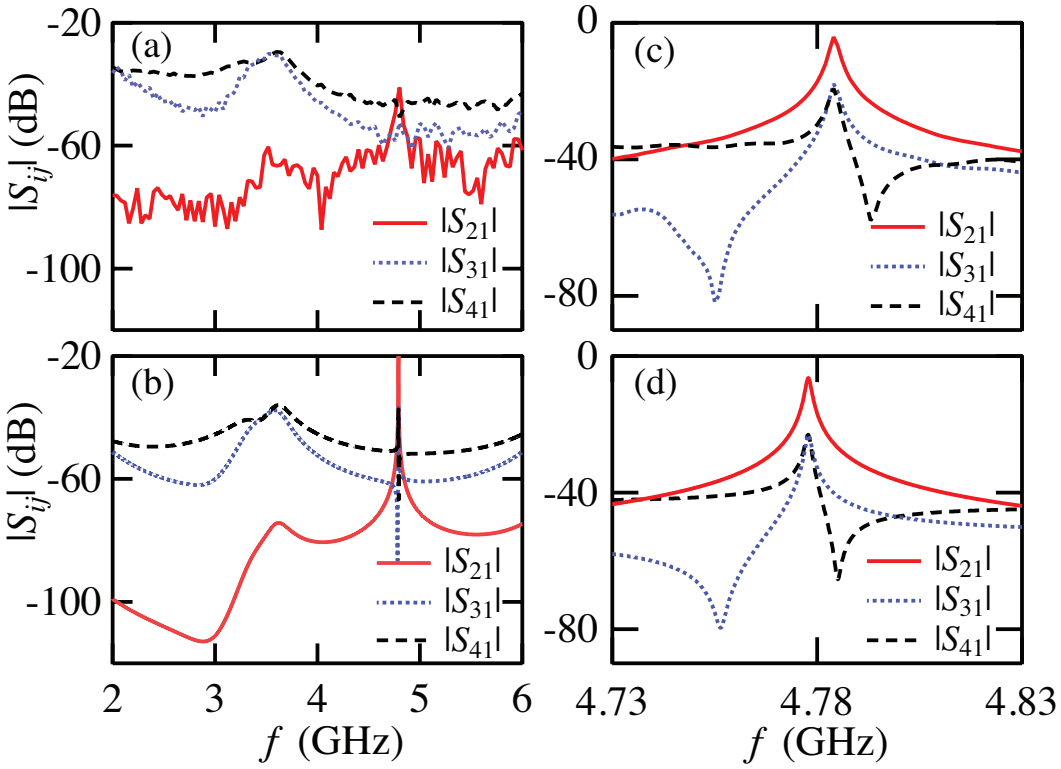

FIGURE 3.4: (a) Measured and (b) simulated transmission spectra S_{21} (solid), S_{31} (dotted) and S_{41} (dashed) of resonator A from 2 GHz to 6 GHz. (c) Measured and (d) simulated transmission spectra S_{21} (solid), S_{31} (dotted) and S_{41} (dashed) of resonator B in the immediate vicinity of the full-wave resonance.

3.4 Effect of the Application of a dc Bias

Before discussing additional resonances, we first examine the effect of a dc bias on the main line full-wave resonance. We determine the quality factors of the resonances by

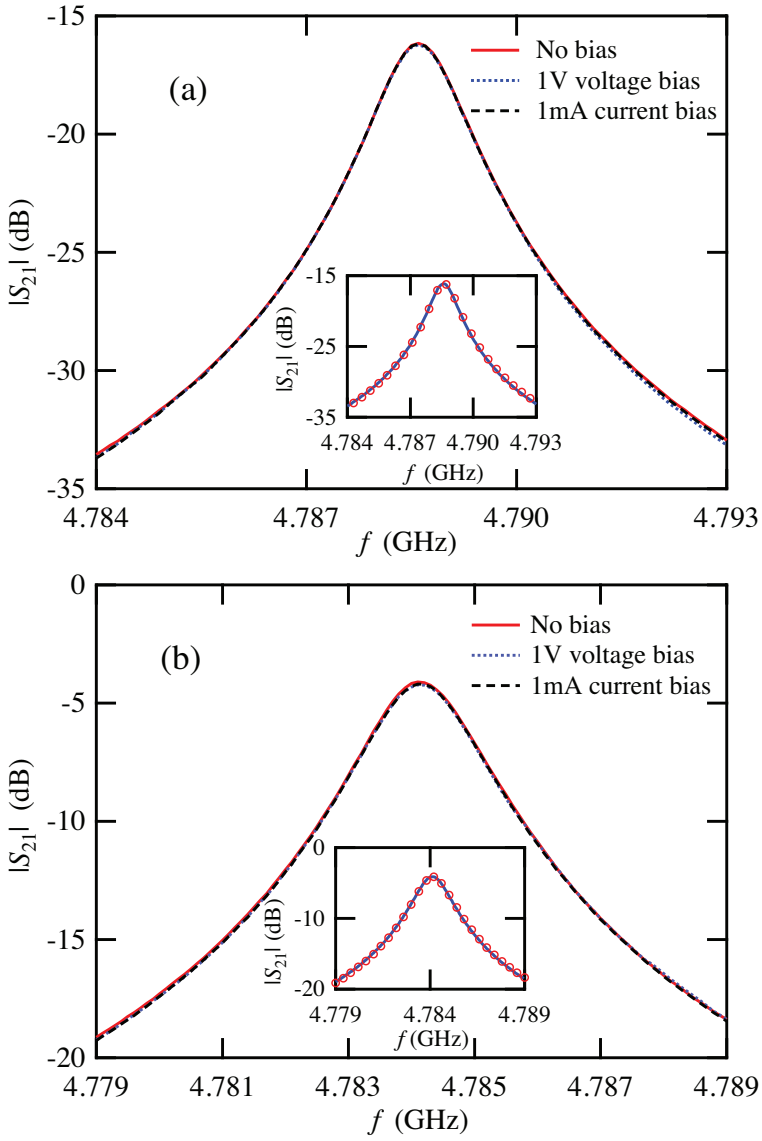

FIGURE 3.5: Measured transmission spectra S_{21} of (a) resonator A and (b) resonator B under different bias conditions. Insets: Lorentzian curve fits (blue curve) to the data points (red circles) when no dc bias is applied. To show the curve fits clearly, the density of data points displayed in the insets has been reduced by a factor of 4.

fitting the S_{21} spectra to a Lorentzian line shape [Eq. (3.2)], as shown in the insets of Figs. 3.5(a) and 3.5(b). The data are clearly well described by Lorentzians with center frequencies of around 4.8 GHz and quality factors determined from the curve fits of $Q_A = 2500$ and $Q_B = 3750$. These values agree reasonably well with the total Q expected from the intrinsic Q and the loading due to coupling capacitors [as in Subsection 2.1.3]. The addition of dc feed line structure therefore, does not have a significant effect on the Q of the first harmonic mode at the temperature (4.2 K) of our measurements.

Finally, we apply a 1V dc voltage bias or 1mA dc current bias to the center conductor of the resonators via the bias lines. The resulting transmission S_{21} spectra are nearly unperturbed by the dc bias, as shown in Figs. 3.5(a) and 3.5(b). The quality factors of the resonators as determined by fits to a Lorentzian line shape degrade by less than 1% under application of dc bias. We conclude that the application of dc bias does not significantly disturb the first harmonic cavity mode, as expected for our design.

3.5 Discussions

To investigate the origin of the additional resonances at 3.2 and 3.6 GHz, we simulated the transmission spectra of the resonators using Microwave Office [47], as shown in Fig. 3.4(b). The loss tangent of the Nb film $\tan\delta = 1.6 \times 10^{-4}$ was chosen to agree with the intrinsic Q of the bare resonator C. We take the dielectric constant of the Si substrate to be $\varepsilon = 11.9$. An effective length for the resonator $l_{eff} \approx 1.04l$ was also chosen to give the best agreement between the measured resonant frequencies for both resonators

A and B. This fitting procedure accounts for small ($\sim 4\%$) discrepancies between the measured and predicted resonant frequencies that are likely due in part to the effects of the kinetic inductance of the Nb film [as discussed in Subsection 2.2.2]. The simulations show good agreement with experimental data for resonators A in Fig. 3.4(b). The full-wave resonance of the main line at 4.8 GHz in Fig. 3.4(a) appears smaller than theory [as in Fig. 3.4(b)] due to the relatively coarse sampling used in the measurement.

The broad resonances at 3.2 and 3.6 GHz are also clearly reproduced in the simulations. Comparison between the simulations and data allows us to identify these resonances as arising from the fundamental resonance of the $3\lambda/4$ length of CPW between port 1 and port 4, and from the first harmonic resonance of the $5\lambda/4$ length of CPW between port 1 and port 3, respectively [see Fig. 3.1]. The resonant frequency of the $5\lambda/4$ section of CPW is pulled downward significantly by the reactance of the $\lambda/4$ section of transmission line [35] from the second bias line to the output at port 2.

To more carefully study the characteristics of the resonators near the full-wave resonance we measured and simulated the same S parameters over a much narrower frequency range immediately around f_0, as shown in Figs. 3.4(c) and 3.4(d) for resonator B; agreement between the measurements and simulations is excellent. The resonance in S_{21} for the main line has a narrow Lorentzian line shape as mentioned above. Transmission through the dc bias lines as shown in Fig. 3.4(c) for S_{31} and S_{41} displays more complex behavior. These resonances are well described by the Fano line shape [48], which generically results from mixing between a discrete state and a continuum. In our case, the continuum arises from the tails of the broad resonances associated with the dc bias lines while the discrete

state is the narrow full-wave resonance of the main line. When a photon is transmitted to one of the dc bias lines it may either couple directly to the bias line, or first couple to the main resonance and then to the bias line. Interference between these two pathways is destructive on one side of the main resonance and constructive on the other, leading to the characteristic Fano line shape.

This analysis suggests an alternative interpretation of the operation of the dc-biased cavity. The dc bias line are in fact additional microwave resonators whose resonant frequencies are far from that of the main line. The bias line resonators necessarily have a low Q due to their strong dc coupling to the measurement circuitry; as a result, their resonances still have significant weight a the frequency f_0 of the main resonance. Mixing with the sharp main line resonance occurs at f_0, allowing some fraction of the photons in the main line to escape via the bias lines. Nonetheless, the mixing is relatively weak; as can be seen in Figs. 3.4(c) and 3.4(d), the peak values of S_{31} and S_{41} at f_0 are about 13 dB less than that of S_{21}, indicating that less than 2.5% of the input power escapes through the dc bias lines. Coupling to the bias lines can be further weakened by using a larger terminating inductance L, which increases the bias line Q and narrows their resonances. For instance, using $L = 20$ nH increases the bias line isolation to roughly 20 dB.

3.6 Conclusion

The ability to introduce a dc bias into a high-Q superconducting microwave cavity is an important addition to the circuit QED architecture. With dc access to the cavity, highly non-linear devices can be developed by embedding current- or voltage-biased Josephson structures such as superconducting quantum interference devices (SQUIDs) or Cooper pair transistors (CPT) in the cavity. The dc-biased cavity may also serve as a general platform allowing very strong coupling between the cavity and a variety of quantum systems. Indeed, the dc current and voltage biased applied above are sufficiently large to achieve strong coupling between a nanomechanical resonator and qubits embedded in such a cavity [45].

Chapter 4

The Cavity-Embedded-Cooper Pair Transistor

Since the 1990s, a great interest has been raised in single charge tunneling effects in systems with small junctions at low temperatures [49]. Among these systems, the single electron transistor (SET), hereafter called the single Cooper pair transistor (CPT), is one of the simplest and most extensively studied devices.

In this dissertation, we focus on the supercurrent regime of the superconducting CPT, where Cooper pairs are the dominant charge carriers. The SET is more commonly referred to, when one discusses the normal state SET or superconducting SET in higher bias regime, where charge carriers such as quasiparticles are involved.

4.1 Josephson Junction, Josephson Effects & Inductance

A superconducting tunnel junction, also known as a Josephson junction (JJ) [50, 51] , refers to two superconducting electrodes separated by a thin insulating barrier [see Fig. 4.1)(a)], or more generally, a weak link [40]. It is the only non-linear and non-dissipative quantum circuit element at arbitrarily low temperature [18]. The discussion in Sections 4.1 and 4.4 follow that in Tinkham [40].

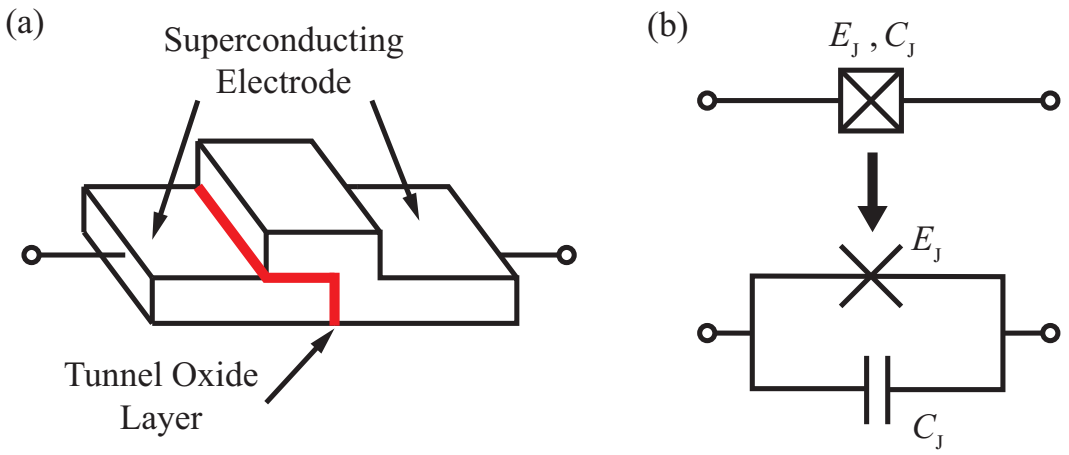

FIGURE 4.1: (a) A superconductor-insulator-superconductor (SIS) Josephson junction. (b) Schematic representation of a Josephson junction, in which the Josephson element is represented by a cross.

In 1962, Josephson [50, 51] predicted that at a zero bias voltage, a supercurrent

$$I_s = I_c \sin \varphi \tag{4.1}$$

should flow through the Josephson junction, known as dc Josephson effect. Here φ is the phase difference of the two electrodes and I_c is the critical current of the tunnel junction. He also predicted that if a bias voltage is applied across the junction, the time

derivative of the phase difference is determined by,

$$\dot{\varphi} = \frac{2e}{\hbar} V_{\mathrm{JJ}} \,. \tag{4.2}$$

The supercurrent thus would be an alternating current with amplitude I_c and frequency $f = 2eV/h$. It also indicates that a Cooper pair tunnels through the junction in each period using the energy quantum hf. Eq.(4.2), known as ac Josephson effect, arises from the very basics of quantum mechanics and is therefore a direct consequence of the coherence of Cooper pair tunneling.

Using Eq.(4.1) and (4.2), one can compute the energy stored in the junction by integrating the external electrical work,

$$E = \int I_s V dt = \int I_c \sin\varphi d\varphi = -E_J \cos\varphi + const. \tag{4.3}$$

where $E_J \equiv \hbar I_c/2e$ is defined as the Josephson energy. This suggests that E_J or I_c can be treated as a measure of the coupling strength of the superconducting electrodes. I_c scales proportionally to the area of the tunnel layer and decreases exponentially with the tunnel layer thickness.

Energy storage and conservation suggest that, a Josephson junction can be considered as having a nonlinear reactance, inductive or capacitive, depending on the observation point of the whole circuit. Generally speaking, the inductance of a electrical element

can be defined as

$$L = \frac{\Phi(t)}{I(t)} \tag{4.4}$$

where the magnetic flux $\Phi(t) = (\Phi_0/2\pi)\varphi(t)$, and $\Phi_0 = h/2e$ is the flux quantum. For elements that do not form a loop, the branch flux can be defined as $\Phi(t) = \int_{-\infty}^{t} V(s)$ ds, where $V(s)$ is the space integral of the electric field along a current line inside the element [18]. Hence, the Josephon inductance of a JJ is

$$L_J(\varphi) = (\frac{dI}{d\Phi})^{-1} = \frac{\hbar}{2eI_c \cos\varphi} = \frac{L_J}{\cos\varphi} \tag{4.5}$$

where $L_J = \hbar/2eI_c$. For small signals, a single JJ thus behaves as a phase-dependent nonlinear inductor in parallel with the capacitance formed by the two overlapping films of the junction, as shown in Fig. 4.1(b). In fact, the Josephson inductance arises from the inertia of Cooper pairs tunneling across the junction, which is essentially the kinetic inductance, as discussed in Subsetion 2.2.2.

4.2 Cooper Pair Transistor (CPT)

A Cooper pair transistor (CPT) consists of two ultra small Josephson junctions connected in series and a small island in between, usually with a gate electrode capacitively coupled to the island, as illustrated in Fig. 4.2.

The CPT can also be considered as a split Cooper pair box (CPB) [52], whose JJs do not form a superconducting loop but are rather connected to an external circuit. The CPB

is widely used as a superconducting charge qubit in quantum computing applications [21]. Even though this dissertation focuses on the physics of the CPT not its direct application in general, the insights gained from the CPB are still very helpful for our study of the CPT.

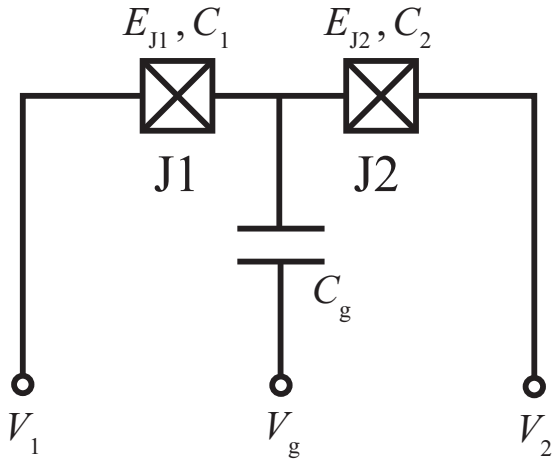

FIGURE 4.2: Schematics of the Cooper Pair Transistor.

To observe single Cooper pair tunneling effects, two requirements need to be met. First, the Coulomb charging energy of a single Cooper pair, $E_{C_J} = (2e)^2/2C_\Sigma = 2e^2/C_\Sigma$, must be significantly larger than the thermal fluctuations at ambient temperature T,

$$E_{C_J} = 2e^2/C_\Sigma \gg k_B T \tag{4.6}$$

where $C_\Sigma = C_1 + C_2 + C_g$ is the total capacitance of the island. This requires that $C_\Sigma \ll 40$ fF at $T \approx 0.1$ K, which explains why we need to fabricate ultra small junctions and cool the device to low temperatures.

Second, the normal resistance R_T of a tunneling junction must be greater than the quantum resistance for a Cooper pair $R_Q = R_K/4 = h/4e^2$, that is

$$R_T > h/4e^2 \approx 6.5\,\mathrm{k}\Omega. \tag{4.7}$$

This is because the Coulomb charging energy of a Cooper pair E_{cp} must exceed the quantum energy uncertainty $\Delta E \geq h/\tau \approx h/R_T C_\Sigma$ associated with the charge lifetime due to Cooper pair tunneling $\tau = R_T C_\Sigma$. Eq.(4.7) ensures that the wave function of the excess Cooper pair is localized on the island.

In practice, aluminum is the most commonly chosen material for fabricating superconducting JJs. It is often said that aluminum is to superconducting circuits what silicon is to conventional MOSFET circuits [18]. A sandwich structure of $\mathrm{Al/AlO_x/Al}$ is usually made by the double-angle shadow evaporation. The naturally grown high quality aluminum oxide layer (thickness $\sim$ 1 nm) acts as the insulating tunneling barrier. The capacitance of the tunneling junctions make up for the most part of the capacitance of the island. Below the critical temperature of Al (1.2 K), the source and drain electrodes as well as the island are superconducting.

As discussed in Section 4.1, besides the charging energy E_c and the thermal energy $k_B T$, another two energy scales, i.e. Josephson energy E_J and the superconducting energy gap Δ, also come into play for superconducting Josephson junctions. In fact, E_J is related

to Δ by the Ambegaokar-Baratoff relation [53],

$$E_J = \frac{h\Delta}{8e^2 R_T} \tag{4.8}$$

where R_T is the normal resistance of the CPT.

If $E_J \gg E_{C_J}$, the phase difference φ across the CPT is well defined and the number of Cooper pairs N on the island undergoes large fluctuations. If instead $E_{C_J} \gg E_J$, the number of Cooper pairs on the island is well defined, and the system is governed by the charging energy of the island. In this dissertation, we are most interested in the regime $E_J < E_{C_J} < \Delta$, where the number N is still well defined, while Cooper pair tunneling is maximized at the same time. Under the above condition that $E_J < E_{C_J} < \Delta$ and Eqs. (4.6) (4.7), the CPT is in the well-knowned Coulomb blockade regime.

4.3 Transport in CPT

4.3.1 Tunneling Process in Single Josephson Junction

Although we are primarily concerned with Cooper pair tunneling in this dissertation, to get a bigger picture it is still worth mentioning other tunneling mechanisms.

Let's start with a single superconductor-insulator-superconductor (SIS) junction. It is convenient to treat the superconductor using *semiconductor model* [40], in which the superconductor is represented by an ordinary semiconductor with a density of independent-particle energy states, as shown in Fig. 4.3.

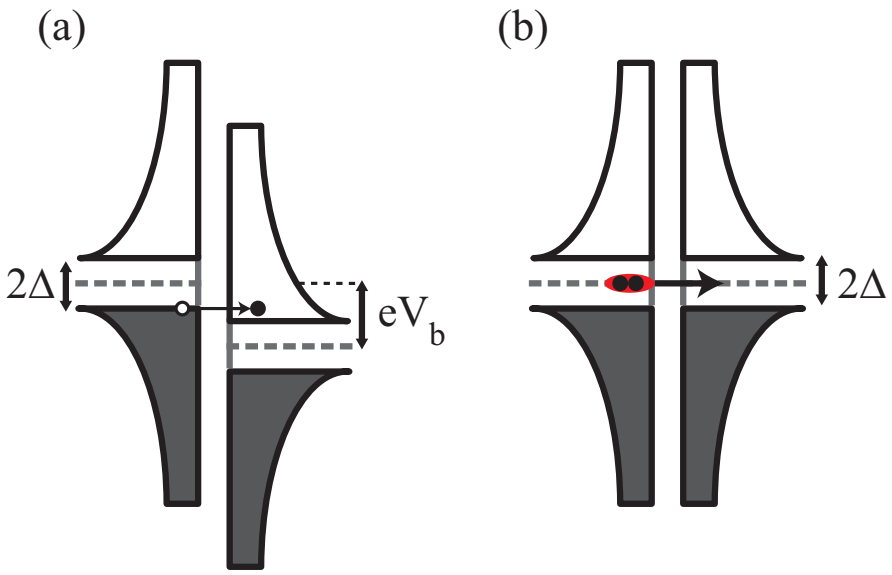

FIGURE 4.3: Semiconductor model of an SIS junction. (a) Dissipative quasiparticle tunneling when $eV_{\rm dc} > 2\Delta$. (b) Resonant Cooper pair tunneling when $eV_{\rm dc} = 0$.

In an SIS junction in general, besides resonant Cooper pair tunneling, quasiparticles can also tunnel through the barrier. At $T = 0$, for a bias voltage $eV_{\rm dc} > 2\Delta$, where 2Δ is the superconducting energy gap of the electrodes, the minimum energy to break a Cooper pair into two quasiparticles according to the BCS theory. In this case, the transport process is dominated by dissipative quasiparticle tunneling. On the other hand, for a bias voltage $eV_{\rm dc} < 2\Delta$, no quasiparticle can be created and only resonant Cooper pair tunneling can cause supercurrent to flow through the junction, if the Fermi energy levels of the two electrodes are aligned.

4.3.2 Tunneling Process in CPT

In reality, a CPT composed of double SIS junctions is much easier to implement and measure than a single junction, because the island is well isolated from the low-impedance

environment by the high resistance and low capacitance double junctions. Fig. 4.4 shows current features of a CPT over a large range of bias voltage.

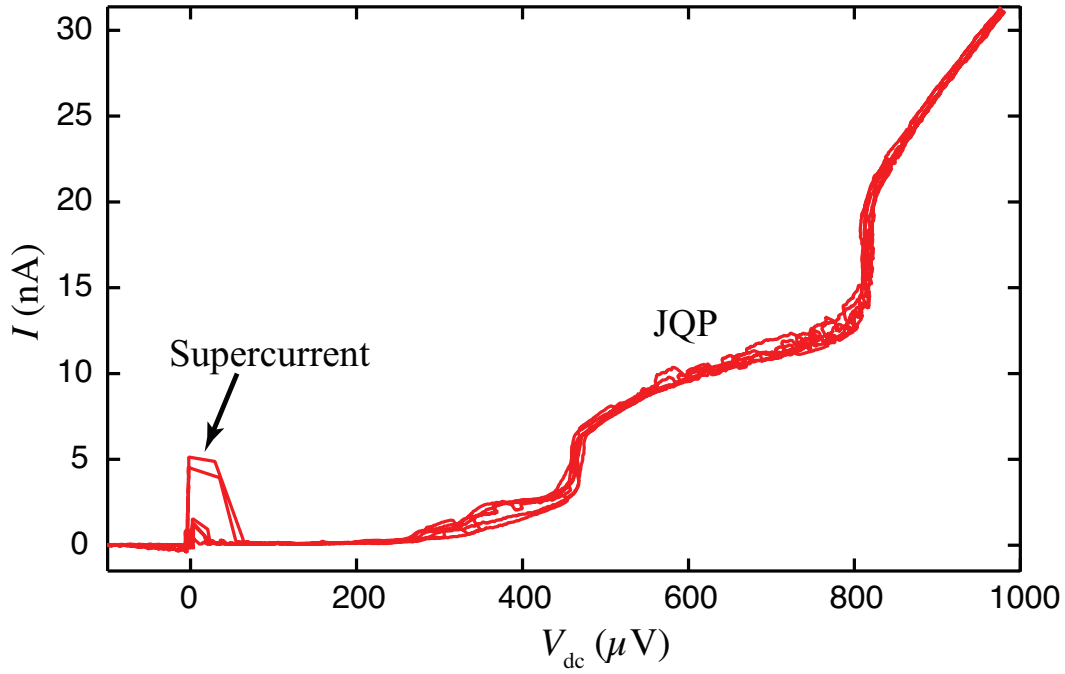

FIGURE 4.4: A collection of I-V curves of a CPT taken at various gate voltages. It clearly shows the super current peaks and JQP peaks. DJQP peaks are not present due to a relatively small charging energy: $E_c < \frac{2}{3}\Delta$

Depending on the relative sizes of the voltage bias $V_{\rm dc}$, the superconducting gap energy Δ and the charging energy for a single electron $E_c = e^2/2C_\Sigma$, the transport process can be divided into several regimes. In the above-gap regime, $eV_{\rm dc} > 4\Delta$, the transport is dominated by sequential quasiparticle tunneling, just as for a single SIS junction.

In the sub-gap regime, apart from the supercurrent peaks, there are a number of different tunneling mechanisms that involve a combination of Cooper pairs and quasiparticles [54]. Two of the most prominent current peaks are the Josephson-quasiparticle cycle (JQP) [55] and the double Josephson-quasiparticle cycle (DJQP) [56].

The JQP cycle is a 3-step process, in which a Cooper pair tunnels through one junction, followed by the subsequent quasiparticle tunneling through the other junction. It requires that $eV_{\rm dc} > E_c + 2\Delta$.

The DJQP cycle is a combination of two Cooper pair tunneling steps interleaved by two quasiparticle tunneling steps. It is sometimes called the 3e process since three electrons in total tunnel at each junction. The Cooper pair resonant tunneling condition dictates that $eV_{\rm dc} = 2\Delta$, and to have quasiparticle tunneling to occur at this voltage, another energy requirement need to be met: $E_c > \frac{2}{3}\Delta$ [54].

The feature we are most interested in is the supercurrent peak, where the bias voltage is close to zero and the transport is dominated by the resonant Cooper pair tunneling. As mentioned in the previous subsection, for a bare junction, the resonant tunneling condition is: $2eV_{\rm dc} = 0$. For a double junction CPT, the charging energy needs to be taken into consideration. Assume that an asymmetrically biased SET [see Fig. 4.2] has junction J2 grounded ($V_2 = 0$) and a bias voltage $V_{\rm dc}$ is applied via junction J1 ($V_1 = V_{\rm dc}$). As far as the voltage across each junction is concerned, the CPT just acts like a capacitance divider. Using Kirchhoff's law, one can easily derive the Cooper pair tunneling condition [54, 57]:

$$\sum_i \kappa_i \, m_i \, eV_{\rm dc} = 2\,\delta m\, E_c(n - n_g + \delta m/2) \tag{4.9}$$

where $m_{1(2)}$ is the number of electrons tunneling across junction J1(2), $\delta m = m_2 - m_1$, n is the initial charge state of the island, $n_g = C_g V_g/e$ is the number of offset gate

charge, and $\kappa_{1(2)}$ is the fraction of the bias voltage dropped across J1(2). In this case, $\kappa_1 = (C_2 + C_g)/C_\Sigma$ and $\kappa_2 = C_1/C_\Sigma$.

The advantage of working in this regime is, in contrast to quasiparticle tunneling, Cooper pair tunneling is both coherent and non-dissipative.

4.4 Quantum Mechanics in the Supercurrent Regime

4.4.1 Quantum Mechanics of the Single Josephson Junction

As discussed in Section 4.2, we are working in the regime $E_J \approx E_{C_J} < \Delta$, where the number of Cooper pairs N on the island is still well defined, while the coupling between the island and the leads is maximized. In fact, the quantum uncertainty relation $\Delta\varphi\Delta N \geq 1$ modifies the classical theory of the Josephson effects in Section 4.1, where the phase difference φ is treated as a classical variable, implying the implicit assumption that $E_J \gg E_{C_J}$.

Again we start with the simplest case, i.e. an isolated single Josephson Junction with capacitance C at $T = 0$. The classical expression for the total energy is

$$E = \frac{Q^2}{2C} - E_J \cos\varphi. \tag{4.10}$$

The JJ phase difference φ is related to the magnetic flux Φ via $\varphi = (2\pi/\Phi_0)\Phi = (2e/\hbar)\Phi$, where $\Phi_0 = h/2e$ is the flux quantum. The operator Φ and Q obey the canonical

coordinate-momentum commutation relation $[\Phi, Q] = i\hbar$. Hence,

$$[\varphi, Q] = 2ei. \tag{4.11}$$

Making the operator replacement $Q = 2ei\frac{\partial}{\partial\varphi}$ in Eq.(4.10), we get the Hamiltonian for a single JJ,

$$H = -4E_c\frac{\partial^2}{\partial\varphi^2} - E_J\cos\varphi \tag{4.12}$$

where $E_c = e^2/2C$. We should keep in mind that this Hamiltonian describes only the tunneling of Cooper pairs and neglects that of quasiparticles at $T \to 0$.

4.4.2 Quantum Mechanics of the CPT

Now we move on to discuss the CPT in the supercurrent regime [as in Fig. 4.2]. We denote the Josephson energies of the two junctions by E_{J1} and E_{J2}. The total capacitance of the island $C_\Sigma = C_1 + C_2 + C_g$. At zero bias voltage, the energy of the CPT is given by the Hamiltonian

$$H = -E_{J1}\cos\varphi_1 - E_{J2}\cos\varphi_2 + \frac{(Q - Q_g)^2}{2C_\Sigma} \tag{4.13}$$

where $Q_g = C_gV_g = e\,n_g$ is the gate charge, φ_1 and φ_2 are the phase differences across junctions J1 and J2, respectively.

We define the new variables $\gamma_\pm = (\varphi_1 \pm \varphi_2)/2$ [58], where γ_+ is the average phase difference across the double junctions (i.e. the 'center of mass', CoM coordinate) and γ_-

is the relative phase of the two junction. In our CPTs, $E_J \sim E_c$, so γ_+ can be considered as a semiclassical variable. In contrast, γ_- is a quantum variable that describes quantum fluctuations of the system.

Replacing φ_1 and φ_2 in Eq.(4.13) by $\gamma_\pm$, we have

$$H = -E_J(\gamma_+)\cos(\gamma_- - \chi) + \frac{(Q-Q_g)^2}{2C_\Sigma} \tag{4.14}$$

where

$$E_J(\gamma_+) = \sqrt{E_{J1}^2 + E_{J2}^2 + 2E_{J1}E_{J2}\cos\gamma_+} \tag{4.15}$$

and

$$\chi = \arctan(\frac{E_{J1}-E_{J2}}{E_{J1}+E_{J2}}\tan\gamma_+). \tag{4.16}$$

Since the eigenvalues of the Hamiltonian do not depend on the phase reference χ, we can drop it and rewrite H as

$$H = -E_\mathrm{J}(\gamma_+)\cos(\gamma_-) + \frac{(Q-Q_\mathrm{g})^2}{2C_\Sigma}. \tag{4.17}$$

Here γ_- and Q also obey the commutation relation $[\gamma_-, Q] = 2ei$. Apart from a semiclassical gate charge $Q_g = n_g\, e$, this equation is equivalent Eq.(4.12) for a single isolated JJ. Due to environmental effects, the double JJ system is a more realistic physical system to fabricate and measure. Fig. 4.5 shows that for sufficiently small bias voltage V_dc, the CPT current is $2e$ periodic (period 69.4 mV in V_g, as opposed to period 34.7 mV in V_g in the quasiparticle regime), as is expected from the Hamiltonian (4.17) in the

supercurrent regime.

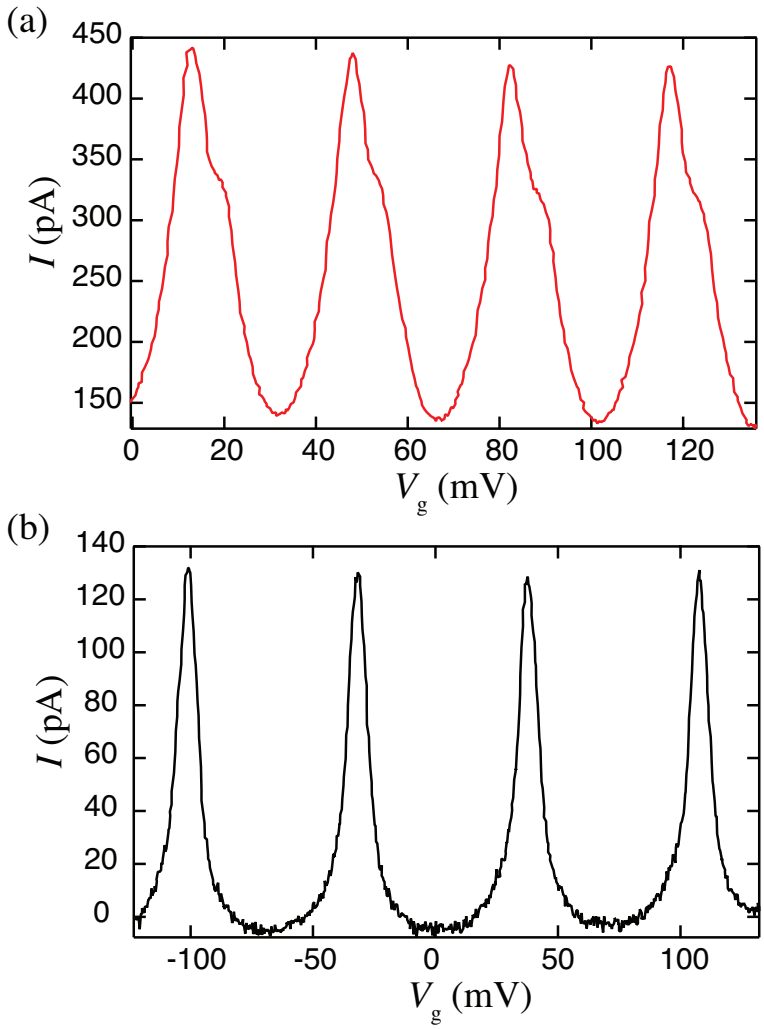

FIGURE 4.5: (a) A gate voltage sweep of a CPT at relatively high source-drain (i.e. quasiparticle regime), which shows a gate voltage period of 34.7 mV. (b) A gate voltage sweep of a CPT at low bias (i.e. supercurrent regime), which has a gate voltage period of 69.4 mV.

In Section 4.1, we introduced the Josephson inductance for a single JJ. The inductance for a double junction CPT can be described similarly. Note that changes of flux and the system energy $E(\varphi, n_g)$ are related by $dE = Id\Phi$, thus the inductance of the system can

be derived as [59]

$$L_{\mathrm{CPT}} = (\frac{dI}{d\Phi})^{-1} = (\frac{d^2E}{d\Phi^2})^{-1} = (\frac{\Phi_0}{2\pi})^2(\frac{d^2E}{d\varphi^2})^{-1} \tag{4.18}$$

where $\varphi = 2\gamma_+ = (2\pi/\Phi_0)\Phi$ is the total phase difference across the CPT. The CPT in the supercurrent regime can therefore be treated as an inductor with a gate-tunable inductance $L_{CPT}(\varphi, n_g)$. Based upon this result, a device called the inductive SET (L-SET) [60] has been invented as a high sensitivity charge detector, taking advantage of non-dissipative Cooper pair tunneling.

4.5 The Cavity-Embedded-Cooper Pair Transistor (cCPT)

We now turn to the the cavity-embedded-cooper pair transistor (cCPT), the main focus of this dissertation. Having demonstrated the dc biasing scheme integrated in the standard circuit QED architecture in Chapter 3, as well as the basic understanding of the quantum mechanics of a CPT on its supercurrent branch, we are finally ready to discuss the cCPT.

We embed the CPT in a dc-biased CPW cavity at at the center of the full-wave resonator, as illustrated in Fig. 4.6. Located at the central voltage antinode, the CPT enjoys a strong electric field which facilitates the strong coupling to the cavity. In addition, it has its source electrode in direct electrical contact with the center conductor and its drain electrode connected to the ground plane of the CPW.

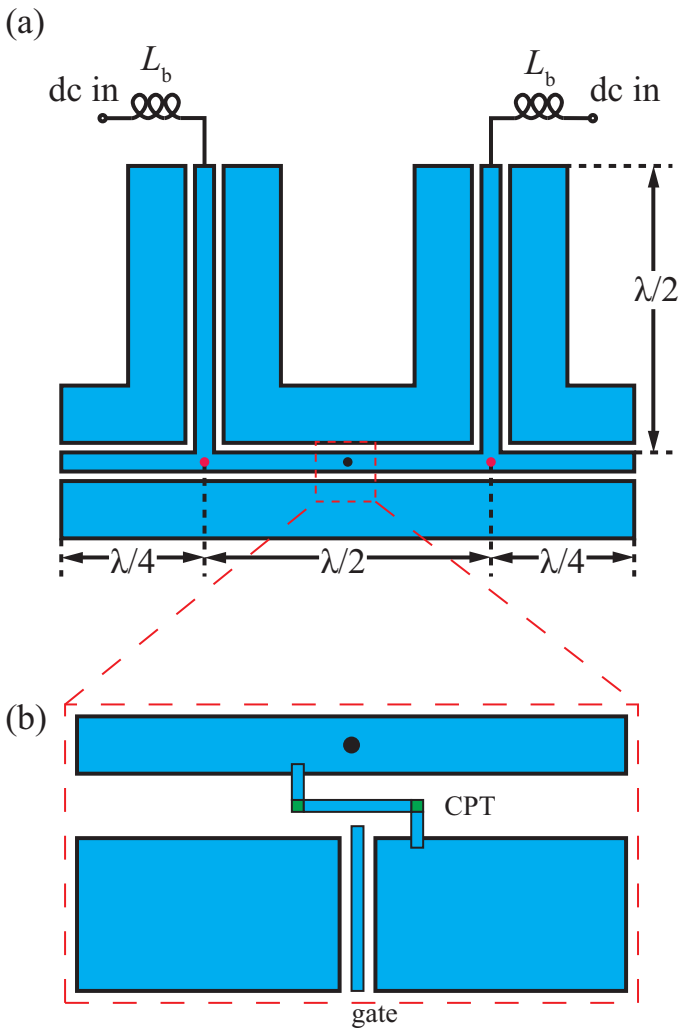

FIGURE 4.6: (a) Schematic diagram of a full-wave dc-biased superconducting CPW cavity showing the CPT location (black dot) at the center of the main cavity line. (b) Expanded view of the CPT/cavity connection with a gate line capacitively coupled to the island of the CPT. The double JJs of the CPT are shown in green.

Due to the ac Josephson effect, we can expect that for a properly chosen bias voltage, the CPT will begin to emit photons into the cavity; effectively we will use the ac Josephson effect to "ring" the cavity up. However, the CPT is also strongly coupled to the high Q cavity field, so we can not use the usual theory of energy exchange with the electromagnetic environment (the so-called $P(E)$ theory) to treat the interaction

between the CPT and the cavity. An implicit assumption in the $P(E)$ theory is that the environment is in thermal equilibrium, which is certainly not true for the cavity in our system. A full theoretical treatment must address the CPT/cavity as *a single quantum system* (i.e. the cCPT system), and not simply a CPT embedded in an electromagnetic environment. This use of the quantum transport in a nanoscale structure (the CPT) to determine the motion of a much larger structure (the cavity) is in many ways similar to the use of the quantum point contact (QPC) shot noise to "ring up" the crystal in which it is embedded [61]. The theoretical analysis in this section follows the discussion in Blencowe *et al.* [62].

4.5.1 Classical Model of the cCPT

A simplified lumped-element model of the cCPT system is shown in Fig. 4.7. It is supposed that for a small external dc bias $V_{\rm dc}$, the CPT interacts predominantly with a particular mode of the cavity, with the other modes and their coupling to the environment modeled as a resistance. Thus the CPW resonator can be modeled as a parallel LCR circuit [as in Chapter 2], which is in parallel with the CPT. For simplicity and practical approximation, we assume that the CPT has symmetric double junctions, which have the same critical current I_c (i.e. same Josephson energy E_J) and same capacitance C_J. Considering the typical values of our device: $L_b \sim$ a few nH, $L \sim$ tenths of nH, $C \sim$ a few pF, $C_J \sim 1$ pF and $C_g \sim$ a few aF, we have the size hierarchies $L_b \gg L$ and $C \gg C_J \gg C_g$.

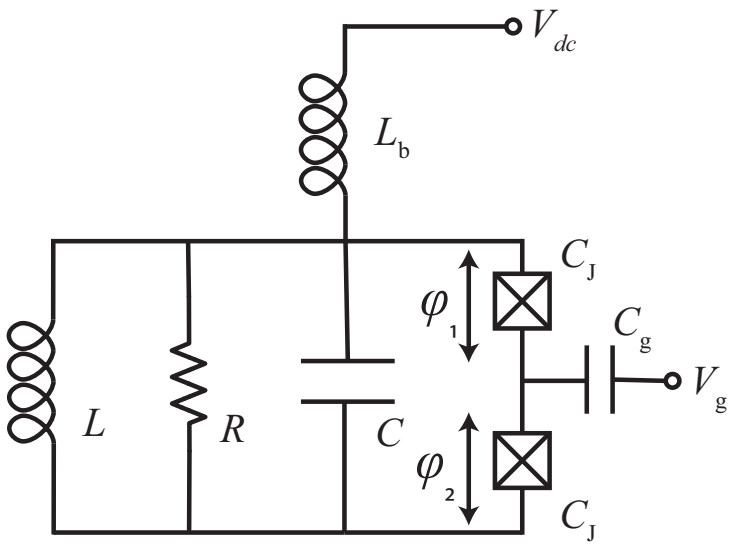

FIGURE 4.7: Effective lumped-element model of the cCPT system.

Using Kirchhoff's laws and assuming $L \ll L_b$, the classical equations of motion for the circuit can by derived in terms of the phase difference across each junction:

$$(C + C_J)\ddot{\varphi_1} + C\ddot{\varphi_2} + R^{-1}(\dot{\varphi_1} + \dot{\varphi_2}) + L^{-1}(\varphi_1 + \varphi_2 - \varphi_{10} - \varphi_{20}) = -\frac{2\pi I_c}{\Phi_0}\sin\varphi_1 + \frac{2\pi}{\Phi_0}L_b^{-1}V_{\rm dc}t \tag{4.19}$$

and

$$(C + C_J + C_g)\ddot{\varphi_2} + C\ddot{\varphi_1} + R^{-1}(\dot{\varphi_1} + \dot{\varphi_2}) + L^{-1}(\varphi_1 + \varphi_2 - \varphi_{10} - \varphi_{20}) = -\frac{2\pi I_c}{\Phi_0}\sin\varphi_2 + \frac{2\pi}{\Phi_0}L_b^{-1}V_{\rm dc}t + \frac{2\pi}{\Phi_0}C_g\dot{V}_g. \tag{4.20}$$

We again define the CoM and relative phase coordinates $\gamma_\pm = (\varphi_1 \pm \varphi_2)/2$ and use the relation $C \gg C_J \gg C_g$, Eqs. (4.19) and (4.20) then become

$$C\ddot{\gamma_+} + R^{-1}\dot{\gamma_+} + L^{-1}(\gamma_+ - \gamma_+^0) = -\frac{\pi I_c}{\Phi_0}\sin\gamma_+\cos\gamma_- + \frac{\pi}{\Phi_0}L_b^{-1}V_{\rm dc}t \tag{4.21}$$

and

$$C_J\ddot{\gamma_-} = -\frac{2\pi I_c}{\Phi_0}\sin\gamma_-\cos\gamma_+ - \frac{\pi}{\Phi_0}C_g\dot{V_g}. \tag{4.22}$$

The oscillator frequency on the left hand side of Eq.(4.21) is $\omega_0 = 1/\sqrt{LC}$ and we define the dimensionless time unit $\tau = \omega_0 t$. Eqs.(4.21) and (4.22) can then be expressed in a dimensionless form,

$$\ddot{\gamma_+} + Q^{-1}\dot{\gamma_+} + \gamma_+ - \gamma_+^0 = -f_0\sin\gamma_+\cos\gamma_- + \omega_d^0\tau \tag{4.23}$$

and

$$\eta_J\ddot{\gamma_-} = -2f_0\sin\gamma_-\cos\gamma_+ - \eta_g\dot{\tilde{V}_g}, \tag{4.24}$$

where the quality factor is $Q = R\sqrt{\frac{C}{L}}$, the dimensionless 'force amplitude' is

$$f_0 = \pi\frac{LI_c}{\Phi_0}, \tag{4.25}$$

the dimensionless 'driving frequency' is

$$\omega_d^0 = \frac{L}{L_{\rm b}}\frac{eV_{\rm dc}}{\hbar\omega_0}, \tag{4.26}$$

and $\eta_J = C_J/C$, $\eta_g = C_g/C$, $\tilde{V}_g = eV_g/\hbar\omega_0$. Transforming to the 'shifted' coordinates $\tilde{\gamma_+} = \gamma_+ - \gamma_+^0 - \omega_d^0\tau + \omega_d^0/Q$ and $\tilde{\tau} = \tau + Q^{-1}$, the equations of the motion of the cCPT system finally become,

$$\ddot{\gamma_+} + Q^{-1}\dot{\gamma_+} + \gamma_+ = f_0 \sin\left(\omega_d^0\tau + \gamma_+\right)\cos\gamma_- \tag{4.27}$$

and

$$\eta_J\ddot{\gamma_-} = 2f_0 \sin\gamma_- \cos\left(\omega_d^0\tau + \gamma_+\right) - \eta_g\dot{\tilde{V}}_g \tag{4.28}$$

where we have set $\gamma_+^0 = \pi$ and dropped the tildes except for $\tilde{V}_g$. For small force amplitude and driving frequencies close to the left side oscillator frequency, $\omega_d^0 \sim 1$, Eq.(4.27) behaves like a driven, damped harmonic oscillator. For typical force amplitude $f_0 \sim 0.1$ and a Q of several thousand, $f_0 Q \gg 1$ and the system is strongly nonlinear. In addition, Eq.(4.28) describes the internal phase fluctuations of the CPT. Note that the system is not described by the Duffing oscillator as discussed in Section 1.1. Instead, both Eqs.(4.27) and (4.28) have a time dependent drive as a result of the ac Josephson effect and the drive frequency can be tuned by an external dc bias $V_{\rm dc}$. In contrast to most systems that require an external ac drive, the cCPT system generates it own ac drive and the strongly nonlinear system self-oscillates.

Using Eqs.(4.21) and (4.22) and a canonical transformation, the Hamiltonian of the cCPT system can also be expressed as

$$H = (\frac{\pi}{\Phi_0})^2(2C)^{-1}p_+^2 + (\frac{\Phi_0}{\pi})^2(2L)^{-1}\gamma_+^2 + E_{\mathrm{C_J}}(N - N_{\mathrm{g}})^2$$
$$- 2E_{\mathrm{J}}\cos\gamma_-\cos(\gamma_+ + \omega_{\mathrm{d}}t) \tag{4.29}$$

where $N = p_-/\hbar$ is the number of Cooper pairs on the island, $N_g = n_g/2 = C_gV_g/(2e)$ is the gate charge in units of Cooper pairs, $E_{C_J} = (2e)^2/(2C_\Sigma) \approx (2e)^2/(2\cdot 2C_J) = e^2/C_J$ is the approximate Cooper pair charging energy neglecting C_g, and $\omega_d = \omega_d^0 \cdot \omega_0 = (L/L_b)(eV_{\mathrm{dc}}/\hbar)$ [1] is the drive frequency due to the dc bias V_{dc}.

Blencowe *et al.* [62] demonstrate that the classical dynamics of the CPT phases are chaotic, as well as aperiodic depending on the initial conditions and the nature and strengths of the damping/noise forces. Classically the CPT island phase looks like a very light pendulum attached to a very large mass (the cavity) on a very stiff spring.

4.5.2 Quantum Model of the cCPT

To derive the quantum counterpart of Hamiltonain (4.29), we note that the quantum commutation relations for the phases are

$$[N, \gamma_-] = i; \quad [\gamma_+, p_+] = i\hbar. \tag{4.30}$$

[1] A more recently developed model [63] taking into consideration the distributive nature of the CPW shows that the effective driving frequency should be $\omega_d = eV_{\mathrm{dc}}/\hbar$. Nevertheless, the physics implied by this model is essentially the same as the model discussed in this section.

Introducing the creation operator a and annihilation operator a^+ for the cavity photons, we have

$$\gamma_+ = \sqrt{\frac{\hbar}{2m\omega_0}}(a + a^+); \quad p_+ = \sqrt{\frac{m\omega_0\hbar}{2}}(a - a^+) \tag{4.31}$$

where the effective 'mass' $m = C(\Phi_0/\pi)^2$. Thus the size of zero point fluctuations of the average phase γ_+ is

$$\Delta_{\rm zp} = \sqrt{\frac{\hbar}{2m\omega_0}} = \sqrt{\frac{Z_0}{R_{\rm K}}} \approx 0.04 \tag{4.32}$$

where $Z_0 = \pi\sqrt{L/C} \approx 50\,\Omega$ is the characteristic impedance of the cavity transmission line, and $R_K = h/e^2 \approx 25.8\,k\Omega$ is the resistance quantum given by the von Klitzing constant. Working in the Cooper pair number state basis of the island $|N\rangle$, the quantum Hamiltonian can be written as

$$\begin{aligned} H = {} & \hbar\omega_0 a^+ a + E_{C_{\rm J}} \sum_{N=-\infty}^{+\infty} (N - N_{\rm g})^2 \, |N\rangle\langle N| \\ & - E_{\rm J} \sum_{N=-\infty}^{+\infty} (|N+1\rangle\langle N| + |N-1\rangle\langle N|) \cos\left[\Delta_{\rm zp}(a + a^+) + \omega_d t\right]. \end{aligned} \tag{4.33}$$

This system is reminiscent of several others in which an SET or JJ is embedded in a cavity or other structured environment [64–66]. These include recent use of an SET as a "single atom laser" [67] as well as many studies of the effects of electrical resonators on an embedded SET or JJ [68].

When the dc bias approaches that needed for the drive frequency ω_d to be resonant with the cavity, the Cooper paris in the CPT should begin to emit photons into it. The resulting cavity field will act back on the CPT, influencing transport through it. We

expect that the cavity will be strongly driven. A meaningful calculation of the quantum dynamics requires very careful treatment of the noise sources (such as the CPT gate/bias lines noise), and requires extremely large computational resources due to the size of the Hilbert space involved.

Blencowe *et al.* [62] show that corresponding to the classical chaotic/aperiodic motions, the quantum dynamics of the driven CPT exhibit such phenomena as dynamical tunneling and the generation of nonclassical states from initial classical states. Numerical simulation of the quantum and classical dynamics shows that, the transient behavior of the system can lead to highly non-classical states even when the initial state is apparently very classical. For more details of theoretical treatment and simulation, the reader should refer to Ref. [62].

4.5.3 Conclusions

In conclusion of our theoretical analysis, it is important to point out that the cCPT system has several novel characteristics that distinguish it from other systems and allows a unique approach to study of nonlinear quantum-to-classical correspondence.

(1) The system is strongly nonlinear while in a fully quantum mechanical regime. For many quantum systems, nonlinearity can only be accessed by application of large amplitude electric field. Here, only a few photons (tens of photons at most) are needed for nonlinearities to be important. Furthermore, we limit ourselves to the supercurrent

regime, in which no quasiparticles are generated by the CPT, so that the system remains fully quantum coherent.

(2) The nonlinearity can be accessed by application of a small dc bias voltage, rather than a large ac voltage. For typical values of $L \sim 0.5$ nH and $L_b \sim 5$ nH and for $\omega_0 \approx 5\,\mathrm{GHz}/2\pi$, we have $\omega_d \approx \omega_0$ for $V_{\mathrm{dc}} < 100\,\mu\mathrm{V}$. This drive voltage will be carefully filtered, allowing the system to remain in quantum regime even when strongly driven.

(3) The nonlinearity is tunable. The relative importance of the nonlinear terms in Eqs. (4.27), (4.28), (4.29) and (4.33) can be adjusted by tuning the CPT gate voltage. This may allow tuning of the dynamics from a regime in which the dynamics are more classical to on in which they are more quantum.

(4) The environment of the CPT is extremely well controlled, and the amount of external noise introduced is minimized. The major sources of external noise are the CPT gate line and bias line, which can be heavily filtered.

(5) The dynamics are unstudied experimentally, and the theory of the full cCPT system (including both CPT and cavity degrees of freedom) is unexplored. Unlike systems that can be described as a Duffing oscillator, the quantum dynamics of the cCPT have not been explored, which is the whole point of this dissertation.

Chapter 5

Design & Fabrication of the cCPT

This chapter reviews the experimental techniques involved in the development process of the cCPT, namely design, fabrication. These seemingly mundane steps, are as a matter of fact, crucial to the success of the whole experiment. One should always keep in mind that, every minor or unnoticed error here could be largely magnified and potentially come back to bite one later, even causing the failure of the whole experiment. In fact, this is unfortunately, what I devote the majority of my Ph.D. life to. I hope that the reader would learn from my lessons and after reading this chapter, become convinced that creating robust designs and fabrication processes should be put as an experimentalist's top priority.

As you will see, the design and fabrication processes of the cCPT system are so intimately related that I have divided them together in multiple sections, I have to frequently refer to one for the other. Additionally, I have found Refs. [21, 37, 69] very helpful in

engineering the circuit QED architecture, although the addition of dc bias lines certainly complicates the entire structure.

5.1 Substrate

As an old Chinese military saying goes, *grain and fodder must go ahead of the troops and horses; an army marches on its stomach.* So does a nano-device. Even before one starts the design process, one should have the substrates in hand and at least an idea of the kind of the metal the will be deposited.

Three different substrates are commonly chosen to fabricate CPW resonators, viz. bare silicon, thermally oxidized silicon and sapphire. All of them have been demonstrated to have the capability to achieve a high quality factor $Q \sim 10^6 - 10^7$. We picked high resistivity undoped silicon with only native oxide for the following reasons. First, as silicon is the *de facto* backbone of the semiconductor industry, its high quality substrates are widely and commercially available on the shelves. Second, silicon with native oxide is an excellent insulator below the liquid Helium temperature: no leakage current has been observed, if at most an 1V dc voltage bias is applied. Thus we do not need an extra step of thermal oxidization. Last but not the least, it is not until we put down CPT into the cavity did I realize that the weak conductivity of the silicon substrate at room temperature actually provides outstanding protection for the CPT against potentially damaging electrostatic discharges. Blessed by the unexpected protection, I have never blown out a single CPT made on this kind of substrate.

The substrates for fabricating all the samples discussed in this dissertation are undoped bare Si wafers that have following parameters: 3" in diameter, thickness $h = 375\,\mu$m , $\langle 100 \rangle$ oriented, relative dielectric constant $\varepsilon_r = 11.9$, a high resistivity $\rho > 10^4\,\Omega$cm.

As discussed in Subsection 2.2.3, as long as the metal of the CPW is made of superconducting materials, the internal loss is dominated by substrate dielectric loss and has very little to do with the property of the metal film. Also as shown in Subsection 2.2.1, the specific kind of metal does not affect the design of the CPW either, except for the effect of kinetic inductance. We chose Al and Nb successively, for reasons that will be clear in Section 5.4.

5.2 Design of the dc-biased CPW Resonator

When it comes to the design of a on-chip microwave cavity, in this case a CPW resonator, the three most important parameters that should instantly pop into the designer's mind are: characteristic impedance Z_0, loaded quality factor Q_L and the resonant frequency ω of the cavity. Let us examine them one after another.

Characteristic Impedance

The most straightforward parameter in a CPW design is the characteristic impedance Z_0, which is simply determined by the ratio of the center conductor width a to the ground plane separation b, i.e. $k = a/b$, as described by Eq.(2.22), subject to the condition that

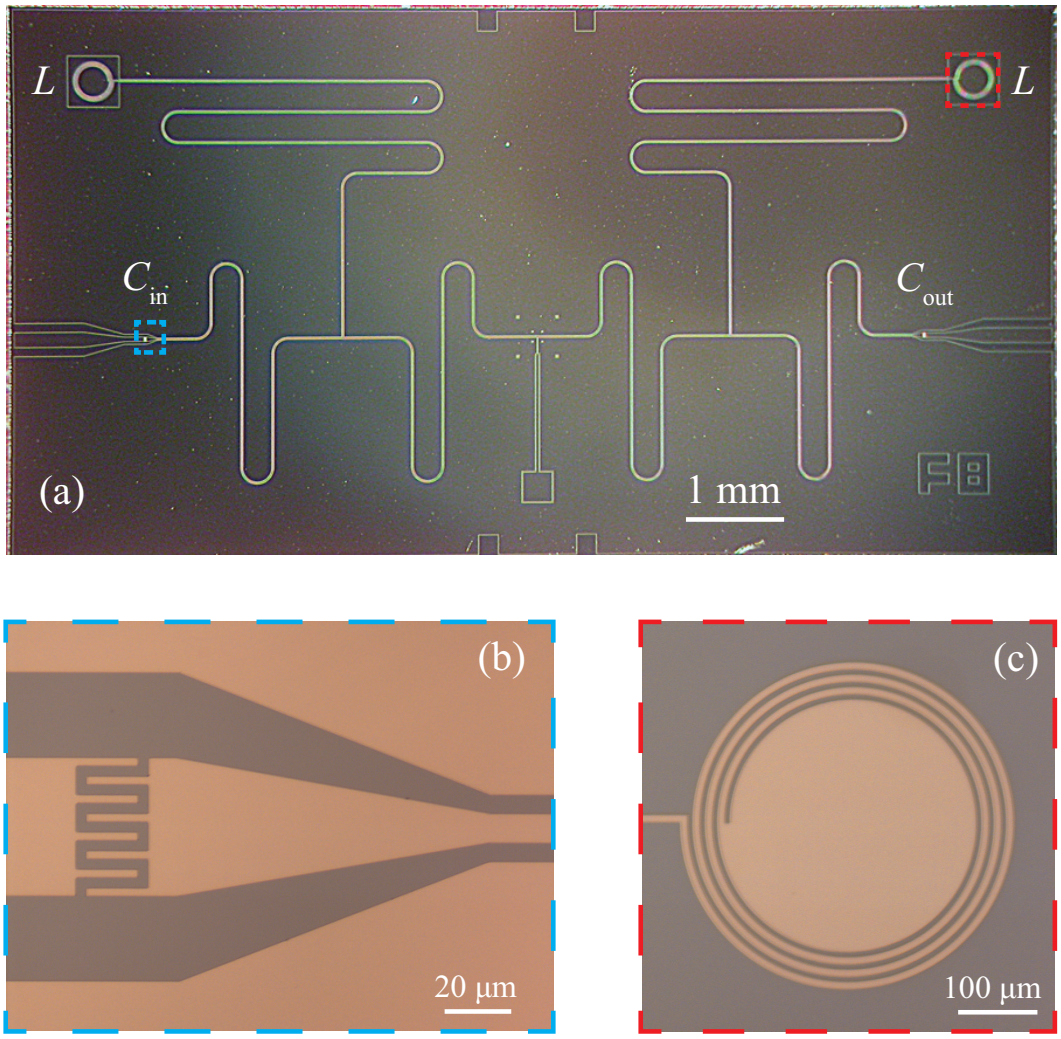

FIGURE 5.1: (a) Optical micrograph of a CPW resonator with coupling capacitors and dc feed lines terminated by inductors. Zoom-in views of (b) an 8-finger coupling capacitor and (b) a 3-turn spiral inductor.

the above dimensions are substantially smaller than the thickness of the substrate h, i.e. $a, b \ll h$, as in Fig. 2.3.

To have a characteristic impedance of $Z_0 = 50\,\Omega$, we can directly plug parameters of the substrate into Eq.(2.22), or more conveniently use free design software, such as *AppCAD* [70] and *TX-Line* [71]. Once we find the desired ratio, we are still free to

select the absolute scale of a and b over a wide range. We would like to keep the gap size $s = (b - a)/2$ small so that the EM field is tightly confined to a small volume, and yet we want to the gap big enough to accommodate the embedded CPT. It turns out that if we have the center conductor width to be $a = 10\,\mu$m, the resulting gap size that matches $Z_0 \approx 50\,\Omega$ impedance is, $s = 5.5\,\mu$m. This is a good compromise between the need for tight confinement and the space for the CPT.

To have the chip connected to the external circuitry via multiple wirebonds, the center conductors on the input/output side of the coupling capacitors need to be extended to a width of at least 100 μm. Here lies another advantage of the CPW geometry: as the characteristic impedance Z_0 is almost unchanged over a wide range of transverse dimensions, given the fixed ratio k, a smooth linear tapering from $a = 10\,\mu$m and $s = 5.5\,\mu$m, to $a = 150\,\mu$m and $s = 90\,\mu$m would simply serve our needs, without causing transmission reflection due to impedance mismatch. However, you as an astute reader, may have found a catch here. The dimensions $a = 150\,\mu$m and $s = 90\,\mu$m violates the previous rule that a, $b \ll h$. This inconsistency is resolved by the fact that the chip would in fact be mounted upon a thick printed circuit board (PCB) with a high relative dielectric constant $\varepsilon_{PCB} = 10.2$, making the Si substrate and PCB effectively a double-layer substrate with a relative dielectric constant $\varepsilon_{2L} \approx (\varepsilon_r + \varepsilon_{PCB})/2 \approx 11$ and a thickness $h_{2L} > 600\,\mu$m. The CPW model is therefore, still a valid approximation and the impedance Z_0 over the taper would remain close to 50 Ω.

Quality Factor & Coupling Capacitors

The loaded quality factor Q_L is a parallel combination of internal and external Qs as in Eq.(2.16). Since the internal Q_{int} depends the intrinsic losses of the resonator [see Subsection 2.2.3], once the CPW is fabricated on the selected substrate, and proper magnetic shielding is applied, Q_{int} will stay relatively fixed at a given temperature. In contrast, the external Q_{ext}, is determined by the strength of the coupling capacitor, according to Eq.(2.17), which gives the designer great freedom to engineer the desired loaded Q.

Two common patterns of the on-chip capacitor design are gap capacitors and interdigitated finger capacitors. The size of the gap capacitance [illustrated in Fig. 2.3] depends on the width of the gap, i.e. separation of the center conductors. Not-too-narrow gap capacitors usually put the resonator in the undercoupled regime, where $Q_{\text{ext}} \gg Q_{\text{int}}$ and $Q_L \approx Q_{\text{int}}$. In practice, this regime provides us a simple way to measure the intrinsic Q_{int} of the CPW, as we did for characterizing the intrinsic Q for Nb film at 4.2 K in Section 3.3.

The geometry of a finger capacitor is slightly more complex than that of a gap capacitor. It is composed of a number of pairs of 'fingers' of length l_f, width w_f and separation s_f, as shown in Fig. 5.2. To make things simple and at the same time help create a robust photolithography process, both the finger width and separation are set to $w_f = s_f = 3\,\mu$m, well above the minimum feature size that a standard mask aligner and

stepper/scanner are able to produce. The length of the fingers are set to $l_f = 20\,\mu$m, for reasons that soon will be clear in section 5.2.

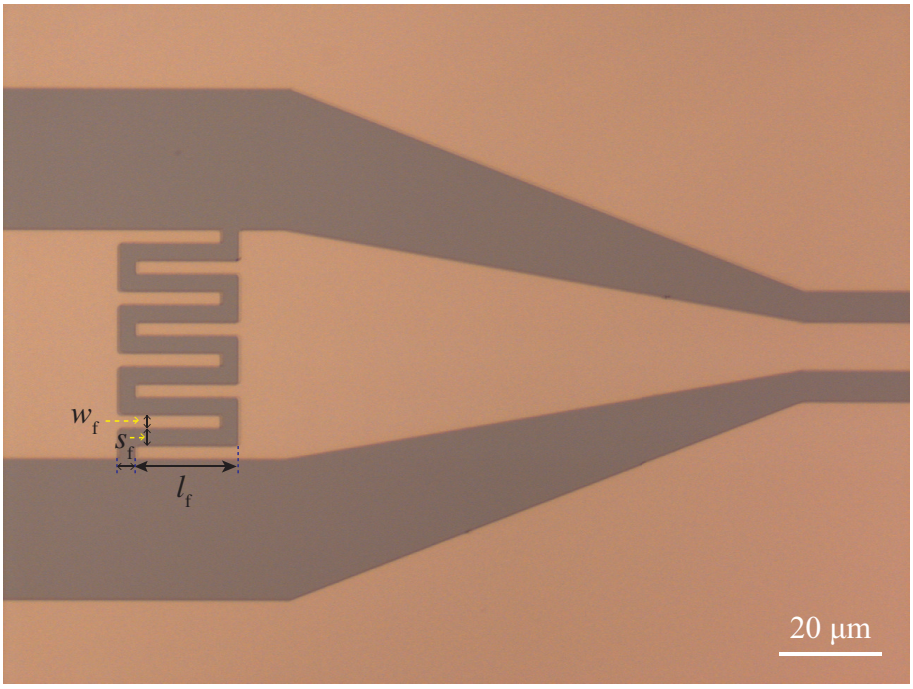

FIGURE 5.2: Optical micrograph of an 8-finger coupling capacitor, showing parameters characterizing the geometry of the inductor.

The devices discussed hereafter are all fabricated in Nb film, operating at dilution fridge base temperature $T \approx 30$ mK. Under these conditions, we fabricate and measure a CPW resonator with symmetric 1+1 finger (2-finger) capacitors, getting a loaded $Q_L \approx 1.5 \cdot 10^5$. Given the simulated external $Q_{\text{ext}} = Q_{2f}/2 = 2.35 \cdot 10^5$ [see Table 5.1], the resonator turns out to be in the overcoupled regime, not too far from the critical coupling point (Q_{ext} and Q_{int} are comparable). Still, the internal Q_{int} can also be estimated by Eq.(2.16): $Q_{\text{int}} = 1/(Q_L^{-1} - Q_{\text{ext}}^{-1}) \approx 4.15 \cdot 10^5$, which is within the expected range of the Qs of our Nb film.

The values of dc capacitance are conveniently simulated by *Maxwell*, a commercial EM field simulation package [72]. The simulated results, as well as the 'one-sided' external Q of the resonator with corresponding capacitor operating at 5 GHz, are shown in Table 5.1. An 'one-sided' resonator has one coupling capacitor as given, and the other with infinitesimally small coupling, thus can be treated as if it is 'one-sided'. The 'one-sided' external Q of the resonator, which gives an idea of the external Q tuned by just the given capacitor, is determined by $Q_{1S} \approx C/\omega_0 R_L C_\kappa^2$. A short cut for estimating the effective capacitance of a full-wave resonator is $C = \pi/(\omega_0 Z_0) = 2.0$ pF at 5 GHz [Eq.(2.8)], which avoids the need of estimating ε_{eff}.

Coupling capacitors	C_κ (fF)	Q_{1S}
20 μm gap	0.23	$1.2 \cdot 10^7$
10 μm gap	0.42	$7.2 \cdot 10^6$
1+1 finger	1.65	$4.7 \cdot 10^5$
2+2 finger	4.47	$6.4 \cdot 10^4$
4+4 finger	11.14	$1.0 \cdot 10^4$
6+6 finger	18.49	$3.7 \cdot 10^3$

TABLE 5.1: Simulated values of dc capacitance and calculated 'one-sided' external Qsat 5 GHz. C_κ is the simulated coupling capacitance. Q_{1S} is the external Q tuned by the given capacitor only, as if the cavity is one-sided.

In principle, the capacitance should have been simulated at microwave frequencies as well. Nevertheless, by the time the final design was set in October 2010, we did not yet have access to any simulation software capable of doing this, e.g. *Sonnet* [73]. As will be shown, the dc values of capacitance turn out to be accurate enough for our practical purposes. For future reference, one should always start and make adjustments with

dc simulations, which run orders of magnitude faster than full microwave simulations. Microwave simulations can then be followed to double-check and fine-tune the dc values.

As in Chapters 2 and 3, we first assume symmetric capacitive coupling to the input and output of the CPW resonator. The decay rate from each capacitor, also known as the angular frequency linewidth due to the loaded capacitor, is defined as $\kappa_{\text{in}} = \omega_0 Q_{C_{\text{in}}}^{-1}$. In the case of symmetric coupling $C_{\text{in}} = C_{\text{out}}$, we have $\kappa_{\text{in}} = \kappa_{\text{out}}$, which means 50% of the escaping photons leak out from each side of the resonator. This is rather inefficient from an experimentalist's point of view, in that only half of the outgoing photons are collected from the output capacitor by the amplifiers in the subsequent stages, and the other half simply 'die without a purpose'. To make the lives of most escaping photons more meaningful in the cCPT experiments, asymmetric coupling are adopted such that $\kappa_{\text{in}} \ll \kappa_{\text{out}}$. Specifically, the 1+1 finger (2-finger) capacitor is always selected as the input capacitor and the output capacitor can be either a 4+4 finger (8-finger) or 6+6 finger (12-finger) capacitor, depending on the requirement of the loaded Q. Having an 8- or 12-finger capacitor at the output end, simple calculations indicate that only about 2% or 0.8% of the outgoing photons, respectively, would escape via the input channel.

This is the end of the story for engineering of the Q, if we only consider the conventional transmissional CPW architecture. Adding dc feed lines terminated by inductors, however, surely complicates things quite a bit, for it introduces an extra channel for photon loss.

Section 3.5 shows that for a symmetrically overcoupled resonator with 5.85 nH spiral

inductors terminating the dc bias lines at 4.2K, the isolation of the dc bias lines at the resonant frequency, viz. the difference between the peak value of the main line transmission S_{21} and those of bias line transmission S_{31} and S_{41} at f_0, is about 13 dB (ideally, $S_{31} = S_{41}$ as a result of symmetry), indicating that less than 2.5% of the input power escapes through the dc bias lines.

While it is possible to develop a theory that takes into account the external loss due to the dc bias lines, i.e. $Q_{\rm dc}$, from a practical point of view, it is more convenient and accurate to take advantage of the EM simulation software Microwave Office for this dc-biasing scheme, as its results agree very well with the experiment in Chapter 2. Further simulations demonstrate that, for CPW resonators with asymmetric coupling described above and dc feed lines terminated by 5.85 nH inductors operating at temperature 20 mK, the isolation of the dc lines remains about 13 dB, even though the absolute magnitudes of all transmissions S_{i1} are lower due to the smaller coupling on the input side, and S_{41} gets pulled down much more than S_{31} owing to its asymmetry.

As the microwave leakage through the dc ports has been significantly suppressed by the bias inductor, we simply take the Q determined by intrinsic and coupling Qs [Eq.(2.16)] as a rough approximation of the loaded Q_L for the corresponding dc-biased CPW cavity, which turn out to be a fairly good estimate. For instance, the device that will be shown in the next chapter has parameters as follows: $C_{\rm in} = C_{2f} = 1.65$ fF, $C_{\rm out} = C_{12f} = 18.5$ fF, with identical bias inductors $L_b \approx 6$ nH. The loaded Q controlled by $Q_L \approx Q_{12f} = 3700$ is slightly higher than the measured value $Q_m \approx 3500$, as is expected. In comparison,

the simulated loaded Q of the whole dc-biased structure is $Q_L \approx 3600$, a narrowly better agreement with the measured value.

In summary, to estimate the loaded Q_L of a dc-biased CPW, a good rule of thumb is to just use the value given by Eq.(2.16) as if the bias lines are not there. Alternatively, a quick EM simulation of the full structure would also give at least an equally good estimate of the Q_L, if not any better.

Resonant Frequency

The cavity resonant frequency, an ostensibly straightforward parameter, is in fact the hardest to predict with a high accuracy by theory but essential to pin down in any cavity experiment. As in Subsection 2.2.1, the the resonant frequency f_0 of a full-wave CPW resonator ($l = \lambda$) is simply given by

$$f_0 = \frac{c}{\lambda\sqrt{\varepsilon_{\text{eff}}}} = \frac{c}{l\sqrt{\varepsilon_{\text{eff}}}}. \tag{5.1}$$

The effective relative dielectric constant ε_{eff} can be calculated by Eq.(2.21), or more easily by simulation softwares *AppCAD* or *TX-Line*.

Before explaining why the analytical calculation have difficulty producing an accurate resonant frequency, it is worth mentioning a couple of tricky points. First, although our substrate is made of bare silicon without intentional thermal oxidization, the natural oxidized oxide still makes the substrate itself effectively a double layer system, which

makes obtaining an exact value using either analytical formula or simulations very difficult. In fact, SiO_2 has an effective dielectric constant $\varepsilon_{r2} = 3.78$, which is in between the dielectric constants of vacuum ($\varepsilon_{r0} = 1$ by definition) and Si ($\varepsilon_{r1} = 11.9$). So one way to get a simple-minded but sometimes surprisingly good approximation for ε_{eff}, is just a simple average of the dielectric constants of vacuum and the Si substrate, namely, $\varepsilon_{\text{eff}} \approx (\varepsilon_r + 1)/2$.

More importantly, we need to be very careful when measuring the electrical length of the resonator, especially at its ends. For gap capacitors, since the EM fields decrease rapidly in the air, the physical starting/ending point of the gap capacitor can be treated naturally as that of the whole resonator. For finger capacitors, since the opposing fingers on both side of the capacitor extend deeply into each other, one would probably guess that half of the finger length l_f needs to be added to the physical length of the bare resonator. Experimental data [37] show that good fits to the resonance frequency can be obtained if approximately 40% of the finger length $l_f = 100\,\mu$m is taken into account, regardless of the number of fingers. While using this rule of thumb in our calculation, to achieve a better absolute uncertainty, we decided to use a shorter finger length $l_f = 20\,\mu$m in our design, instead of $100\,\mu$m.

Besides the extra electrical length added by the finger capacitors, a number of other factors come into play. For a conventional CPW resonator with the sole main line, we have shown the resonant frequency shifts due to the coupling capacitors in Section 2.1.3 and kinetic inductance in Section 2.2.2. The downward pulling by the loading of capacitors are well quantified by Eq. (2.15) and can be further approximated by $-\omega_0 C_\kappa / C$

for symmetric coupling. In contrast, the downward shift due to kinetic inductance is difficult to estimate, but its effects in frequency shift is estimated to be less than 5% for our geometry [See Section 2.2.2].

Again, adding the dc-biased lines with the terminating inductor L_b, plays a role in the resonant frequency of the main line. Another simplified lumped element model accounting the bias feed lines has been derived [74], expressing the new effective capacitance C and inductance L seen by the CPT as

$$C = \frac{C_l \lambda}{2}(1 - \frac{C_\kappa}{L_b} Z_0^2) \tag{5.2}$$

$$L = \frac{L_l \lambda}{2\pi^2}(1 + \frac{2}{\pi} Z_0 \omega_0 C_\kappa). \tag{5.3}$$

Hence, the shifted resonant frequency due to the loading of bias lines together with the capacitors is well approximated by

$$\omega' \approx \omega_0 (1 + \frac{C_\kappa}{2L_b} Z_0^2)(1 - \frac{1}{\pi} Z_0 \omega_0 C_\kappa). \tag{5.4}$$

Using our device parameters: $C_\kappa \approx C_{\text{out}} = 18.5$ fF and $L_b \approx 6$ nH, the upward shift due to the inductor L_b is about 0.8%. Even this is an overestimate, since the above equations are derived for symmetric coupling capacitors. For asymmetric couplings with $C_{\text{in}} \ll C_{\text{out}}$, the effect of the input capacitor is negligible and the total shift should only be $\sim 0.4\%$. The shift due to the loading of the bias lines can therefore be safely neglected. Amazingly, what this approximation gives us the same as that obtained for

a bare CPW main line pulled by the coupling capacitors, i.e. $\omega' \approx \omega_0(1 - C_\kappa/C)$, as it should!

Finally, the embedded CPT *per se* would cause a shift in the resonant frequency as well, since the CPT acts like an inductor in the supercurrent regime. The parallel connection of the CPT inductance L_{CPT} and the CPW effective inductance L implies that the modified effective inductance L' obeys

$$\frac{1}{L'} = \frac{1}{L} + \frac{1}{L_{\mathrm{CPT}}}. \tag{5.5}$$

Thus the shifted resonance is then

$$\omega = \omega_0 \sqrt{1 + \frac{L}{L_{\mathrm{CPT}}}}. \tag{5.6}$$

Since the the CPT inductance L_{CPT} can vary from 20–100 nH depending on the gate bias voltage [60], and $L = Z_0/(\omega_0\pi) \approx 0.5$ nH for a CPW cavity resonant at 5 GHz, the upward shift due to the CPT is expected to be between 0.12% to 1.24%.

In conclusion, if the electrical length is accurately estimated and the pulling of the loading capacitors is properly calculated, the downward uncertainty of the estimated resonant frequency should be within 5% mainly because of a joint effect of the kinetic and CPT inductances. Indeed, the two batches of Nb CPWs fabricated in series end up having a resonant frequency 4.0% and 2.67% below the designed values of 5.0 GHz and 5.4 GHz, respectively, consistent with our expectation.

Spiral Inductor

You may have been wondering about how we know the inductance of the spiral inductors all along. This is actually not a trivial question, to which tremendous effort has been devoted, because of its importance in silicon-based integrated circuits for radio-frequency applications [75–77].

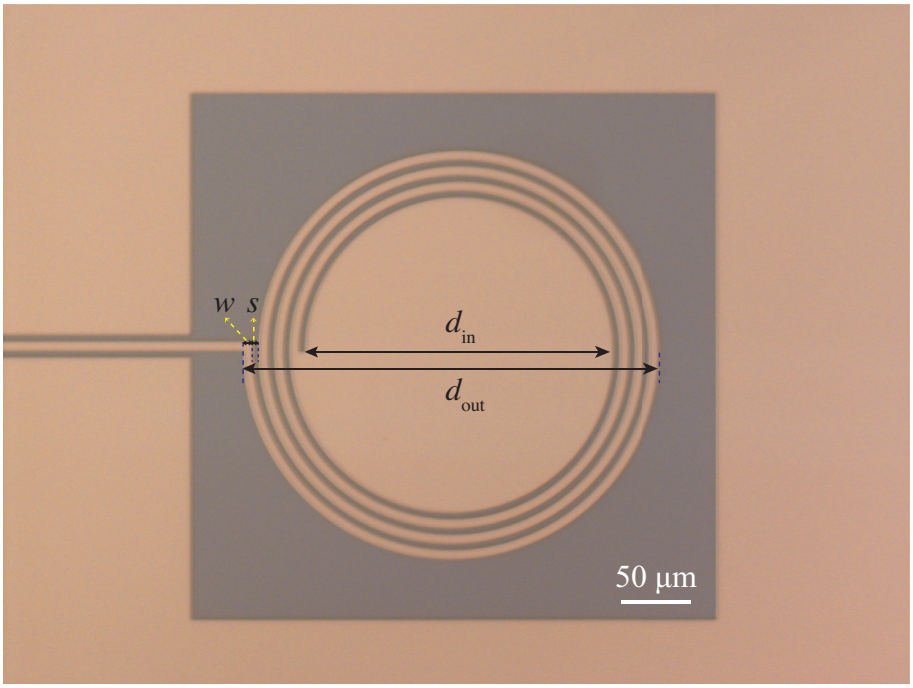

FIGURE 5.3: Optical micrograph of a 3-turn spiral inductor coupled to the CPW bias line, showing parameters characterizing the geometry of the inductor.

A simple and accurate expression for estimating the planar spiral inductance at room temperature is known as the current sheet model, which approximates the sides of the spirals by symmetrical current sheets of equivalent densities [77]. This simple model is capable of calculating inductances for different spiral geometries, such as square, hexagonal, octagonal and circular spirals. While the first three kinds of spiral inductors

are easier to lay out than the last one, we pick the circular spiral geometry, because it is the only one free of the sharp bend discontinuities and coupling of the corners, making the simple approximation more appropriate and parasitic modes less likely to appear. As shown in Fig. 5.3, a circular spiral inductor is completely specified by the number of turns n, the turn width w, the turn spacing s, and the inner diameter d_{in} or outer diameter d_{out}. The last two parameters are related by $d_{\text{out}} = d_{\text{in}} + 2n \cdot w + (2n-1) \cdot s$.

The expression for the spiral inductance given by the current sheet model is

$$L = \frac{\mu_0 n^2 d_{avg} c_1}{2} (\ln(c_2/\rho) + c_3\rho + c_4\rho^2) \tag{5.7}$$

where the average diameter $d_{avg} = (d_{\text{in}} + d_{\text{out}})/2$, and the fill ratio is defined as $\rho = (d_{\text{out}} - d_{\text{in}})/(d_{\text{in}} + d_{\text{out}})$. The coefficients c_i for the circular spirals are as follows: $c_1 = 1.00$, $c_2 = 2.46$, $c_3 = 0.00$, $c_4 = 0.20$. The accuracy of Eq.(5.7) worsens as the ratio s/w becomes large; for $s \leq 3w$, it exhibits a maximum error of 8% for room temperature spiral inductors. The results given by the current sheet model are also in excellent agreement with two other models, i.e. the modified Wheeler and monomial fit expressions [77]. A online calculator comparing all three models for square, hexagonal, octagonal spiral inductors is available from Stanford Microwave Integrated Circuits Laboratory [78].

For our circular inductors, we naturally keep the spiral turn width identical with the center conductor width of the CPW, i.e $w = a = 10\,\mu$m, keeping the CPW-to-microstrip transition smooth. To have a small s/w ratio and at the same time not to push the minimum feature size of photolithography, the turn spacing is set at $s = 5\,\mu$m. Meanwhile,

to make multiple wirebonds on the inner pad of the inductor, the inner diameter is fixed at $d_{\text{in}} = 300\,\mu\text{m}$. Given the above parameters, the values of spiral inductance for turns of $n = 1$ to 4 by the current sheet model (5.7) are shown in Table 5.2.

number of turns n	outer diameter d_{out} (μm)	Spiral inductance L (nH)
1	320	0.84
2	350	2.83
3	380	5.85
4	410	9.88

TABLE 5.2: Circular spiral inductance for turns of $n = 1$ to 4, $w = 10\,\mu\text{m}$, $s = 5\,\mu\text{m}$ and $d_{\text{in}} = 300\,\mu\text{m}$ by Eq.(5.7)

Note that for superconducting inductors, kinetic inductance again needs to be taken into account. Since a spiral inductor is essentially a microstrip with large diameters changing at each turn, similar to a CPW, the kinetic inductance of a microstrip is only a few percent of its linear inductance (~ 0.1 nH for 4-turn inductors with $d_{\text{avg}} = 400\,\mu\text{m}$), thus negligible compared to the spiral inductance.

Since an inductance value of 5 – 10 nH is ideal for our experiments, both 3-turn and 4-turn inductor designs were selected and incorporated into our dc biasing scheme.

Chip Dimensions

In order to suppress the parasitic modes of the cavity chip and the sample box, the chip must be made as small as possible, so that the minimum cut-off frequency of such modes will be raised further away from the resonant frequency of the CPW. This poses a

fairly difficult design issue in that with the addition of two half-wave dc lines with spiral inductors to the full-wave line, our structure is intrinsically significantly larger than the most commonly used half-wave resonators at around 5 GHz.

For the latest design, the effective dielectric constant is estimated to be $\varepsilon_{\text{eff}} \approx 6.78$ from the previous measured resonance. This gives a full-wave length of $l = \lambda \approx 21.30$ mm at the designed resonant frequency of 5.4 GHz (the resonance turns out to be at 5.256 GHz). To fit the dc-biased structure on a 10.5 mm by 5.5 mm chip, the center conductor and the gaps of the CPW have to meander. If the effective radius r of the meandering line is much greater than the gap size s, the impedance of the CPW will stay unchanged [21]. In our case, all effective radii are set to be $r = 155\,\mu$m in comparison with gap $s = 5.5\,\mu$m and the separation of the ground planes $b = 21\,\mu$m.

Special attention is also paid to make sure each of the dc feed lines and the main line are kept away from one another as distant as possible, thus suppressing the crosstalk between different channels to a large extent. To prevent other on-chip parasitic modes, e.g. slotline modes, jumpers are wirebonded to connect two halves of the ground plane periodically [38]. Wirebonds are also heavily implemented as effective air bridges wherever CPW discontinuities are encountered and various parasitic modes most likely to appear, such as T junctions, 180° bends, CPW tapering and CPW-to-microstrip transitions, as have been done in Fig. 5.4(b).

5.3 Printed Circuit Board & Sample Box

In order to perform electrical and microwave measurements on the CPW cavity, the sample chip has to somehow be connected to external circuitry. The mounting and packaging of the sample is extremely important for our ultra-sensitive ultra-low power system: there are only tens of photons in the cavity on average ($\sim$ 100 at most), outputting a few fW power. The goals of our sample packaging are therefore: 1, fully transmitting the signal from the cavity without impedance mismatch; 2, suppressing parasitic modes to a great extent; and 3, screening irrelevant EM fields from the ambient environment.

The last requirement can be easily satisfied by spatially confining the sample in a small volume by a metallic shield, i.e. a sample box, whose walls should be thicker than the skin depth of microwave frequencies on the order of a few GHz. To meet the first two goals, careful design and engineering have to be carried out. A standard approach [21, 69] is to mount the sample chip on a printed circuit board (PCB) within the box shielding, as in Fig. 5.4.

PCB

Let us start from the PCB, to which the sample chip is directly attached. To best match to the impedance of the on-chip CPW, it is natural to choose the same CPW geometry for the board, which also makes the board design process quite similar to that of the chip.

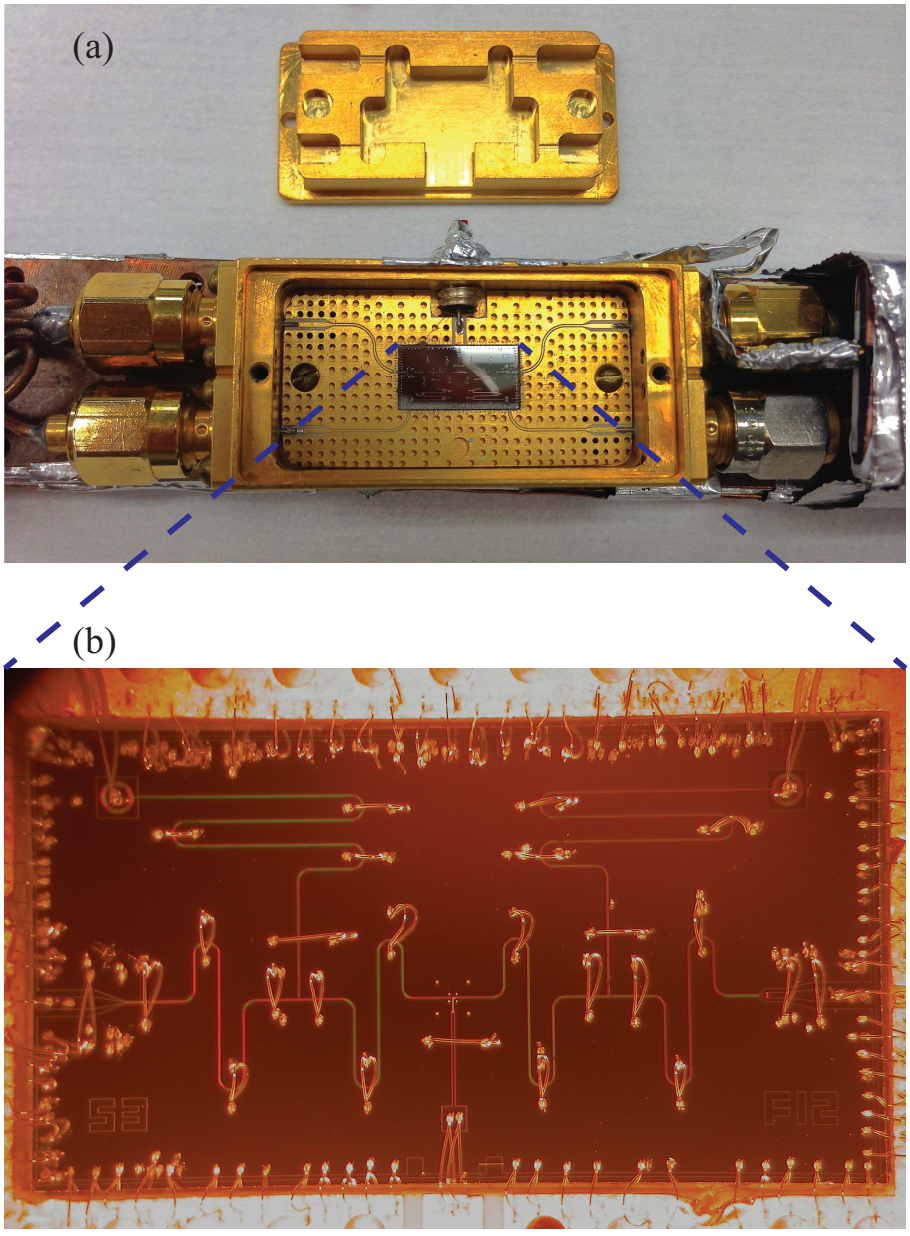

FIGURE 5.4: (a) Sample box mounted on the fridge 'tail' with a chip in it and the 'mode filling lid' of the box. (b) Optical micrograph of a dc-biased CPW chip mounted on the PCB with wirebonds connecting the transmission lines and ground planes.

Once again, we at first need to choose the 'substrate' of the PCB, viz. the material it is made of. A low-loss woven glass reinforced laminate, *Arlon* AD1000, is selected mainly because of its high dielectric constant $\epsilon_r = 10.2$. The board has a thickness of 25 mil, 1/2 oz double-sided copper cladding. A gold plating (thickness 0.05 mil) has been applied to both sides of the board for reliable wire-bonding and protection against tarnishing. Note that there is no standard nickel plating between the copper and gold layers, since we do not want any magnetic material in the proximity of the superconductor [69].

The board CPW center conductor width of $a = 5$ mil and gap width $s = 3$ mil is optimized again by *AppCAD* to achieve both a 50Ω characteristic impedance and roughly match the corresponding dimensions of the on-chip CPW on the border, rendering possible multiple short side-by-side wirebonds connecting their center conductors. When the traces are close to the edge of the board, just like the on-chip CPW, the board center conductor and gap widths are linearly extended to another set of 50 Ω-impedance dimensions, i.e. $a = 16$ mil, $s = 12$ mil, which are large enough for the SMA connector center pins (10 mil in diameter) to be soldered on. Another reason for introducing the dc biases to both the dc feed lines and the gate line via the CPW central traces is, in this way we can collect the microwave transmission leaking through the spirals (S_{21} and S_{31} in Fig. 3.1).

To suppress the parasitic modes caused by different 'grounds', it is best to make sure the system has only a single well-defined ground, i.e. all the grounds of the whole measurement setup, including the chip, the board, the box, the dilution refrigerator tail, etc., must all have good and frequent contact with one another. For the board *per se*,

different parts of the ground plane on the top side are periodically connected to the back, via a large number of plated through via holes (20 mil in diameter, spacing 40 mil or so). Furthermore, the bottom copper cladding of the board, kept as a single piece, is held firmly against the sample box by two top screws.

Similarly, we would like to make periodic wirebonding connections between the chip and the board, as many and short as possible. This is important for a well-established ground, but even more important for the wirebonds bonding their center conductors as well as the gate bias line, because the inductance of the Al wirebonds increases with its length at about 1 nH/mm [21]. We want to keep the total inductance between the grounds or the conductors as small as possible, so that the possibility of producing parasitic modes is minimized. To achieve this, a rectangular cut-out at the center of the circuit board is milled out to be 0.426" by 0.23" in size and 15-mil deep, thus making the chip fit snugly into the cutout and flush with the board traces. The two halves of the chip ground are also connected via wirebond jumpers periodically, especially near the various discontinuities [see Fig. 5.4(b)].

Sample Box

The sample box is made of OFHC copper, subsequently gold plated without an intermediate Ni layer for protection against tarnishing as for the board. To screen the EM fields from the environment, the box walls need to be much thicker than the skin depth of copper at relevant frequencies of 4 – 10 GHz, which is estimated to be around 1 μm. Thus practically any rigid copper box should work for this purpose. In our case, the

dimensions of the SMA connectors and a dc feedthrough post predetermine the thickness of the facing walls to be 125 mil and 60 mil, respectively.

This leads to the tricky part of the sample box design, viz. each of the microwave/dc center pins well soldered to the board actually acts like an antenna, which radiates/receives microwave signals to and from the free space inside the box, causing serious disturbances to our delicate transmission measurement. In fact, the first version of our box had a plain box lid, which made the interior of sealed box well approximated by a rectangular waveguide [35]. Using the box dimensions, simple calculations show that the lowest cutoff frequency of the TE/TM modes that can propagate within the box is right around our cavity resonance $\sim$ 5 GHz, which is unacceptable for our measurements.

To overcome this issue, we borrow an ingenious idea, namely, the so-called 'mode filling lid' from Ref. [69], which developed this idea after three iterations of their box designs. The essence of the 'mode filling lid' is to fill the inner space of the box with metal as much as possible, so that the cutoff frequencies of the surviving TE/TM modes are substantially lifted.

Accordingly, we fabricate the first version of the 'mode filling lid' for our PCB and chip layouts, shown in Fig. 5.5(a). The lid should be pressed tightly against the board, making the channels of the lid the only path the microwave can travel. Again, considering all possible cross-sections inside the box and plugging the dimensions into rectangular waveguide formulas, the lowest cutoff frequency of the TE/TM modes turns out to be 12.5 GHz, which is a great improvement over the plain lid and should not affect our

microwave detecting range of 4.0 – 6.0 GHz. However, we found from our measurements at 4 K that the crosstalk between the input microwave port and dc bias ports are still large compared with our simulation results.

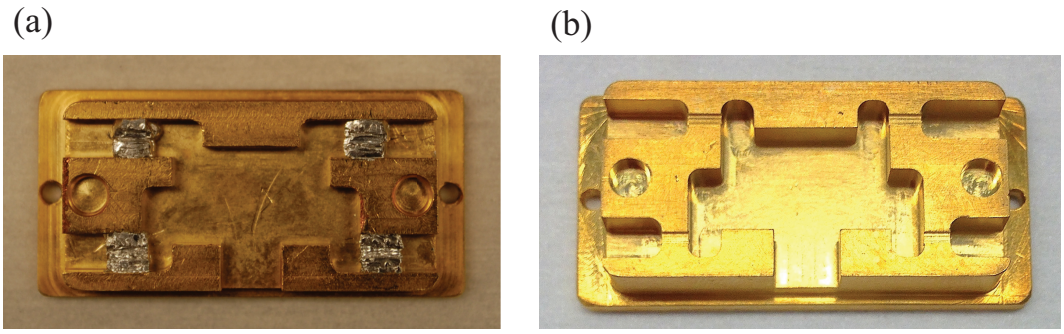

FIGURE 5.5: Comparison of the first (a) and second (b) versions of the 'mode filling lid' for the sample box. Note that in the first (a) lid, indium barriers were improvised to cut crosstalk between different ports and yet its microwave performance is still not as good as the (b) lid.

To block the unwanted crosstalk, a second version of the lid was then made with even narrower and shallower channels, as soon as the corresponding traces on the board are tapered down, as in Fig. 5.5(b). In this manner, the various dc/microwave ports are further isolated from one another. The good agreements in transmission measurements and simulations shown in Fig. 3.4 was not achieved until we used the new box lid.

With the close presence of the lid to the PCB traces, one might worry that the properties of the board CPW, especially its characteristic impedance could be changed, as it has effectively becomes a well-shielded CPW rather than a bare CPW in the free space. Fortunately, for a shielded CPW with the bottom of the shield a distance of H away from the surface of CPW, and a ground plane extending a width of $L/2$ from the middle of the center conductor to its sides, the impedance Z_0 is affected by less than 1.5% if $L/b \geq 1.75$ and $H/a \geq 2.50$ [38]. Consequently, the dimensions of our final lid design

are arranged to conform this criterion with a good margin, listed as follows: close to the edges of the board, the channel width is L = 125 mil and the channel height is H = 242 mil; when the traces narrows, L = 35 mil and H = 15 mil.

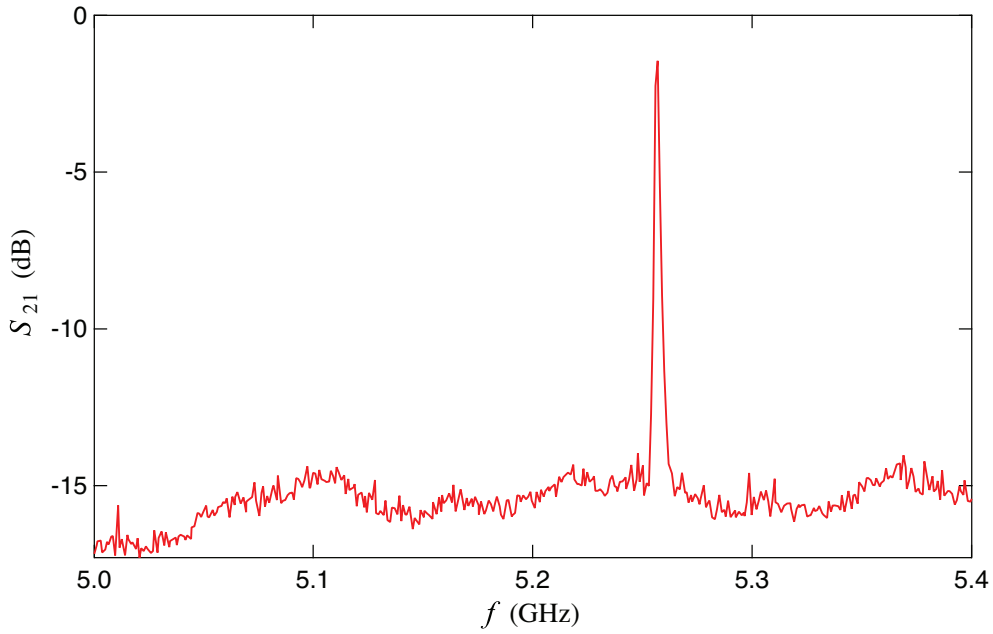

FIGURE 5.6: Measured transmission spectrum S_{21} of a cCPT in the final design of the sample box, showing nearly 15 dB suppression of parasitic modes around the resonance at $f_0 = 5.256$ GHz.

In the end, the final design of sample box and lid also works well for our cCPT experiments. The resulting main transmission S_{21} of the cavity is shown in Fig. 5.6, displaying nearly 15 dB suppression of parasitic modes 400 MHz around the resonance at $f_0 = 5.256$ GHz, with $Q \approx 3500$.

5.4 Fabrication

Once we have the design of the cavity, the fabrication of the cCPT is relatively straightforward. To fabricate a cCPT sample, its individual components, i.e. the dc-biased cavity and the CPT, need to be made separately by different techniques, mainly because their overall scale (∼10 cm vs. ∼5 micron) and minimum feature size (∼ 5 micron vs. ∼ 70 nm) are quite distinct as in Fig. 5.7.

The Nb cavity is fabricated by our collaborators, the Simmonds group at NIST Boulder, involving the following steps: 1, 100 nm Nb film is put down on the bare Si substrate by dc sputtering; 2, a standard photolithographic process transfers the design pattern from a photo mask to the photoresist on the surface of the substrate; 3, the exposed area of Nb film is then dry etched by a reactive ion etcher, thus defining the gaps of the CPW and and creating a sloping side wall.

Since the CPT and cavity are produced in separate steps, the cavity is exposed to the air in between and a robust Nb oxide layer is then formed. To ensure the coupling between the CPT source and drain leads to the center and the ground of the cavity, as well as the coupling between different parts of the gate line, some means of either removing the oxide or preventing its formation must be found. Our collaborators at NIST deposit thin Ti/Au contact pads after ion milling away the oxide on the Nb resonators, as shown in Fig. 5.7 (b). The Au of the pads does not oxidize during the subsequent exposure to air, and the total pad thickness of 30nm is sufficiently thin that it can be driven

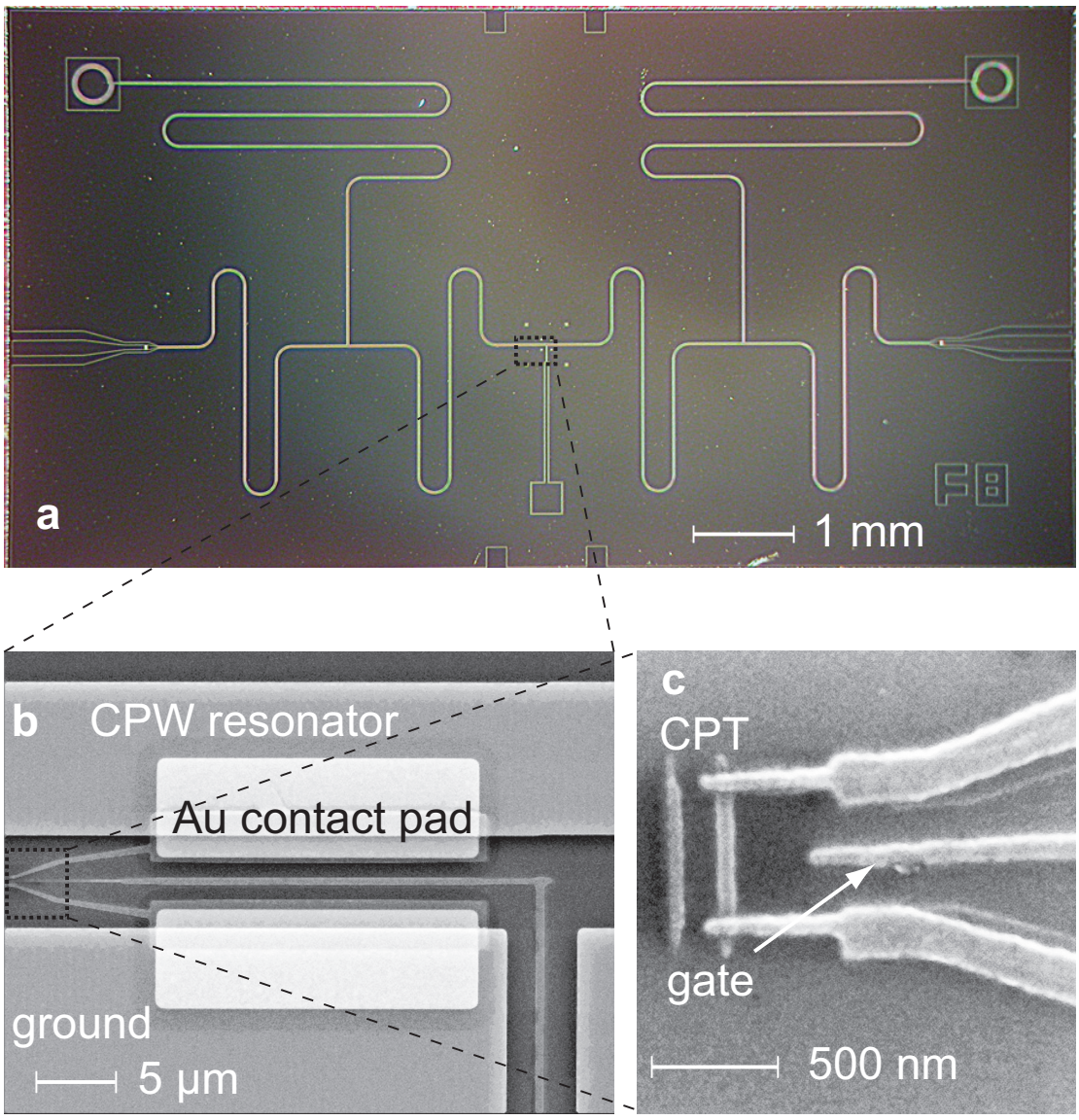

FIGURE 5.7: (a) Optical micrograph of a CPW resonator with dc feed lines terminated by inductors. (b) Electron micrograph of the center of the cavity showing the Ti/Au contact pads connecting the source and drain leads of the CPT, and the gate line entering the cavity gap from lower right. (c) Detailed view of the CPT, showing the source/drain leads, center island and the gate line.

superconducting via the proximity effect by the thicker metal of the Nb cavity below or the Al CPT leads above.

The CPT is reliably made in our lab by electron-beam lithography followed by double-angle shadow evaporation [79]. To prevent trapping of quasiparticles on the island and ensure $2e$ periodicity in the CPT supercurrent regime, we fabricate the CPT with an ultra-thin (thickness $\sim$ 7 nm) central island [see Fig. 5.7 (c)], which has a slightly larger superconducting band gap than the thicker leads [80]. To make sure such a thin Al film is electrically continuous, the substrate has to be cooled to a low temperature. A liquid nitrogen cooled sample stage in our thermal evaporator was developed by Dr. Zhongqing Ji [57]. The ultra-thin islands fabricated by this technique in our lab have shown to routinely prevent quasiparticle poisoning of the supercurrent in the past [81], as well as in the cCPT sample [Fig. 4.5 with $2e$ period].

To make sure the Au contact pad is driven superconducting especially in the CPW gap where there is no Nb layer underneath the Au, we want to deposit the Al leads layer as thick as possible. We are able to routinely achieve a thickness of $\sim$ 70 nm for this layer, which completely covers the Au pad within the gap and should drive it superconducting at the dilution fridge base temperature $\sim$ 30 mK. In addition, the large contact area ($20 \times 5\,\mu m^2$) of the lead and the Au pad ensure reliable direct coupling between the CPT and the cavity.

Chapter 6

Measurement & State Reconstruction Techniques

This chapter is divided into two parts. We first discuss the cryogenic, electrical, and microwave measurement techniques used in the cCPT experiments. We then introduce quantum state tomography and apply it to the cCPT emission fields. In particular, we extend maximum-likelihood methods for the microwave photon fields with relative large numbers of signal and noise photons, and reconstruct density matrices from the field quadrature measurements.

6.1 Measurement Setup

Given direct access to the dc source-drain and gate voltage lines, electrical transport in the cCPT can be probed by standard dc measurement circuits, very much the same way a bare CPT is measured. At the same time, the cavity state can be characterized by microwave transmission through the cavity output, similar to what we did in Chapter 3 for a dc-biased cavity without a CPT in it. We choose a standard transmission type setup for the cCPT experiments as opposed to reflection, because it is exactly what the dc biasing scheme with symmetric biasing lines and asymmetric coupling capacitors, is designed for.

6.1.1 Cryogenic Setup

The cCPT experiments are conducted in an *Oxford Instruments* Kelvinox 100 dilution refrigerator with a base temperature of $\sim 20 - 30$ mK. The sample is mounted on a home-made fridge 'tail', which is screwed on the cold stage inside the mixing chamber at the base temperature.

This Kelvinox 100 dilution fridge in our lab was historically set up to perform reflection measurements [57, 79]. Although it is not difficult to convert it to a transmission setup, great care must be taken to ensure proper noise filtering and heat sinking for both microwave lines and dc lines. Pictures of the fridge insert and its various components are shown in Fig. 6.1.

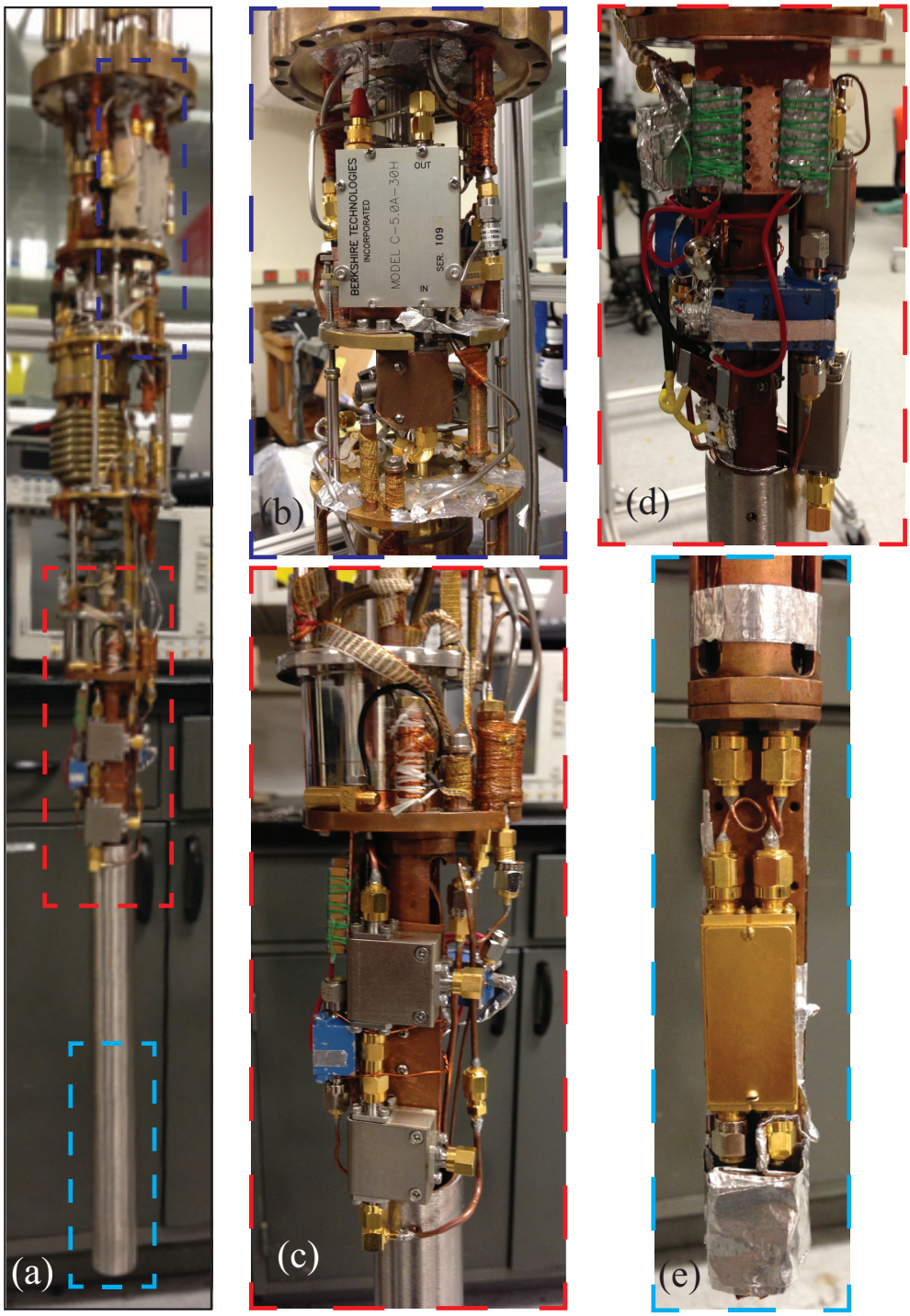

FIGURE 6.1: Kelvinox 100 dilution fridge insert (a) inside the inner vacuum chamber with a magnetic shield installed, with various enlarged components: (b) a HEMT amplifier with a circulator right underneath, (c) the still and two circulators inside the mixing chamber, (c) two ~ 40 μF capacitors and bias tees for both dc biasing lines, and (d) the sample box mounted on the tail seen with the magnetic shield removed.

As discussed in Section 4.5, the cCPT is expected to be driven by the dc bias in the regimes we are interested, for which no ac signal is applied. Even in the few circumstances where an external microwave signal is needed for characterizing the cavity, less than -70 dBm (100 pW) is required at the input end of the cavity. Thus a low thermally conductive and lossy stainless steel coaxial cable is perfect for the microwave input line from room temperature to the fridge tail. In addition, cold attenuators at various stages are used to further reduce the noise transmitted in the input cable. A total of $\sim$ 50 dB attenuation is achieved from room temperature to the cavity input.

The microwave output line, on the other hand, needs to have very low loss, especially before the cavity output signal reaches the first amplification stage, in this case, a high electron mobility transistor (HEMT) amplifier. On the fridge tail, low-loss copper cables are used for both input and output lines, which also provides high thermal conductivity to keep the sample in thermal equilibrium with the cold stage. Between the cold stage to the input of HEMT amplifier at 4.2 K, a 0.0085" Nb coax cable is installed, as Nb becomes superconducting below 9 K and has both nearly zero electrical loss and zero heat conductance.

The *Berkshire* 3-stage low-noise HEMT amplifier used here has three amplification stages supplying a total gain of $\sim$ 38 dB for frequencies between 4.0 – 6.0 GHz with a noise temperature of $T_n \approx 8$ K. In order to prevent the HEMT back acting the sample, three *Pamtech* circulators (4.0 – 8.0 GHz) are installed in series in between the cavity output port and the HEMT, two at the fridge tail and one right below the HEMT, each adding $\sim$ 20 dB isolation.

In addition to the microwave lines, a ribbon of 24 Manganin wires runs from room temperature to the tip of fridge tail. These dc wires are filtered by a 3 Hz RC low pass filter at room temperature and a Cu powder filter at the base temperature. In the cCPT experiments, we need only three dc lines: two for introducing and measuring the bias voltage and current, and one for supplying the gate voltage bias. For redundancy, each dc line is applied through two different wires on the ribbon.

From the ribbon wires to the sample the gate bias is introduced via the dc feedthrough going into the sample box. Each of the source-drain bias lines is connected via a bias tee whose ac port is terminated by a 50 Ω cap. The combined dc and ac output of the bias tees is then transmitted to the PCB traces via Cu coax cables and SMA connectors. A 100 Ω cold resistor is inserted into each source-drain bias line between the ribbon wires and the dc input port of the bias tee for CPT protection against electrostatic discharge.

As discussed in Section 2.2.3, trapping of magnetic flux in superconducting films may contribute to excess internal dissipation of the cavity. To alleviate this problem, a 0.062" thick Amumetal 4K (A4K) magnetic shield [82] was designed, fabricated, and ultimately bolted to the fridge tail, fully enclosing the sample box [See Fig. 6.1(a) & (e)]. A4K is a high permeability nickel alloy and this specific shield has been optimized for use at our base temperature 30 mK through hydrogen annealing cycles. Situated at more than five times the shield's inner diameter from the opening, the magnetic field at the sample box is estimated to be attenuated by a factor of $\sim 2000 - 3000$, thus eliminating concerns regarding stray magnetic fields.

6.1.2 Electrical & Microwave Measurement Scheme

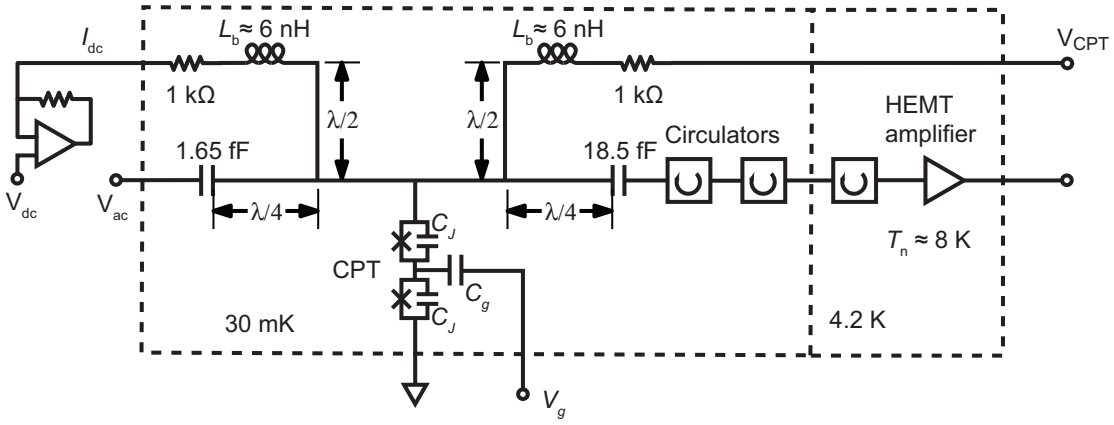

FIGURE 6.2: dc and microwave measurement scheme for the cCPT experiments.

The combined dc and ac measurement scheme for the cCPT experiments is illustrated in Fig. 6.2. In this scheme, both the source-drain bias voltage $V_{\rm dc}$ and the gate bias voltage V_g are first generated by a data acquisition (DAQ) board controlled by the *Labview* program on a computer. The current of the inductive bias line $I_{\rm dc}$ is measured by a current-to-voltage converter (i.e. current amplifier) before being fed into the cold bias line. Because the drain electrode of the CPT is always internally grounded, the current going through the CPT double junctions $I_{\rm CPT}$ is simply the same as the incoming current, i.e. $I_{\rm CPT} = I_{\rm dc}$.

Meanwhile, the other inductive bias line can be used for directly measuring the voltage across the CPT $V_{\rm CPT}$, as essentially no current will be flowing through this line due to the ultra-high input impedance of the voltage amplifier. By scanning the bias voltages $V_{\rm dc} = V_{\rm CPT}$ and V_g while monitoring the CPT current, an image plot of current $I_{\rm CPT}(V_{\rm dc}, V_g)$ revealing the dc properties of the cCPT, can be routinely obtained.

On the other hand, standard transmission measurements can be employed to characterize the basic microwave properties of the cavity, such as the resonant frequency and the loaded Q, ideally by a network analyzer. The network analyzer in our lab, however, only operates at frequency up to 3.5 GHz, too low for our cavity resonance. A Labview program was therefore written to simultaneously control a signal generator and a spectrum analyzer via their GPIB (General Purpose Interface Bus) interfaces, effectively implementing a network analyzer. A *Lucix* 2 – 6 GHz room temperature field-effect transistor (FET) amplifier is used to amplify the signal prior to measurement by the spectrum analyzer, providing another stage of gain of $\sim$ 45 dB at around 5 GHz.

6.1.3 Improved Microwave Measurement Scheme

The measurement setup in Fig. 6.2 worked well for our investigation of dc transport in the cCPT system. Nevertheless, it has serious limitations for sensitive microwave measurements.

Let us consider thermal noise in a simplified cCPT model, with only the protective resistor $R = 1\,\mathrm{k}\Omega$ and a single Josephson junction at the fridge base temperature $T = 30$ mK, as shown in Fig. 6.3(a). We emphasize here that the noise considered is the low frequency noise introduced by the dc feed lines, as opposed to the cavity resonance at $\sim$5 GHz, because the high frequency noise has been carefully filtered for both dc and microwave lines. For low frequencies close to dc, even at a low temperature $T = 30$ mK, voltage fluctuations resulting from the thermal noise of the resistor are still well

approximated by the Rayleigh-Jeans approximation, giving the white Johnson noise [35]:

$$V_n = \sqrt{4k_B T B R}. \tag{6.1}$$

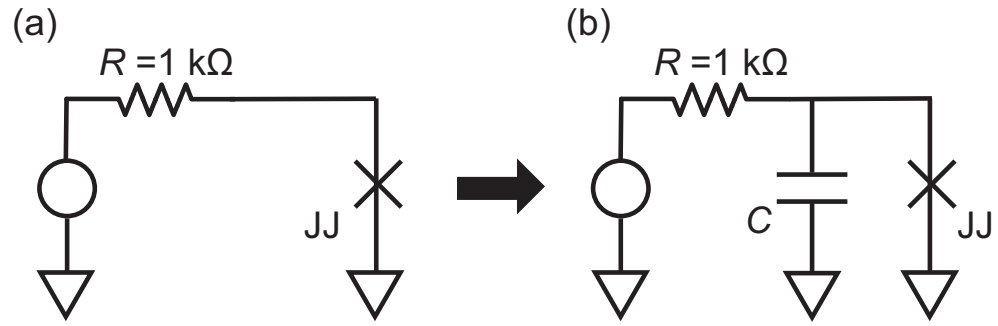

FIGURE 6.3: A simplified cCPT model to study the effect of the thermal noise, with-/without the capacitor.

Assuming low frequency noise with a moderate bandwidth $B = 1$ MHz enters the cavity via the dc lines, an apparently small thermal noise voltage $V_n \approx 40$ nV given by Eq. (6.1) is applied to the junction. However, the resulting jitter in the Josephson frequency

$$\delta f_d = \frac{2eV_n}{h} \approx 20\,\text{MHz} \tag{6.2}$$

being much larger than the cavity linewidth $B_c = f_0/Q \approx 1.5$ MHz, is clearly far too large. Hence, sharp features within the cavity linewidth, if any, would definitely be washed out by the thermal noise.

Fortunately, a large capacitor can be added to the circuit to form a RC filter, as shown in Fig. 6.3 (b). The RC low-pass filter with a cut-off frequency of $f_c = 1/(2\pi RC)$,

effectively reduces the integrated voltage noise to $V_n = \sqrt{k_B T/C}$, which no longer depends on the resistance R.

We installed two ceramic capacitors in parallel on each dc feed line [see Fig. 6.1(e)]. Each of them has a capacitance of 220 μF at room temperature and has been tested at 4 K, which indicates a cold capacitance of $\sim$20 μF. The parallel arrangement of the capacitors gives a large total cold capacitance of $C \approx 40\,\mu$F. Thanks to the large capacitors, the voltage jitter is reduced to $V_n \approx 0.1$ nV, corresponding to a drive frequency fluctuation of $\delta f_d \approx 50$ kHz.

With a such great improvement from the cold capacitors, one may worry that whether the thermal noise from room temperature would live up to this standard as well. At room temperature a capacitor can similarly be attached to form a RC circuit. To obtain the same noise level as the cold RC circuit, the room temperature capacitor would need to be $\sim$0.4 F, an extremely large capacitance! Even if such a large capacitor existed, it would make the measurement circuit respond too slowly in any case.

A feasible and elegant way to achieve our goal is to put in another resistor at the base temperature to serve as a cold voltage divider shown as $R_d = 100\,\Omega$ in Fig. 6.4. In this manner, even with a moderate capacitor $C = 2\,\mu$F at room temperature and a large biasing resistor $R_b = 100$ kΩ, the voltage noise after the cold divider is a thousand times smaller than that at room temperature and is $\sim$50 pV. Together with the cold capacitors, the new microwave measurement scheme does not only bring a much better resolution in microwave spectrum, but also makes possible quantum state tomography

using microwave field quadratures, as will be discussed in Section 6.2.

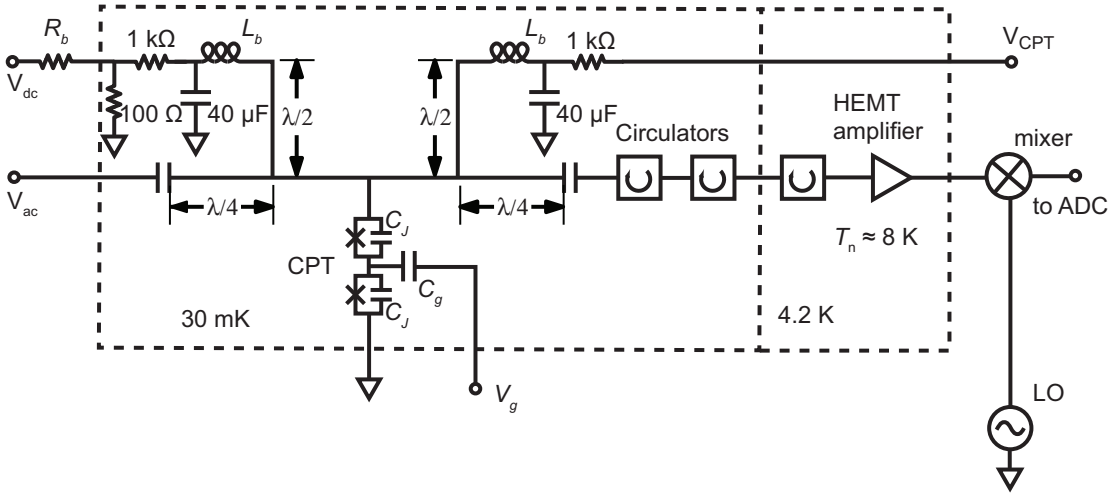

FIGURE 6.4: Improved microwave measurement scheme for the cCPT experiments.

Just as "there is no such thing as a free lunch", the much-improved microwave measurement scheme does not come without any expense. By adding the cold divider grounded in the mixing chamber, we have gave up our direct means of monitoring the CPT current. It is straightforward to figure out an indirect method to calculate the CPT current in the new biasing scheme:

$$I_{\mathrm{CPT}} = \frac{I_d R_d - V_{\mathrm{CPT}}}{R_{1\mathrm{k}}} \approx \frac{V_{\mathrm{dc}} R_d / R_b - V_{\mathrm{CPT}}}{R_{1\mathrm{k}}} \tag{6.3}$$

where $R_{1\mathrm{k}}$ is the 1 kΩ protective resistor, and the current flowing through the divider resistor I_d can be approximated by $I_d \approx V_{\mathrm{dc}}/R_b$. This is a good approximation only when the CPT differential resistance R_{CPT} is large. But since the $I-V$ slope varies significantly around the supercurrent regime, the accuracy of the approximation is not

be very consistent. For this reason, current sensitivity in this setup is not as good as in the original setup [see Fig. 6.4]. We therefore decided to take advantage of both schemes: the dc measurement results presented in Chapter 6 are measured by the previous scheme, while most of the microwave spectrum and all quadrature measurement data are taken using the new one.

6.1.4 Shot Noise Calibration of the Amplifier Chain

An important parameter of microwave measurement setup is the effective total gain G of the whole amplification chain from the sample cavity input to the room temperature FET amplifier output [see Fig. 6.4]. Taking into account the insertion loss of the cavity, the loss on three circulators, the loss on both cold and warm coax cables, the HEMT amplifier gain, and the FET amplifier, these values calibrated at room temperature add up to $G \approx 69$ dB. Since the performance of the microwave components is slightly different at the fridge base temperature, we need to calibrate G when the microwave line is cold. In this case, we do not have a direct access to the cavity except through the microwave input line, which adds another factor of uncertainty in and of itself.

Instead, a standard method to calibrate the cold amplification gain in the CPT experiments is to take advantage of the shot noise generated by the cCPT. At high source-drain bias, a bare CPT with two symmetric junctions has a shot noise current spectral density [49],

$$S_I = \frac{eV_{\mathrm{dc}}}{R_{\mathrm{CPT}}} = eI_{\mathrm{dc}} \tag{6.4}$$

where R_{CPT} is the normal resistance of the CPT when biased well above the superconducting gap. In the cCPT system, the measured CPT shot noise is modified by the presence of high-Q cavity. To derive the expression for cCPT output shot noise, we as usual model the CPW cavity as a parallel LCR circuit with a resonant frequency ω_0. We assume the cavity is driven by the shot noise current of the CPT with spectral density S_I as in Eq.(6.4). A lumped element model of a CPW resonator coupled to a dissipative CPT driven by a current noise source, is shown in Fig. 6.5.

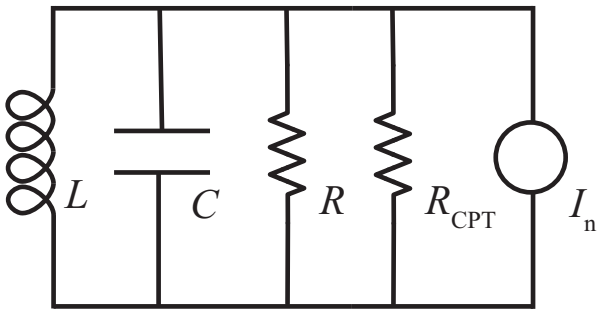

FIGURE 6.5: LCR lumped elements of a CPW resonator coupled to a dissipative CPT resistance, driven by a current noise source.

Applying Kirchoff's laws to the circuit, the voltage noise spectral density at the cavity output can be derived as

$$S_V(\omega) = \left(\frac{\omega}{C}\right)^2 \frac{eS_I}{\left(\omega_0^2 - \omega^2\right)^2 + (\omega\omega_0/Q_L)^2} \tag{6.5}$$

where Q_L is the loaded Q of the cavity taking into account the additional loading of dissipative CPT resistance. The loaded Q is thus given by $Q_L^{-1} = Q_C^{-1} + Q_{\mathrm{CPT}}^{-1}$, where

$Q_{\mathrm{CPT}} = \omega_0 R_{\mathrm{CPT}} C$ and Q_C is the original cavity "loaded Q" without additionally CPT dissipation.

The total voltage noise over the entire bandwidth of the resonance can is given by the integral

$$\langle V_n^2 \rangle = \frac{1}{2\pi} \int_\omega S_V \, d\omega = \frac{e I_{\mathrm{dc}} Q_L}{4\omega_0 C^2}. \tag{6.6}$$

The total stored energy, including both electric and magnetic energy, is

$$E = C\langle V_n^2 \rangle = \frac{e I_{\mathrm{dc}} Q_L}{4\omega_0 C}. \tag{6.7}$$

Finally, the noise power at the cavity output port is given by

$$P_c = \kappa_{\mathrm{out}} E \approx \kappa_{\mathrm{tot}} E = \frac{e I_{\mathrm{dc}}}{4C} \frac{Q_L}{Q_C} \tag{6.8}$$

where we have used the condition that $\kappa_{\mathrm{out}} \gg \kappa_{\mathrm{in}}$ and $\kappa_{\mathrm{tot}} \approx \kappa_{\mathrm{out}}$. The noise is then amplified by the amplifier chain with a effective gain G, giving the room temperature noise power:

$$P_n = G P_c = \frac{eG}{4C} \frac{Q_L}{Q_C} I_{\mathrm{dc}} \, . \tag{6.9}$$

By driving the CPT into the above-gap regime, while collecting the output noise power, we can plot P_n versus I_{dc} as Fig. 6.6.

We know that the cavity $Q_C \approx 3500$ and the cavity effective capacitance $C = \pi/\omega_0 Z_0 =$ 1.9 pF. The loaded Q_L can be obtained from curve-fitting the output spectrum at high

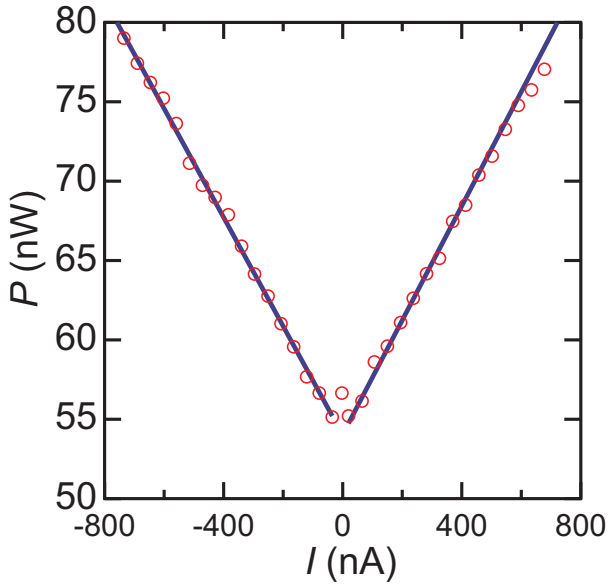

FIGURE 6.6: Noise power P_n (red dots) at the output of the amplifier chain versus CPT current $I_{\rm dc}$, linearly fitted by two lines (solid lines).

dc biases, giving an average $Q_L \approx 900$. Using these values and the average slope from a linear fit to P_n versus $I_{\rm dc}$, we determine the total $G = 68$ dB. This is in excellent agreement with room temperature calibration, with a deviation of only 1 dB.

In addition, the intersection B of the high-current linear asymptotes of P_n extrapolated back to $I_{\rm dc} = 0$ determines the system noise (dominated by the HEMT amplifier), i.e. $B = G\Delta f\, k_B T_{\rm sys}$, where Δf is the measurement bandwidth of the output noise. This gives a system noise $T_{\rm sys} = 31$ K, higher than the HEMT noise temperature $T_{\rm HEMT} = 8$ K specified by the manufacturer. Losses on the cable and three circulators between the cavity output and HEMT input are likely to give rise to the larger system noise temperature. Finally, the number of HEMT noise photons is calculated as $n_h = k_B T_{\rm HEMT}/\hbar\omega_0 \approx 123$. The number of added noise photons is important for quantum state tomography, the topic of the next section.

6.2 Quantum State Tomography

The quantum state of any physical system can be completely characterized by its density matrix or equivalently an quasi-probability distribution such as the Wigner function defined in Eq. (1.3). Nonetheless, given a prepared state of a quantum system, its very quantum nature makes it impossible for a person to determine the state without disturbing the system, just as in the Schrödinger's cat experiment in Fig. 1.1. One way to circumvent this problem is to prepare an ensemble of identical state, make a set of observations of the state, and build up a histogram of the outcomes. A probability distribution of the system can then be reconstructed through data analysis and the whole process of probing the state is called quantum state tomography (QST) [83].

As will seen in Chapter 7, our electrical and microwave measurement results let us strongly suggest that the cavity photon field of the cCPT system exhibits non-classical features of light. We therefore would like to apply QST, which has been widely used for optical fields of light [83], to the microwave emission of the cCPT.

Before we proceed, it is worth explaining what we mean by "quantum" or "non-classical" states. If you are convinced the quantum theory is more fundamental than its classical counterpart [as in Section 1.1], you may think that no state should be classical. Borrowing from George Orwell [84], we could well say that *all states are quantum, but some states are more quantum than others.*

To clarify the meaning of "quantum" or "non-classical", we will review some basics of quantum optics, phase-space probability distributions in particular. Subsection 6.2.1

follows the discussion in Gerry & Knight [5].

6.2.1 Phase-space probability distributions

Besides the Wigner function, two other probability distributions are widely used, namely the Glauber-Sudarshan P function and Husimi Q function. Any density matrix ρ can be represented as a linear combination of coherent states $|\alpha\rangle$ with the P function being the coefficient:

$$\rho = \int_{\alpha} d^2\alpha \, P(\alpha)|\alpha\rangle\langle\alpha| \tag{6.10}$$

where $\int_\alpha \equiv \int_{\mathbb{C}} \mathrm{d}\alpha$ is defined as the integral over the complex plane. As the P function can be negative or highly singular for some quantum states, it is a quasi-probability distribution like the Wigner function.

The Q function corresponding to density matrix ρ is also defined via coherent states $|\alpha\rangle$ as:

$$Q(\alpha) = \frac{1}{\pi}\langle\alpha\,|\rho|\,\alpha\rangle. \tag{6.11}$$

Since the Q function is positive for all states, it can be considered as a true probability distribution.

In addition, the Wigner function can also be related to the corresponding density matrix ρ by

$$W(x,p) = \frac{1}{h}\int_{-\infty}^{+\infty} \langle x + \frac{1}{2}x'\,|\rho|\,x - \frac{1}{2}x'\rangle e^{-ipx'/\hbar}dx'. \tag{6.12}$$

The Wigner function turns out to be very useful for distinguishing between quantum and classical states, because it is very sensitive to certain quantum features and it is always well-behaved. For example, we consider two representative quantum states of light, i.e. the most quantum state, the Fock (photon number) state; and the most classical of the quantum states, the coherent state. The Wigner function for a Fock state $|n\rangle$ is

$$W(\alpha) = \frac{2}{\pi}(-1)^n L_n(4|\alpha|^2)e^{-2|\alpha|^2} \tag{6.13}$$

where L_n is a Laguerre polynomial. For the coherent state $\rho = |\beta\rangle\langle\beta|$, the Wigner function is

$$W(\alpha) = \frac{2}{\pi}e^{-2|\alpha-\beta|^2}. \tag{6.14}$$

From the above formulas, it is clear that for a Fock state, the Wigner function is oscillatory and negative over a large region in phase space, whereas it is a totally positive Gaussian distribution for a coherent state. As a matter of fact, the negativity of a Wigner function is a signature of a quantum state; a state with a partially negative Wigner function is considered to be *quantum* or *non-classical*. The converse, however, is not always true.

We thus bring in another indicator of the nature light as well as the photo statistics, namely, the Fano factor. It is defined as

$$F = \frac{\langle n_{\rm ph}^2\rangle - \langle n_{\rm ph}\rangle^2}{\langle n_{\rm ph}\rangle} \tag{6.15}$$

where n_{ph} is the photon number of the system. It essentially measures the variance of photon number relative to the average photon number. Typical values of the Fano factor are: $F = 0$ for a Fock state, $F = 1$ for a coherent state and $F = \langle n_{\text{ph}} \rangle + 1$ for a thermal state. A state with $0 < F < 1$ is also *non-classical*, because it is an amplitude (number) squeezed state and exhibits sub-Poissonian photon statistics, even though its Wigner function could be completely positive.

6.2.2 Microwave Field Quadrature Measurement

Quantum state tomography was first realized in the optical frequencies for the full reconstruction of a single cavity state, using both homodyne and heterodyne detection schemes [83]. For microwave frequencies, we implement the heterodyne analog of the optical techniques, the microwave field quadrature detection scheme, for characterizing photons escaping the cCPT cavity.

Detection Scheme

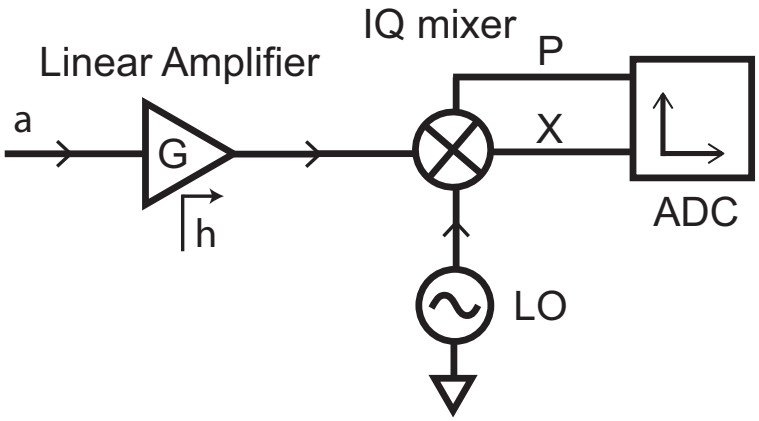

FIGURE 6.7: Simplified microwave field quadrature detection scheme.

A simplified microwave field quadrature detection scheme is illustrated in Fig. 6.7. The cavity in the cCPT can be considered as a radiation field with a photon mode a. The signal mode a is first amplified by a phase-insensitive linear amplification chain with an effective gain G. During this amplification process, a noise mode h is also introduced to the signal. Since $G \gg 1$, the system noise is dominated by the amplifier noise modified by the cable loss, i.e. $h \approx h_{\text{amp}}$. The amplified signal is then combined with a LO signal in a mixer and down-converted to conjugate quadratures $\hat{X}$ and $\hat{P}$. Thus the complex amplitude operator $\hat{A}$ can be defined [85, 86]

$$\hat{A} \equiv a + h^{\dagger} = \hat{X} + i\hat{P}. \tag{6.16}$$

The amplification factor $\sqrt{G}$ has been removed in this definition by referring $\hat{A}$ to the input of the amplifier. Assuming the signal a and noise h are not correlated with each other, the probability distribution of $\hat{A}$ can be expressed as the convolution [87]

$$D^{[\rho_a]}(A) = \int_{\alpha} P_h(A^* - \alpha^*)\, Q_a(\alpha) \tag{6.17}$$

where ρ_a denotes the density matrix of mode a, $P_h(\alpha)$ is the P function of noise mode h, and $Q_a(\alpha)$ is Q function of the signal mode a .

Detection Setup

In reality, the field quadrature detection experimental setup shown in Fig. 6.8 is a bit more complex than the scheme shown in Fig. 6.7. The amplification chain before the

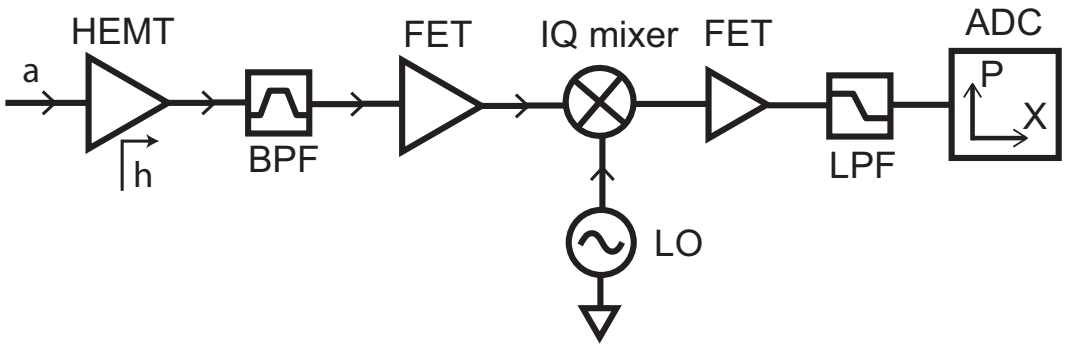

FIGURE 6.8: Microwave field quadrature detection setup.

IQ mixer consists of a cold HEMT amplifier with ∼38 dB gain and a room temperature FET amplifier with ∼45 dB gain around the cavity resonance at ∼5 GHz. Two identical *Minicircuits* Bandpass filters VBFZ-5500-S+ are inserted right at the room temperature microwave output port to reduce noise. The amplified signal must then be down-converted before it can be sampled by an analog-to-digital converter (ADC) board. This down-conversion is conveniently done by a *Marki* IQ mixer IQ-4509, which mixes the measurement signal with a local oscillator (LO) signal. In a heterodyne measurement, the LO signal is offset from the cavity resonance by the intermediate frequency (IF) $f_{\mathrm{IF}} = 5 - 25$ MHz, thus producing the two IQ conjugate quadratures of the IF signal at f_{IF}, well within the frequency range of the data acquisition board. In order to reach the amplitude range of the board of a few mV, the down-converted IF signal is amplified again by a *Minicircuits* ZFL-500LN amplifier with ∼30 dB gain. The signal after the final amplification stage is again filtered by a low-pass filter before it is fed into the ADC converter. In the end, the signal is digitized by an *AlazarTech* dual-channel 16-bit waveform digitizer card ATS9462 with a maximum sampling rate of 180 MS/s.

The IQ conjugate quadrature amplitudes of the IF signal, denoted by X and P, can be

taken directly from the two arms of the mixer output. This process, however, is very sensitive to imbalances and offsets in the mixer or the subsequent amplification chain. To avoid this problem, we choose a different method only using one quadrature, i.e. the so-called digital homodyne process [21] at the cost of a factor of 2 in signal to noise ratio and some reduction of detection bandwidth.

The quadrature components X and P are related to the single channel IF signal

$$A(t) = M(t)\cos(\omega_{\mathrm{IF}}t + \phi) = X\cos(\omega_{\mathrm{IF}}t) + P\sin(\omega_{\mathrm{IF}}t) \tag{6.18}$$

by Fourier transformation,

$$X = \frac{2}{T}\int_T A(t)\cos(\omega_{\mathrm{IF}}t)\,dt \tag{6.19}$$

$$P = \frac{2}{T}\int_T A(t)\sin(\omega_{\mathrm{IF}}t)\,dt \tag{6.20}$$

where the period of the IF signal is $T = 2\pi/\omega_{\mathrm{IF}}$. The amplitude and phase information can be extracted from the quadratures using

$$M = \sqrt{X^2 + P^2}, \quad \phi = \arctan(\frac{P}{X}). \tag{6.21}$$

In our cCPT experiments, we set the IF frequency $f_{\mathrm{IF}} = 5$ MHz and the sampling rate of the acquisition board to be 20 MHz, which means for every (X, P) pair , 4 samples must be taken by the ADC board. The integrals in Eqs.(6.19) and (6.20) are then simplified

to

$$X = \frac{1}{2}(A(t_1) - A(t_3)) \tag{6.22}$$

$$P = \frac{1}{2}(A(t_2) - A(t_4)) \tag{6.23}$$

where $A(t_i)$, $i = 1 - 4$, are the four amplitudes of the single quadrature acquired in a single IF period. Although this digital technique reduces the detection bandwidth to the IF frequency, $f_{\mathrm{IF}} = 5$ MHz is large enough for our cCPT experiments as it is still wider than the cavity bandwidth ∼1.5 MHz.

As calibrated in Subsection 6.1.4, the system noise temperature $T_{\mathrm{sys}} \approx 31$ K, dominated by the HEMT amplifier noise. Thus the noise mode h is assumed to be well approximated by a thermal field with average photon number ∼120, which is also not correlated with the signal mode a. Under this verifiable assumption, the probability distribution of $\hat{A}$, i.e. $D^{[\rho_a]}(A)$, contains all information needed for reconstructing the signal density matrix ρ_a.

We perform repeated measurements of $\hat{A}$ and discretize the probability distribution space into a two-dimensional histogram with a 1024×1024 grid. Two representative measured histograms are shown in Fig. 6.9, where the complex amplitude A is relabeled by the complex amplitude of a coherent state α.

A reference measurement for the amplifier noise is performed first, when there is no detectable emission from the cavity itself. In this situation, the signal mode a is the amplifier noise and the "noise" mode h is the vacuum state. Other histograms for cavity modes are taken where the cCPT emits photons from the cavity at various resonant

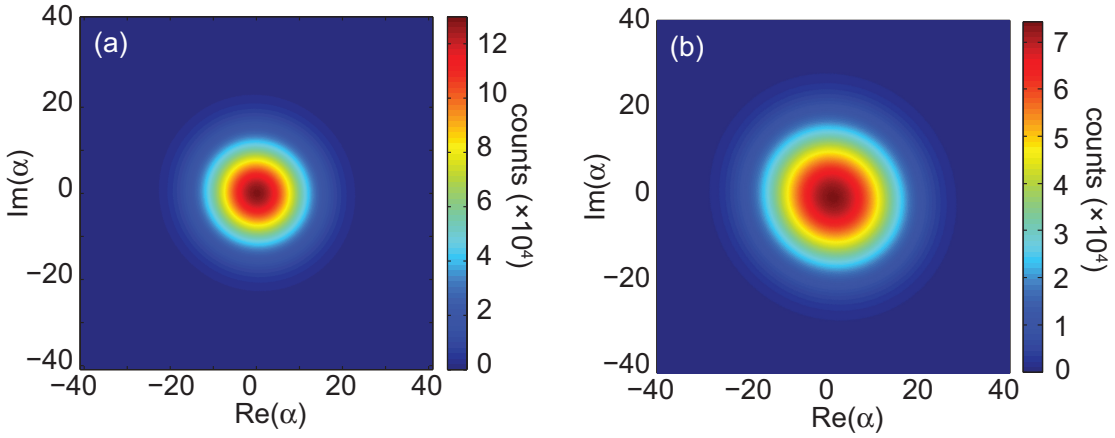

FIGURE 6.9: Measured quadrature histogram $D(A)$ for cCPT output mode a (a) as the amplifier noise and the noise mode h in the vacuum, (b) at the first cotunneling feature $\omega_d = \omega_0/2$ with $n_g = 0.71$.

features. In all cases quadrature data are collected for approximately 26 min, giving a total of 7.86×10^9 data points per histogram. The density matrix of the state can then be extracted from the noisy background through a numerical algorithm, namely, maximum likelihood estimation.

6.2.3 Maximum Likelihood Estimation

The goal of maximum likelihood estimation (MLE) is to find a state of the system that maximizes the probability of obtaining the observed experimental data set. This method has been used in a wide range of fields, e.g. image processing and econometrics. In the case of reconstructing a density matrix, it is guaranteed to generate a physically plausible state, as all the requirements of a density matrix can be incorporated into the MLE procedure [88]; we can constrain the reconstructed density matrix to be Hermitian, positive semi-definite, and of unity trace.

The Iterative MLE Algorithm

Each measurement of the quantum system ρ can be described by a positive operator valued measure (POVM) $\hat{\Pi}_j$, which gives the corresponding outcome with a probability $p_j = \mathrm{Tr}[\rho\hat{\Pi}_j]$. A complete set of POVMs satisfies $\sum_j \hat{\Pi}_j = \mathbb{1}$. The measurement is repeated many times, of which each outcome occurs f_j times. The likelihood function can then be defined as

$$\mathcal{L} = \prod_j p_j^{f_j} = \prod_j \mathrm{Tr}[\rho\hat{\Pi}_j]^{f_j}. \tag{6.24}$$

Given the measurement results, the most probable state ρ_{MLE} is the state that maximize the likelihood $\mathcal{L}$. It can be computed by an iterative procedure [89–91], which introduces a non-negative iteration operator

$$\hat{R}(\rho) = \sum_j \frac{f_j}{\mathrm{Tr}[\rho\hat{\Pi}_j]}\hat{\Pi}_j. \tag{6.25}$$

The iteration for updating the density matrix is then

$$\rho_{k+1} = \mathcal{N}\hat{R}(\rho_k)\rho_k\hat{R}(\rho_k) \tag{6.26}$$

where $\mathcal{N}$ is a normalization factor giving $\mathrm{Tr}[\rho_k] = 1$. In practice, both the phase space and the Fock space must be truncated to finite dimensions; the phase space is discretized as well. As a result, $\hat{G} = \sum_j \hat{\Pi}_j \neq \mathbb{1}$. In this case, iteration (6.26) must be replaced by

$$\rho_{k+1} = \mathcal{N}\hat{G}^{-1}\hat{R}(\rho_k)\rho_k\hat{R}(\rho_k)\hat{G}^{-1}. \tag{6.27}$$

The above algorithm is often referred to as the "$R\rho R$ algorithm" and shows fast convergence over a variety of reconstructions. In the case that the likelihood function does not increase monotonically, a "diluted" algorithm [92] can be introduced, in which the iteration operator $\hat{R}$ defined by Eq. (6.25) is modified as

$$\hat{R}_{\mathrm{dil}} = \frac{\mathbb{1} + \epsilon \hat{R}}{1 + \epsilon} \tag{6.28}$$

where the positive parameter ϵ specifies the step size of each iteration. For $\epsilon \to \infty$, $\hat{R}_{\mathrm{dil}}$ reduces back to $\hat{R}$. For $\epsilon \to 0$, the diluted algorithm is guaranteed to converge monotonically.

Application of MLE to Noise Characterization

Let us apply the MLE procedure to the simplest scenario, where the noise mode h is in the vacuum state. The noise reference measurement is in such a scenario and a representative histogram is shown in Fig. 6.9(a). Since the vacuum state has a P function $P_h(\beta) = \delta^{(2)}(\beta)$, the distribution of the complex amplitude $\hat{A}$ is simplified from Eq. (6.17) to

$$D^{[\rho_a]}(A) = Q_a(A). \tag{6.29}$$

The POVMs are thus defined via

$$\mathrm{Tr}[\rho_a \hat{\Pi}_\alpha] \doteq D^{[\rho_a]}(\alpha) = \frac{1}{\pi} \langle \alpha \left| \rho \right| \alpha \rangle \tag{6.30}$$

where the amplitude operator $\hat{A}$ is again relabeled by the amplitude of a coherent state α. The POVMs are then determined by Eq. (6.30):

$$\hat{\Pi}_\alpha = \frac{1}{\pi}|\alpha\rangle\langle\alpha|. \tag{6.31}$$

In the Fock basis, the matrix elements of the operator Π_α are

$$\Pi_\alpha^{nm} = \frac{1}{\pi}\langle n|\alpha\rangle\langle\alpha|m\rangle = \frac{1}{\pi}e^{-|\alpha|^2}|\alpha|^{n+m}\frac{e^{i(n-m)\theta}}{\sqrt{n!m!}} \tag{6.32}$$

where $\alpha = |\alpha|e^{i\theta}$.

As estimated from the shot noise calibration in Section 6.1.4, the number of system noise photons is $N_{\text{sys}} \approx 120$. In order to reconstruct the noise distribution with high accuracy, a Fock space of a dimension $d \sim 10N_{\text{sys}} \sim 1000$ needs to be taken into account. Another space involved in this algorithm is the discretized histogram space with a dimension of 1024×1024. Given these large dimensions, if one wants to store all the matrix elements $\hat{\Pi}_\alpha^{nm}$ of all accessible POVMs with double precision, one needs a computer memory of $1000^2 \times 1024^2 \times 8 \approx 8$ TB! Even if we re-bin the histogram by a factor of 2 or 4, the memory required is still well beyond the computational power available to us. This leaves us the only other approach for $\hat{\Pi}_\alpha^{nm}$, i.e. calculating all these elements each time for each iteration, which is also very computationally demanding.

Fortunately, we can see from Eq. (6.32) that the magnitude $|\Pi_\alpha^{nm}|$ and complex phase factor of the element $e^{i(n-m)\theta}$ can be calculated separately and combined at the end. If

we take the natural logarithm of the magnitude, we have

$$\ln|\Pi_\alpha^{nm}| = -|\alpha|^2 + (n+m)\ln|\alpha| - \ln\pi - \frac{1}{2}\ln n! - \frac{1}{2}\ln m!. \tag{6.33}$$

The terms that really consume computational power are only $\ln n!$ and $\ln m!$, which can be calculated once for all by Mathematica, stored in a file and stored in the RAM at runtime. The complex phase factor $e^{i(n-m)\theta} = \cos(n-m)\theta + i\sin(n-m)\theta$. Both the sine and cosine terms for different n and m can be calculated from the well-known recurrence relations widely used in Fast Fourier transforms. In addition, because of the symmetry of the α phase space, the number of these calculations can be reduced by a factor of 4 or even 8. More importantly, numerical analysis shows that for each α, the magnitude of the matrix element $|\Pi_\alpha^{nm}|$ is peaked at around $n \approx |\alpha|^2$ and $m \approx |\alpha|^2$ and decays as n and m deviates further from the peak. For a precision of $\epsilon = 10^{-16}$, we calculate the dynamic range of n and m that need to be taken into account for $|\alpha|$ up to 40. We find that on average the number of elements that are significant enough to be calculated is about an order of magnitude smaller than the original number of elements. With all these computational shortcuts, the complexity of the algorithm has been reduced by more than 95%. It is then programmed in C++ code and run on the Dartmouth *Discovery* cluster [93].

Applying the above algorithmic procedure to the reference histogram [Fig. 6.9(a)], the noise state ρ_h is then reconstructed. Its diagonal elements are shown in Fig. 6.10 and are well approximated by a thermal distribution with average photon number $n \approx$

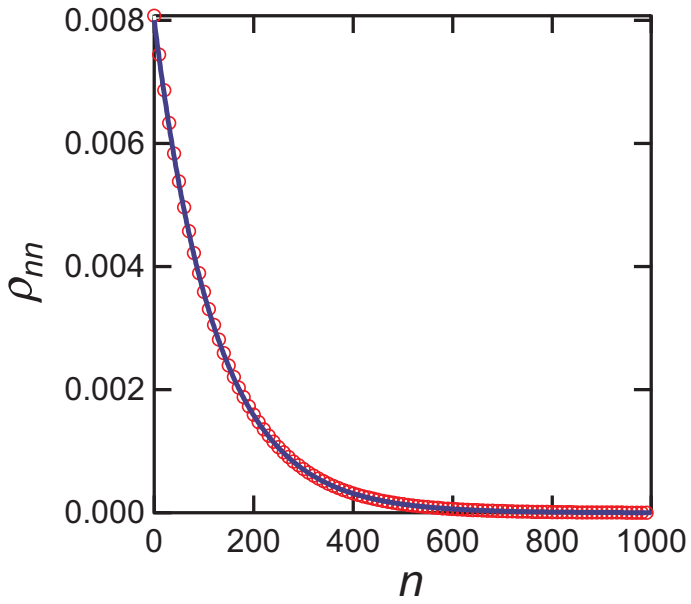

FIGURE 6.10: Diagonal density matrix elements for the reference noise mode reconstructed by the iterative MLE method. The photon distribution (red dots) is well described by a thermal distribution (blue solid line) with average photon number $n \approx 123$. To show the curve fit clearly, the density of data points displayed has been reduced by a factor of 10.

123, in perfect agreement with the shot noise calibration. The maximum value of the off-diagonal elements is less than $5 \cdot 10^{-5}$ and is thus negligible. We have therefore experimentally verified the assumption that the noise mode h being in a thermal state. We can now proceed to extract the signal from the noise background.

Application of MLE to Signal Extraction

For a system with a signal mode a buried in a thermal noise mode h, the modified POVM $\hat{\Pi}_\alpha^{\rho_h}$ obeys

$$\mathrm{Tr}[\rho_a \hat{\Pi}_\alpha^{\rho_h}] \doteq D^{[\rho_a]}(S) = \int_\alpha P_h(S^* - \alpha^*) Q_a(\alpha) d^2\alpha \tag{6.34}$$

and is thus given by

$$\hat{\Pi}_{\alpha}^{\rho_h} = \frac{1}{\pi} T_h(\alpha) \tilde{\rho}_h T_h^{\dagger}(\alpha) \tag{6.35}$$

where the displacement operator is defined as $T_h(\alpha) \equiv e^{\alpha h^{\dagger} - \alpha^* h}$ and $\tilde{\rho}_h$ is the most likely density matrix of the reflected histogram $Q_h(-\alpha^*)$ [86].

In principle, using the procedure described in Subsection 6.2.3, $\tilde{\rho}_h$ can be reconstructed from the noise histogram and $\hat{\Pi}_{\alpha}^{\rho_h}$ can then be calculated via $T_h(\alpha)$. Nevertheless, given the large Fock space we need to use, we would rather avoid the matrix multiplication in Eq. (6.35) for every α. It turns out that given the fact that the noise mode is well approximated by a thermal field with an average photon number $\bar{n}$, the matrix element of the modified POVM $\hat{\Pi}_{\alpha}$ have a closed form expression:

$$\langle m|\hat{\Pi}_{\alpha}^{\rho_h}|n\rangle = \frac{\bar{n}^n}{\pi(\bar{n}+1)^{m+1}} \sqrt{\frac{m!}{n!}} |\alpha|^{n-m} e^{-i(n-m)\theta} \exp^{\left[\frac{-|\alpha|^2}{\bar{n}+1}\right]} L_n^{n-m}\left[\frac{-|\alpha|^2}{\bar{n}(\bar{n}+1)}\right] \tag{6.36}$$

where L_n^k is an associated Laguerre polynomial and $n \geq m$. The other half of elements with $n < m$ can be easily deduced by the Hermiticity of the matrix. The factorial terms and complex phase factor can be calculated the same way as those for $\hat{\Pi}_{\alpha}$ [in Subsection 6.2.3].

Fortunately, the evaluation of the L_n^k is not as difficult as it may seem to be. First, given the strictly negative argument of $L_n^{n-m}(-z)$ $(z > 0)$, its value is positive definite. Also, a recursion relations exists for obtaining $L_n^k(-z)$ at fixed z for rising values of n. Additionally, similar to the behavior of $|\Pi_{\alpha}|$, the magnitude $|\Pi_{\alpha}^{\rho_h}|$ is strongly peaked at the diagonal $n = m$. It drops off so rapidly away from the diagonal that only elements

with $|n-m| \leq 40$ are greater than the tolerance $\epsilon = 10^{-16}$ for $|\alpha|$ up to 40. The complexity and the runtime for calculating $\Pi_\alpha^{\rho_h}$ is therefore even more greatly reduced than that for Π_α.

Having implemented the above algorithm in a C++ program, a maximally likely state of signal mode should in principle be found, given the measured histogram such as Fig. 6.9(b) and an initial state such as the maximally mixed state $\rho_0 = \mathbb{1}/d$, where d is the dimension of the reconstructed Fock space. Nonetheless, because the system has a large number of thermal noise photons ~ 100 as well as a comparable number of cavity photons, the probability space of the likelihood function for the reconstruction is relatively flat. The algorithm may not be able to converge to an optimal state with maximum likelihood before it runs into numerical problems. Consequently, we extend the MLE procedure by seeding the algorithm with different initial states and choose the iteration that converges fastest and changes the least. To have an indicator of the convergence rate, we define the relative change of subsequent matrices at iteration k as

$$C = \frac{||\rho_{k+1} - \rho_k||_{\max}}{||\rho_{k+1}||_{\max}} \tag{6.37}$$

where $||\rho||_{\max} = \max\{|\rho_{ij}|\}$ denotes the max norm of the matrix ρ.

We seed the algorithm with a diagonal matrix whose diagonal elements are given by a discrete Gaussian distribution centered at its predetermined average photon number n_{ph} and the width given by the assigned Fano factor F.

Using histogram 6.9(b), we seed the program with $n_{\text{ph}} = 70$, $F = 0.1 - 1$ and $n_{\text{ph}} = 100$,

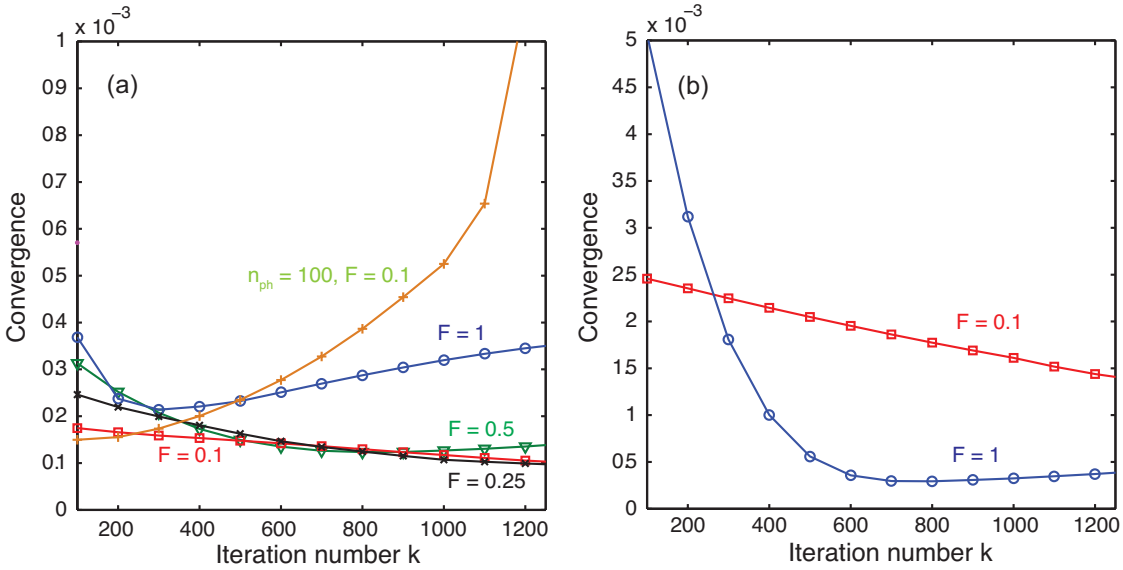

FIGURE 6.11: The convergence plots for the cavity emission field at first cotunneling peak (a) and for the driven nearly coherent state (b).

$F = 0.1$, giving convergence plot shown in Fig. 6.11(a). By integrating the spectrum of the cavity output field, we estimate $n_{\rm ph}$ at the first cotunneling peak to be about 70 [see Fig. 7.7]. The convergence plot is indeed consistent with our estimate: a iteration with a far off photon number $n_{\rm ph} = 100$ diverges quickly, whereas all other iterations with $n_{\rm ph} = 70$ converge almost equally well, except the one with a Fano factor $F = 1$. This implies that the cavity emission field is very likely to have a small Fano factor $F < 1$, i.e. the cavity is in an amplitude squeezed non-classical state.

Similarly, when the cCPT is biased off resonance and no cavity emission occurs, we drive the cavity with an external pure-tone signal at cavity resonance, producing a nearly coherent state cavity. We can see in Fig. 6.11(b) that with roughly correct photon number $n_{\rm ph} \approx 100$, an initial state with a Fano factor of $F = 1$ converges more rapidly and better that the one with $F = 0.1$, which is exactly what we expect for a

coherent state.

In conclusion, while we can not accurately determine the Fano factor from the extended MLE procedure, we can distinguish between quantum and classical states of the cavity field with Fano factor $F \ll 1$ and $F \geq 1$ respectively.

Having reconstructed the density matrices of the photon fields, it is straightforward to obtain the Wigner function distributions by utilizing QuTiP (Quantum Toolbox in Python) [94], an open-source software for simulating the dynamics of open quantum systems. The reconstruction results of the cCPT emission fields will be presented in Section 7.3.

Chapter 7

Results of the cCPT Experiments

Before beginning the experimental investigations on the cCPT system, it is worth briefly summarizing the configuration and key parameters of the cCPT device we discuss during the development process in Chapter 5.

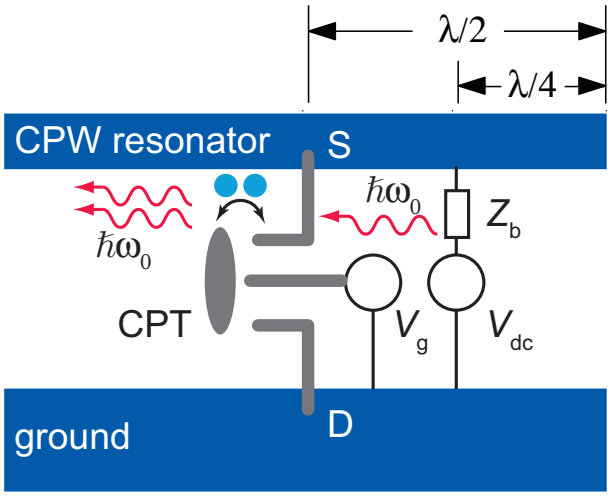

FIGURE 7.1: Schematic illustration of the cCPT circuit

The coplanar waveguide cavity is approximately 21.5 mm long, fabricated from 100 nm thick Nb film and is coupled at either end to the external transmission lines with $Z_0 = 50\,\Omega$ characteristic impedance, via asymmetric input and output capacitors ($C_{\text{in}} =$ 1.65 fF, $C_{\text{out}} =$ 18.5 fF). The cavity has a fundamental full-wave resonant frequency $\omega_0 = 2\pi \times 5.256$ GHz and a quality factor $Q \approx 3500$, giving a photon decay rate $\kappa \approx 2\pi \times 1.5$ MHz.

The wavelength long cavity is modified by placement of dc bias lines at the voltage nodes located one quarter wavelength from either end of the cavity as shown in Fig. 7.1. These bias lines allow application of a dc bias voltage V_{dc} to the center conductor of the cavity without affecting the microwave properties of the cavity at its resonance frequency through a biasing impedance $Z_b = i\omega_0 L_b$ ($L_b \approx 6$ nH).

The CPT is located at the voltage antinode at the center of the main full-wave resonator. It consists of a 7 nm thick superconducting Al island and 70 nm thick source and drain leads, forming two almost identical $\sim 70 \times 70\,\text{nm}^2$ Josephson junctions in series. The source and drain leads are in direct electrical contact of the center conductor and the ground of the cavity, respectively, via proximized 30 nm thick Au/Ti contact pads without introducing additional dissipation. A separate gate voltage V_g is applied to the CPT island through a capacitance C_g to adjust the electrostatic potential via the gate charge $n_g = C_g V_g / e$.

Escaping photons can be measured by microwave circuitry connected to the cavity's output port while the dc bias lines are simultaneously used to probe electrical transport

in the CPT.

For our purposes, the CPT is well described by considering only two charge states, $|0\rangle$ and $|1\rangle$, corresponding to zero and one excess Cooper pairs on the island. These charge states are separated by a gate-dependent electrostatic energy difference $2\varepsilon = 4E_c(1-n_g)$, and coupled to each other via the Josephson energy E_J. The Hamiltonian of the cCPT is thus reduced from Eq.(4.33) to

$$H = \hbar\omega_0 a^\dagger a + \varepsilon\sigma_z - E_J \cos\left[\Delta_{zp}(a + a^+) + \omega_d t\right] \tag{7.1}$$

where σ_x and σ_z are the Pauli matrices. The first two terms in Eq.(7.1) describe the cavity photons and the CPT charge. The third term describes the coupling between charge states, between the CPT and the cavity photons, and the effects of the voltage drive. In a standard CPT (with no cavity and at zero bias), this term would read $E_J\sigma_x \cos\varphi/2$, where φ the total superconducing phase difference between the source and drain, can be treated as a classical variable. In our case, however, quantum fluctuations of the cavity photon field must be accounted for via the identification $\hat{\varphi}/2 = \Delta(a + a^\dagger)$, which proportional to the electric field in the cavity at the location of the CPT. The dimensionless parameter $\Delta = \sqrt{Z_0/R_K} \approx 0.04$ describes strength of the quantum phase fluctuations of the cavity field, which can be important for large numbers of photons in the cavity.

7.1 Electrical Transport in the cCPT

Much can be learn about the cCPT by simply measuring its current I_{CPT} versus dc bias voltage V_{dc} and gate charge n_g, the two macroscopic parameter of the CPT that we have direct control of; a representative image plot of $I_{\mathrm{CPT}}(V_{\mathrm{dc}}, n_g)$ is shown in Fig. 7.2.

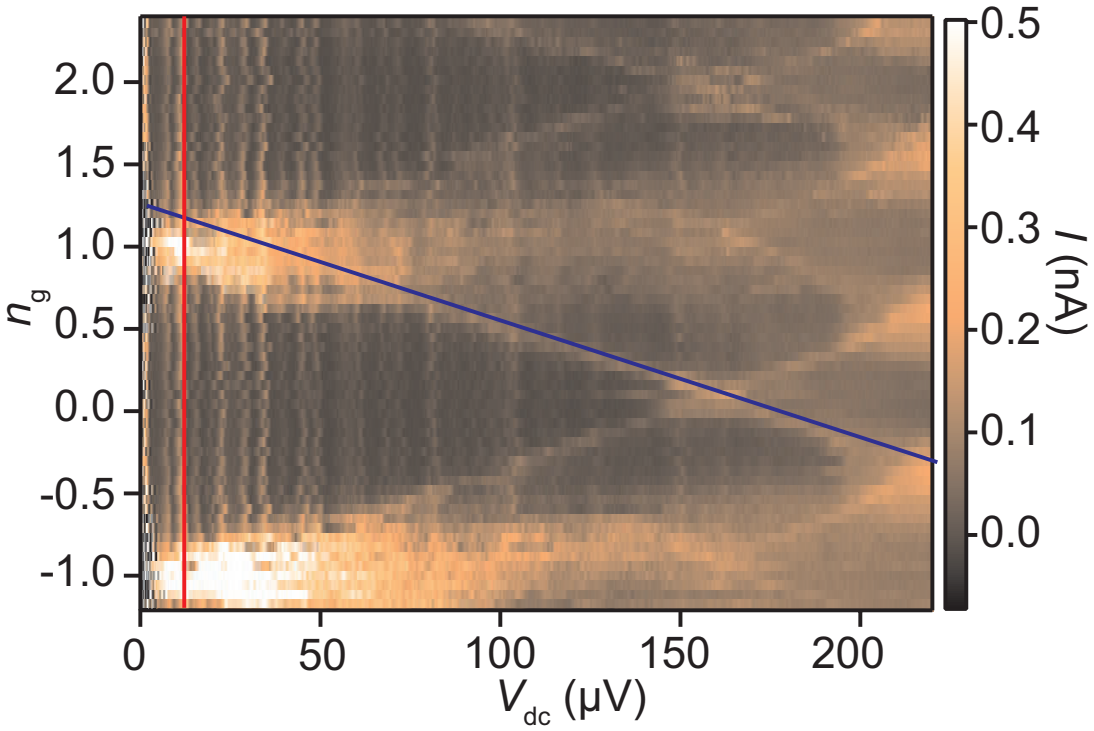

FIGURE 7.2: Current I_{CPT} through the CPT vs. V_{dc} and n_g

The data clearly shows that for sufficiently low V_{dc} the CPT current is $2e$ periodic (period 70 mV in V_g), the transition between $2e$ and e periodicity occurs at $V_{\mathrm{dc}} \approx 150\,\mu\mathrm{V}$. This behavior is an indicator that only Cooper transport is significant for $V_{\mathrm{dc}} < 150\,\mu\mathrm{V}$ and quasiparticle trapping on the island is minimal, so the "poisoning" of the $2e$ periodicity of I_{CPT} has been avoided.

More significantly, the map of I_{CPT} clearly displays a tremendously rich structure, mainly consisting of two parts: a large number of vertical lines, and a somewhat smaller number of diagonal ones. Structures similar to both sets of lines have been seen several similar systems [67, 95–97] consisting of a CPT or SET coupled to either intentional or unintentional low-Q resonances. The features in Fig. 7.2 are unusual, however, in that they are both very sharp and very numerous. In general, these two sets of lines correspond to two distinct varieties of transport processes attributable at the interaction of the CPT with the cavity. They are clear indications of strong couplings between the CPT and the cavity as will be described in detail below.

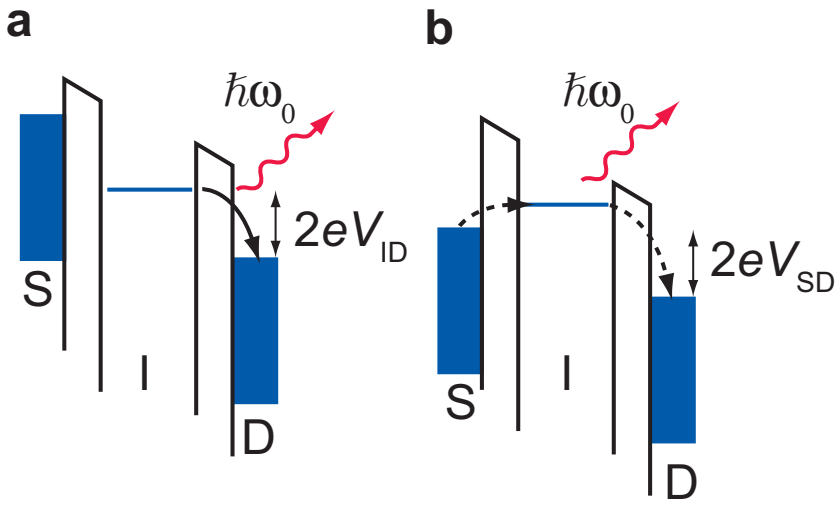

FIGURE 7.3: Sequential tunneling across the island-drain junction and co-tunneling across the CPT both with simultaneous net photon emission.

First, there are sequential tunneling processes involving photon emission, as indicated by diagonal lines in Fig. 7.2. Such processes involve an allowed transition of a Cooper pair across either the source or drain junction, combined with net emission of a photon into the cavity, as illustrated in Fig. 7.3(a).

Second, there are also higher order virtual processes, i.e. cotunneling, indicated by the vertical line with a spacing in $V_{\rm dc}$ of roughly $11\,\mu$V in Fig. 7.2. Here, as shown schematically in Fig. 7.3(b), a Cooper pair is transferred from the source to drain through an energetically forbidden state, again with net emission of a photon into the cavity [96].

It is important to note that in the presence of large numbers of cavity photons, each process can be enhanced by the simultaneous absorption of photons, i.e. stimulated emission of photons in expected to be important, as indicated schematically in Fig. 7.1.

To investigate the coupling of the CPT to cavity photons more carefully, we restrict ourselves to very low applied voltage ($V_{\rm dc} < 30\,\mu$V) and concentrate on the first two cotunneling features at $V_{\rm dc} \approx 11$ and 22 μV in the current map as indicated in Fig. 7.4(a). By way of the ac Josephson effect, the dc bias gives rise to a characteristic drive frequency $\omega_{\rm d} = 2eV_{\rm JJ}/\hbar \approx eV_{\rm dc}/\hbar$, which can be viewed approximately as the frequency of Josephson oscillations across each junction. Here $V_{\rm SD}$ is the source-drain voltage that exists at the CPT. Note that due to the nonlinearity of the system and the presence of the bias impedance Z_b, $V_{\rm SD}$ in general can differ from the applied voltage V_{dc}. The cotunneling features at $V_{\rm dc} \approx 11$ and 22 μV, therefore are an indication of the drive frequencies at $\omega_d \approx \omega_0/2$ and ω_0, respectively. Referring to the diagram for cotunneling in Fig. 7.1(b), these features correspond to the emission of one or two photon into the cavity during Cooper pair tunneling.

Furthermore, detailed behavior of the CPT current I versus the measured source-drain

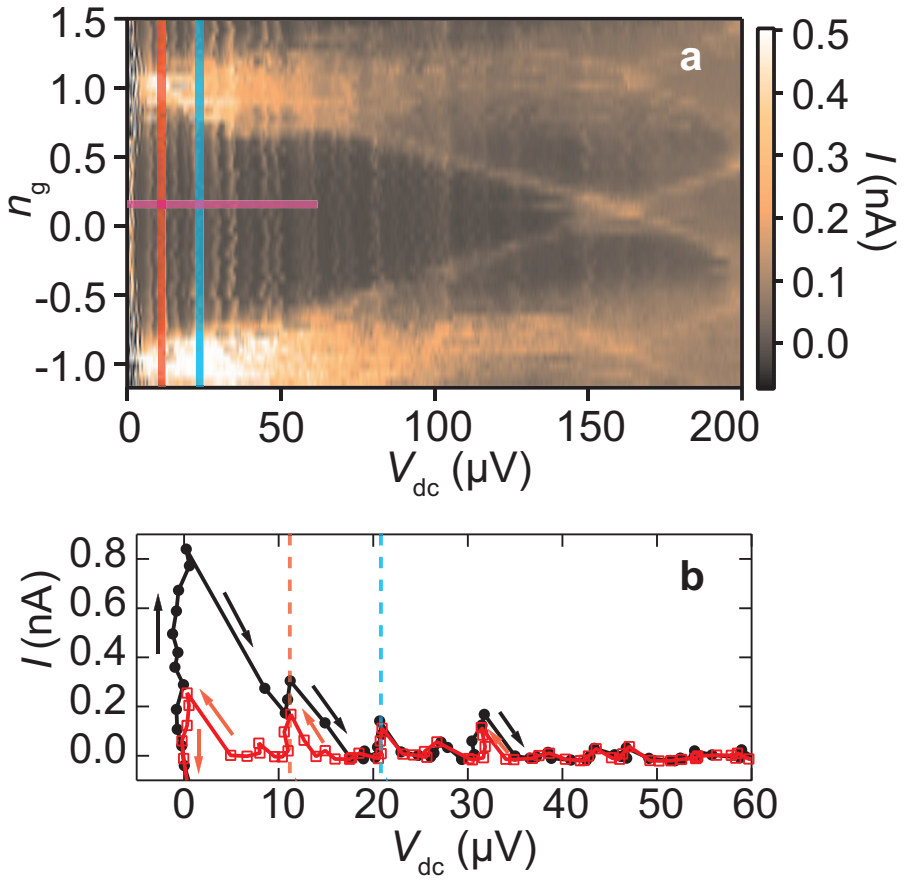

FIGURE 7.4: Transport in the cCPT. (a) Current versus $V_{\rm dc}$ and n_g showing the portions of the parameter space chose for investigation. (b) $I-V$ characteristic for two sweep directions, as indicated, along horizontal magenta line in (a). The vertical dashed red and blue lines indicate the locations of the first and second cotunneling features at $V_{\rm dc} = 11\,\mu$V and $22\,\mu$V respectively.

voltage $V_{\rm dc}$ is shown in Fig. 7.4(b) at a particular gate charge far from the charge degeneracy points $n_g = \pm 1$. The current is strongly hysteretic in $V_{\rm dc}$, indicating the presence of bistability in the cCPT dynamics. Furthermore, these are sharp current steps at fixed voltages, nearly evenly spaced $V_{\rm dc}$. These steps in current correspond to the bright vertical cotunneling lines visible in Fig. 7.4(a).

The structure of individual $I-V$ characteristics as in Fig. 7.4(b), with a steep rise in current at a fixed voltage bias are reminiscent of two phenomena from study of large

area Josephson junctions, namely Shapiro steps [98] and Fiske modes [99, 100]. In both cases, phase locking between a microwave electromagnetic field at frequency f_0 and the Josephson oscillations of a junction subject to a dc voltage bias, lead to series of steps in the $I-V$ characteristic at voltages such that $f_d = nf_0$ where n is an integer. This occurs because the phase across the junction arises from both ac and dc sources. In the case of Shapiro steps the electromagnetic field is from an external source, while in the case of Fiske modes it is self-generated when a dc bias is applied. When the Josephson drive frequency f_d is equal to a multiple of f_0, the ac and dc phases lock and a non-zero dc current results. It is important to note that both Shapiro steps and Fiske modes are classical phase locking phenomena, since the Josephson phase difference is a classical variable in large area junctions [40].

Given the similarity of our data to the above phenomena, it is reasonable to suppose that we are observing phase locking of the CPT with a self-generated field produced by photon emission into the cavity. In fact a detailed theoretical analysis [62] of the cCPT indicates that such emission can in fact occur. Furthermore, since the photons emitted by the CPT are confined to the cavity for a significant period of time due to the large cavity Q, the current steps are an indication that the very photons generated by the tunneling Cooper pairs are in turn directly influencing other tunneling events and subsequent photon emission, i.e. they constitute direct evidence for stimulated photon emission.

7.2 Photon Emission in the cCPT

7.2.1 Electrical Transport & Photon Emission Correspondance

Note that phase locking in the cCPT system differs significantly from that in Fiske modes, for instance. In particular, non-trivial quantum correlations may well exist in the total phase across the CPT, and the state of the photon field inside the cavity could be strongly non-classical. There has been a great deal of attention lately on the closely related notion single artificial atom lading, consisting of much theoretical work [101–103] and a single experiment result [67]. While that result is similar to ours in that in involves an SET embedded in a microwave cavity, there are important differences as well: the SET/cavity coupling was capacitive rather dc; the SET was operated on the Josephson-quasiparticle (JQP) resonance at high bias, so that generation of quasiparticles during transport limited the quantum coherence of the overall system.

In contrast, a measurement of photon emission from the cCPT system using measurement scheme in Fig. 6.2, shows clear evidence of phase locking, proving the presence of stimulated emission in our devices. This can be seen in Fig. 7.5, which shows both the CPT current and simultaneous photon emission at 5.25 GHz for several values of gate voltage. The emission data are collected while sweeping the dc voltage bias down along the solid horizontal lines in Fig. 7.5(d). As can be seen in Fig. 7.5(a)–(c), when the Josephson drive frequency f_d approaches a multiple of cavity resonant frequency, the CPT oscillations at f_d suddenly "snap" to match the cavity resonant frequency, and

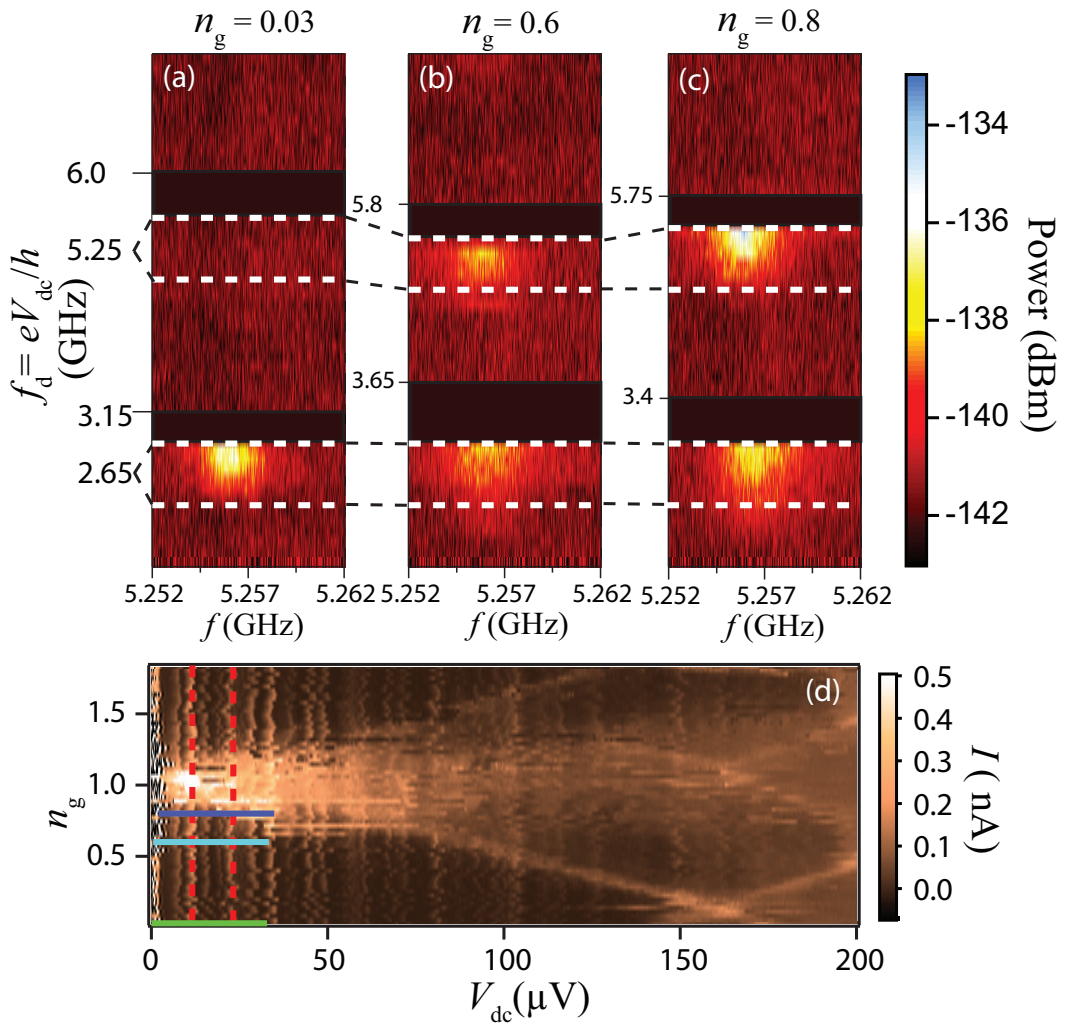

FIGURE 7.5: (a)–(c) Measured photon emission spectrum versus Josephson drive frequency f_d for three different gate charges. Emission is measured along the green, cyan and dark blue lines in the current map (d).

emission suddenly turns on. This behavior is a clear indication of phase locking and strong Cooper pair/photon coupling.

7.2.2 Features in Photon Emission Spectrum

As discussed in Subsection 6.1.3, the noise in the dc bias voltage $V_{\rm dc}$ and accompanying jitter in the drive frequency ω_d can be minimized by switching to the setup shown in Fig. 6.4. Again, we collect the microwave power emitted by the cCPT for a series of different values of n_g for bias voltages surrounding the cotunneling features near $V_{\rm dc} = 11\,\mu$V and $22\,\mu$V. The results from the new scheme, e.g. Figs. 7.6 and 7.7, display a great improvement of the photon emission stability over Fig. 7.5 as expected.

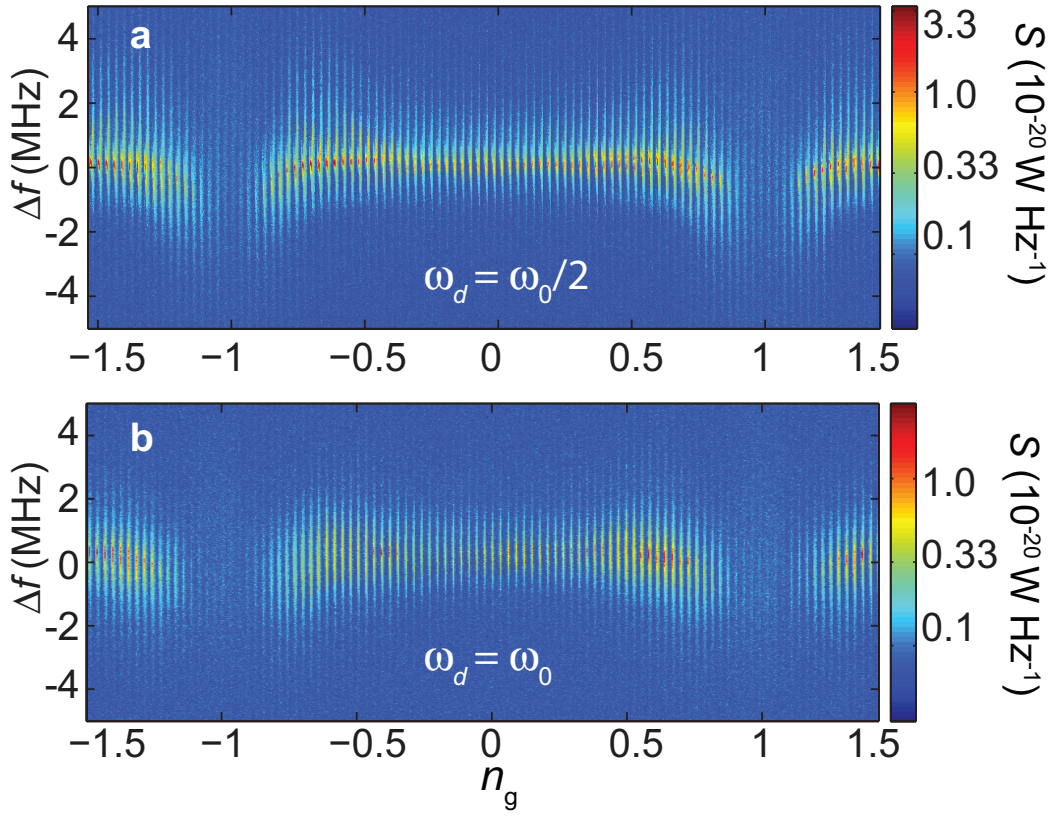

FIGURE 7.6: Microwave spectral power density $S(\omega)$ the cCPT over a 5 MHz span versus detuning $\Delta f = f - f_0$ from the cavity resonance frequency $f_0 = \omega_0/2\pi = 5.256$ GHz for the first (a) and second (b) cotunneling peaks along the red and blue vertical lines in Fig. 7.4(a).

In Fig. 7.6, each vertical band in the data was collected by measuring the output power spectral density S of the cCPT versus frequency over a narrow range of applied voltage $V_{\rm dc}$ at specific gate voltage. The gate voltage was then stepped and the measurement of S repeated. For both set of data $V_{\rm dc}$ was swept from low to high bias.

For both cotunneling features, there is clearly strong emission close to the cavity resonance frequency ω_0; this is particularly striking for the first cotunneling feature, for which the drive frequency $\omega_d = \omega_0/2$. Emission at twice the drive frequency is a direct consequence of the strong nonlinearity of the system. The emission pattern is $2e$ periodic, as is the electrical transport, and shows interesting structure versus n_g. In particular the emission for $\omega_d = \omega_0/2$ appears to develop internal structure for $n_g \geq 0.6$ while for $\omega_d = \omega_0$ there is a clear "hot spot" in the emission for $n_g \approx 0.7$. In both cases, the emission dies out as the gate charge approaches the charge degeneracy points at $n_g = \pm 1$.

A detailed view of the emission at $\omega_d = \omega_0/2$ and $\omega_d = \omega_0$ reveals numerous additional interesting features, as shown in Fig. 7.7, which shows the emission spectra $S(\omega)$ and cavity photon occupation $n_{\rm ph}$ versus applied voltage $V_{\rm dc}$ at representative values of gate charge n_g for both the $\omega_d = \omega_0/2$ and $\omega_d = \omega_0$ cotunneling features.

For the $\omega_d = \omega_0/2$ resonance in Fig. 7.7 we see that as might be expected for a single-atom emitter there is no clear sign of a lasing threshold, with the cavity occupation $n_{\rm ph}$ climbing smoothly from zero as $V_{\rm dc}$ is increased. For low $V_{\rm dc} \leq 13\mu$V the emission linewidth of roughly 1 MHz shows modest narrowing over the intrinsic cavity linewidth

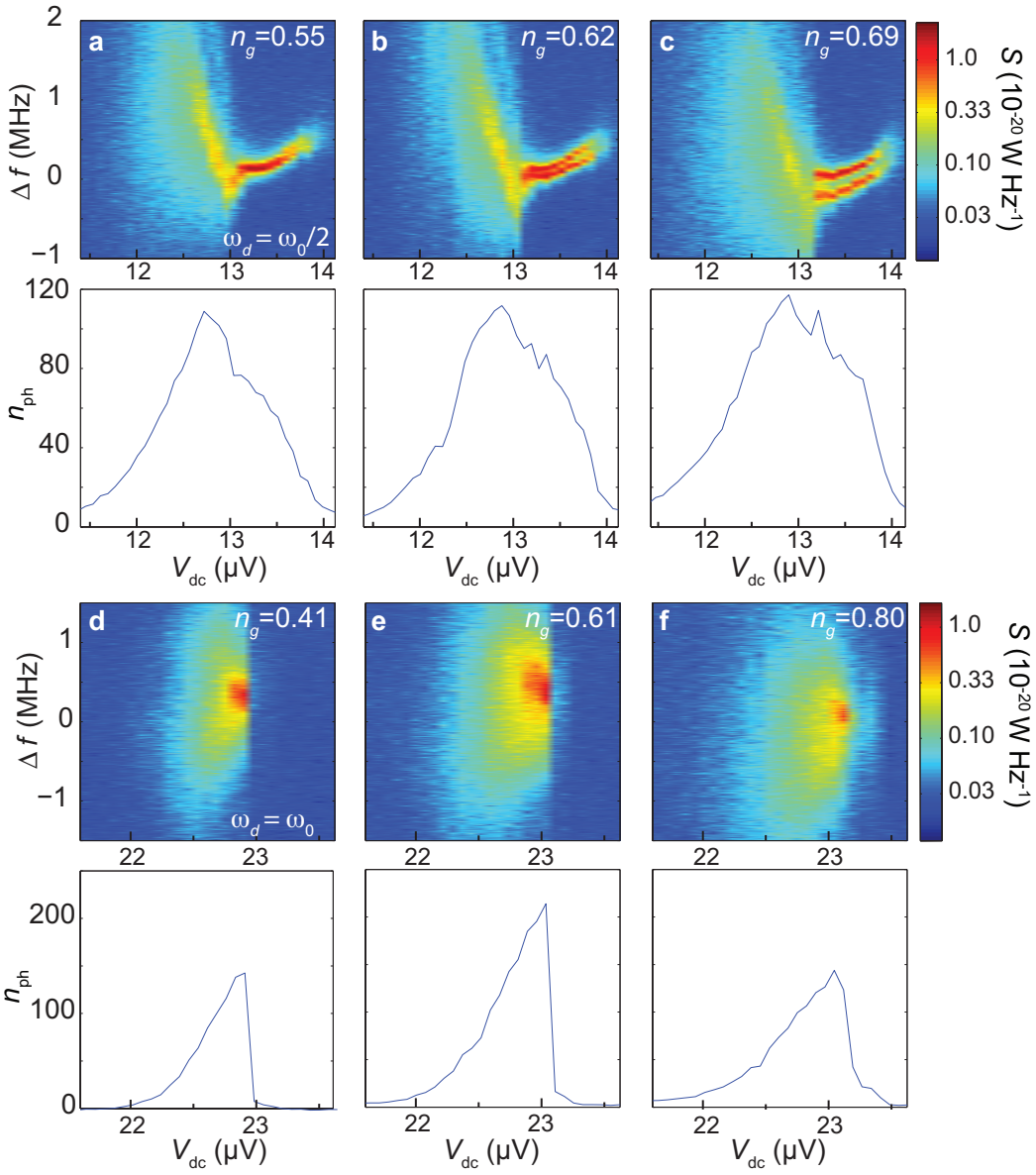

FIGURE 7.7: Detailed emission spectra. (a)–(c), Top panels: emission for $\omega_d = \omega_0/2$ versus applied bias voltage $V_{\rm dc}$ for $n_g = 0.55$, 0.62 and 0.69. $V_{\rm dc}$ was swept from low to high bias in 80 nV increments. Bottom panels: cavity photon occupation $n_{\rm ph} = P/\kappa\hbar\omega$ versus $V_{\rm dc}$ for each gate voltage where P is the integrated emission power. (d)–(f) Emission and cavity photon occupation $n_{\rm ph}$ for $\omega_d = \omega_0$ versus applied bias voltage $V_{\rm dc}$ for $n_g = 0.55$, 0.62 and 0.69. $V_{\rm dc}$ was swept from low to high bias in 75 nV increments. All emission spectra are plotted versus detuning Δf.

$\kappa = 1.5$ MHz. At $V_{\mathrm{dc}} \approx 13\,\mu$V, there is a sudden sharp change in the emission pattern: the linewidth suddenly drops by roughly an order of magnitude, to as low as 70 kHz. The cavity photon occupancy n_{ph} reaches a maximum value on the order of 100 before dropping sharply, stabilizing briefly, and then rapidly declining.

Strikingly, as charge degeneracy is approached, the sharpened spectrum splits into two narrowly separated peaks at around $n_g = 0.62$. The separation of these peaks increases as n_g approaches charge degeneracy. Furthermore, there is a notable shift in the emission frequency toward negative detuning for the same gate voltage range, and an even more notable shift toward negative detuning for large n_{ph}. This latter tendency results in the characteristic "V" shape of the emission versus V_{dc}.

For the $\omega_d = \omega_0$ emission spectra share some features with those for $\omega_d = \omega_0/2$; there are, however, significant differences as well. There is again no clear sign of a threshold as V_{dc} is increased, and there is again a tendency though less pronounced pulling toward negative detuning as charge degeneracy is approached or n_{ph} is increased. There is no sudden sharpening of the spectrum in this case; instead, the emission simply cuts off abruptly for $V_{\mathrm{dc}} \geq 23\,\mu$V, just after the cavity reaches its maximum occupancy of roughly $n_{\mathrm{ph}} \approx 200$. The minimum linewidth of the emission spectra is roughly 500 kHz, significantly below the bare cavity linewidth, but not by as much as that for the $\omega_d = \omega_0$ resonance.

Some aspects of this behavior can be explained within a semiclassical model of the cCPT system [104]. The emission of cavity photons at ω_0 for both $\omega_d = \omega_0/2$ and

ω_0 resonances can be explained dynamically by considering the time dependence of the drive term $\sigma_x \cos\left[\Delta(a + a^\dagger) + \omega_d t\right]$ in the cCPT Hamiltonian. It can be shown that σ_x oscillates at odd harmonics of the drive frequency ω_d; the nonlinearity of the system in the form of the product σ_x with a sinusoidal function of ω_d leads to an overall oscillation at the cavity resonant frequency ω_0. The semiclassical analysis also correctly predicts the approximate number of photons n_{ph} in the cavity for both cases. Additional progress can be made by treating the CPT when far from charge degeneracy as an effective single junction system. Under this approximation, and using either a rotating wave approximation or a semiclassical approximation, it can be shown that the $\omega_d = \omega_0/2$ resonance can, for sufficiently large amplitude, undergo a bifurcation that leads to spectral splitting similar to that in Fig. 7.6. Nonetheless, many aspects of the emission remain unexplained, making the cCPT emission a rich topic for continued theoretical investigation.

7.2.3 Multiphoton Stimulated Emission Process

Another possible explanation for the spectral splitting in the cCPT spectra at various values of gate charge n_g along the first cotunneling feature [in Fig. 7.6(a)] could be the occurrence of a strong resonance between the qubit states of the CPT and the cavity photons. These resonances need to be considered separately for the two different junctions, since the voltage drop across each junction can be different, and when completing a charge/photon transport cycle transitions across different junctions will begin with a different island charge state.

Given that the CPT is embedded in a cavity containing many photons, the most general kind of transition we can consider is one that involves absorption or emission of multiple photons. Furthermore, since we are interested in a charge transport cycle that will increase the number of photons in the cavity by one (since we are concerned with features on the first cotunneling feature), it is reasonable to consider first two particular kinds of transition, as illustrated in Fig. 7.8.

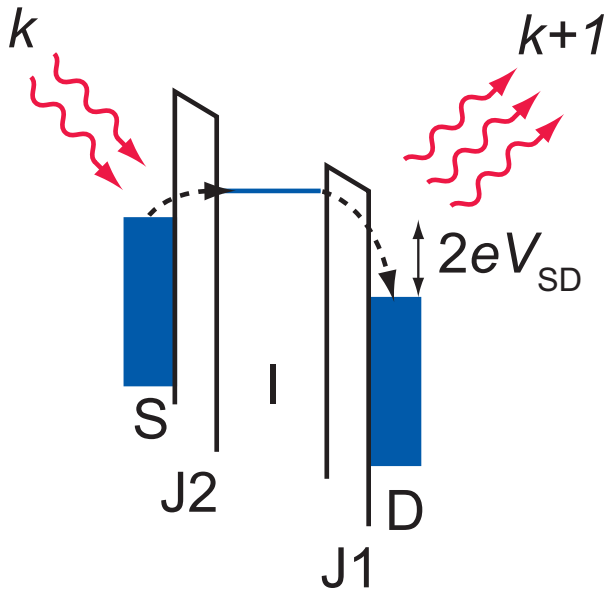

FIGURE 7.8: Schematic illustration of the charge/photon transport process involving multiphoton emission.

First, we assume the CPT is grounded at one end (J2) while the other end (J1) is held at a positive voltage $V_{\rm dc}$. Cooper pairs will then tunnel onto the CPT through J2 and off through J1. Furthermore, if the Cooper pair absorbs k photons when tunneling onto the island it, it must then emit $k+1$ when tunneling off to guarantee conservation of energy during the transport cycle. We therefore consider the processes $0 \Rightarrow 2$ with absorption of k photons through J2, and $2 \Rightarrow 0$ with emission of k + 1 photons through J1.

To determine the values of gate charge n_g and bias voltage $V_{\rm dc}$ for which these processes can be resonant, we turn to the combined charge/photon transition rules given by [95]

$$\sum_i \kappa_i \, m_i \, eV_{\rm dc} = 2\,\delta m\, E_c(n - n_g + \delta m/2) \pm k\hbar\omega_0 \tag{7.2}$$

where $m_{1(2)}$ is the number of electrons tunneling across junction J1(2), $\delta m = m_2 - m_1$, n is the initial charge state of the island, $n_g = C_g V_g/e$ is the number of offset gate charge, k is the number of photons emitted (+) or absorbed (–), and $\kappa_{1(2)}$ is the fraction of the bias voltage dropped across J1(2). In this case, $\kappa_1 = (C_2 + C_g)/C_\Sigma$ and $\kappa_2 = C_1/C_\Sigma$. Eq. (7.2) is a simple extension of Eq. (4.9) to the case where photons are involved.

Using Eq. (7.2), we find that the transition $0 \Rightarrow 2$ with absorption of k photons is resonant for J2 along the line

$$\kappa_2 eV_{\rm dc} = 2E_c(-n_g + 1) - k\hbar\omega_0/2 \tag{7.3}$$

while the the transition $2 \Rightarrow 0$ with emission of $k+1$ photons is resonant for J1 along the line

$$\kappa_2 eV_{\rm dc} = -2E_c(-n_g + 1) + (k+1)\hbar\omega_0/2. \tag{7.4}$$

By inspection, it is clear that both transitions can be simultaneously resonant if $2eV_{\rm dc} = \hbar\omega_0$. Solving for the resonant gate voltages we find that

$$n_g = 1 - \frac{k + \kappa_2}{\kappa_1 + \kappa_2}\frac{\hbar\omega_0}{4E_c} \tag{7.5}$$

so that there are a series of resonances along the line $2eV_{\rm dc} = \hbar\omega_0$. If $\kappa_1 = \kappa_2 = 1$, then Eq. (7.5) becomes

$$n_g = 1 - (k + 1/2)\frac{\hbar\omega_0}{4E_c}. \tag{7.6}$$

Note that for $k \neq 0$ all the resonances clearly describe stimulated emission processes.

For the measured capacitances of the cCPT device discussed in this chapter, namely $C_1 = 1.08$ fF, $C_2 = 1.14$ fF, and $C_g = 4.6$ aF, we have $\kappa_1 = 0.515$, $\kappa_2 = 0.485$ and $E_c = 36\,\mu eV = h \times 8.7$ GHz. The photon energy is $\hbar\omega_0 = h \times 5.26$ GHz while for reference the Josephson energy $E_J = 63.6\,\mu eV = h \times 17$ GHz. Substituting the measured capacitances, charging energies and photon energies into Eq. (7.5), we obtain the following values of n_g for which resonances are expected to occur, along with the corresponding number k of photons absorbed:

k	n_g
0	0.93
1	0.78
2	0.62
3	0.47
4	0.32
5	0.17
6	0.02

TABLE 7.1: Expected values of the gate charge n_g for the multiphoton resonances

The pattern formed by the resonances is illustrated in Fig. 7.9, which plots the lines (7.4) and (7.3) versus n_g in units of $eV_{\rm dc}/4E_c$. The zero-photon resonances for the $0 \Rightarrow 2$ and $2 \Rightarrow 0$ transitions are shown as solid black lines, while resonances from lines (7.3) and (7.4) for $k = 0$ are shown as red and blue dashed lines respectively, which intersect

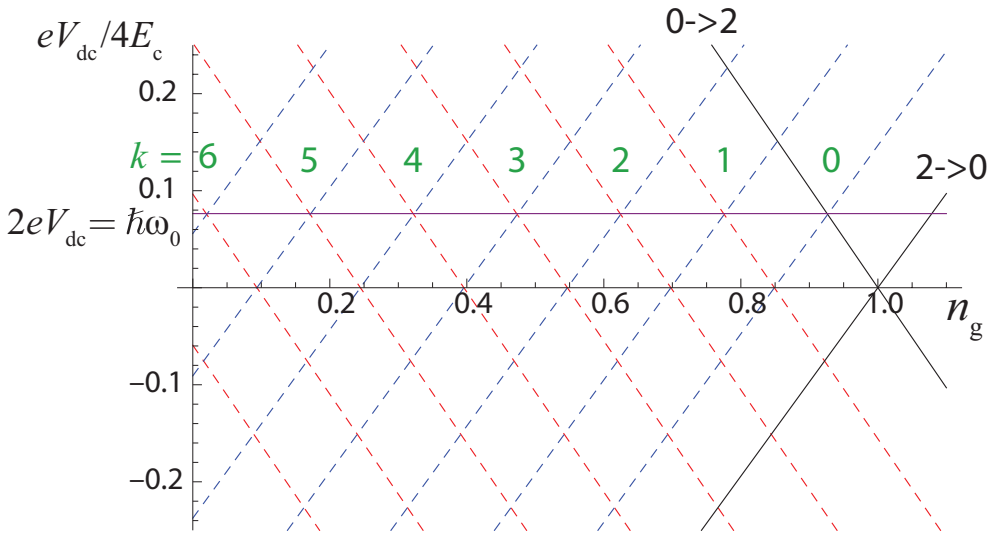

FIGURE 7.9: Schematic illustration of the multiphoton resonances lines. As can be seen in the figure, the k photon absorption process (red dashed lines) is simultaneously resonant with the $k+1$ emission process (blue dashed lines) at $V_{dc} = \hbar\omega_0/2e$ for a particular gate charge n_g between 0 and 1. The entire set of resonances appears at evenly spaced gate voltages along the line $2eV_{dc} = \hbar\omega_0$ defining the location of the first cotunneling feature in the transport and emission measurements.

at $2eV_{dc} = \hbar\omega_0$ for a series different gate charges. The location of the kth resonance is indicated by a green number.

To compare with experiment, we have plotted the locations in n_g of the various resonances from the table above as set of vertical dashed lines in the plot of emission versus detuning and gate charge n_g shown in Fig. 7.10. The agreement seems very good, with new features in the emission spectra appearing at or near the resonance lines in several cases. The level of agreement seems particularly notable for the $k = 3$ resonance, but is also good for $k = 1$ and $k = 2$. Signs of splitting, while less noticeable, are even present near $k = 6$.

While this simple pictures tells us the gate voltages at which the various resonances occur, it does not tell us what happens in the vicinity of a particular resonance, e.g.

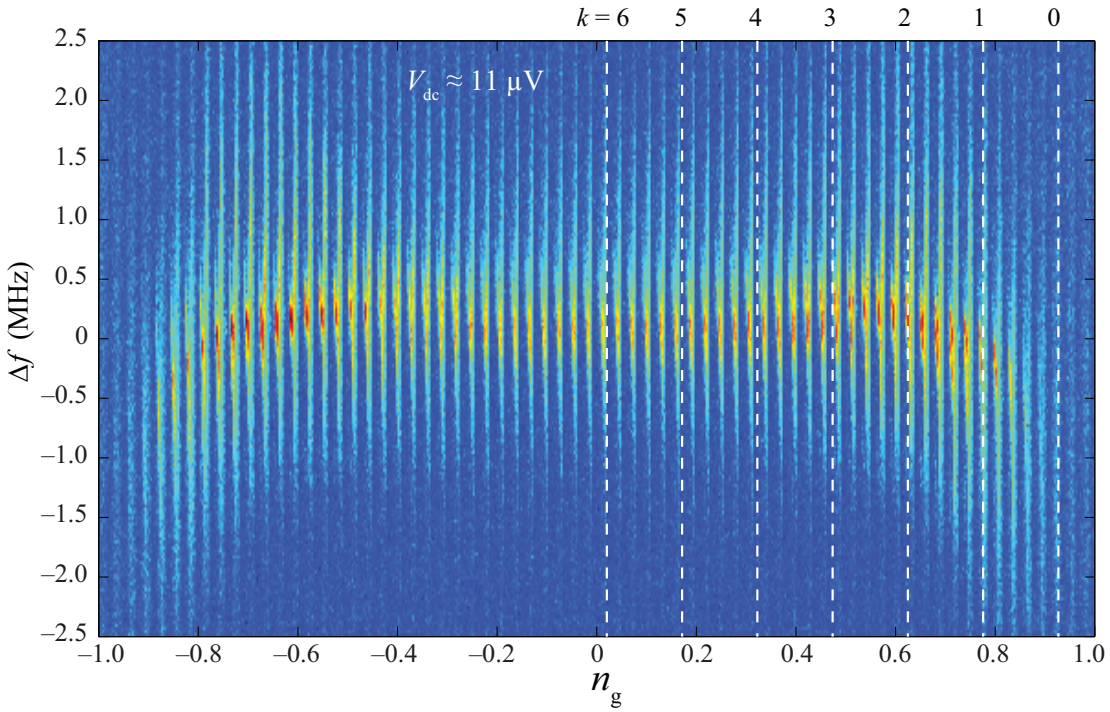

FIGURE 7.10: Emission spectra versus detuning Δf and gate charge n_g for bias voltages in the range of the first cotunneling feature at $V_{\rm dc} \approx 11\,\mu$V. The expected locations of the various multiphoton resonances are shown as the vertical dashed lines.

the pulling of the emission frequency, which makes the cCPT emission a rich topic for continued theoretical investigation.

7.3 Quantum State Reconstruction in the cCPT

Finally, we turn to the question of the nature of the photon field in the cavity, and whether it is better described as a classical or quantum state. Intuitively, given the highly quantum nature of the electronic/photonic transport in the cCPT we expect that the cavity photon field most likely has non-classical correlations of some kind. For instance, it is well known that in the cCPT Cooper pairs must tunnel one at a time; furthermore,

it is clear from the I-V characteristics in Fig. 7.4(b) that the charge transport is phase locked to the cavity photon field. This implies that Cooper pair tunneling events, and therefore photon emission events, occur at more less equally spaced time intervals. As a result, we expect that the photon statistics in the cavity should be sub-Poissonian; i.e., we expect the cavity Fano factor $F = \langle n_{\rm ph}^2 \rangle - \langle n_{\rm ph} \rangle^2 / \langle n_{\rm ph} \rangle$ to be less than unity.

This expectation is supported by several theoretical calculations. Far from the charge degeneracy points we again treat the CPT will act as an effective single junction system. Making this approximation, and using either a rotating wave approximation, or a complete quantum calculation in a Floquet basis, we find that the predicted Fano factor for systems parameters comparable to the experiment is $F \approx 0.3$, which would place the system firmly in the quantum regime for which $F < 1$. In fact, suppression of photon number fluctuations leading to a reduced Fano factor seems to be a generic property of the system, whether biased on the cotunneling features considered here on on the sequential tunneling features also visible in Fig. 7.2.

To investigate this question experimentally, we have performed full quantum state tomography of the density matrix ρ_a describing the cavity photon field by applying techniques for state reconstruction using linear detectors to the cCPT. This is accomplished for a given cavity state by measuring a histogram $D^{[\rho_a]}(A)$ where A is the measured complex cavity field output amplitude referred to the input of a cryogenic HEMT amplifier with a system noise temperature $T_n = 31$ K. We use maximum likelihood estimation to find an estimate for ρ_a that is likely to produce the measured distribution given the

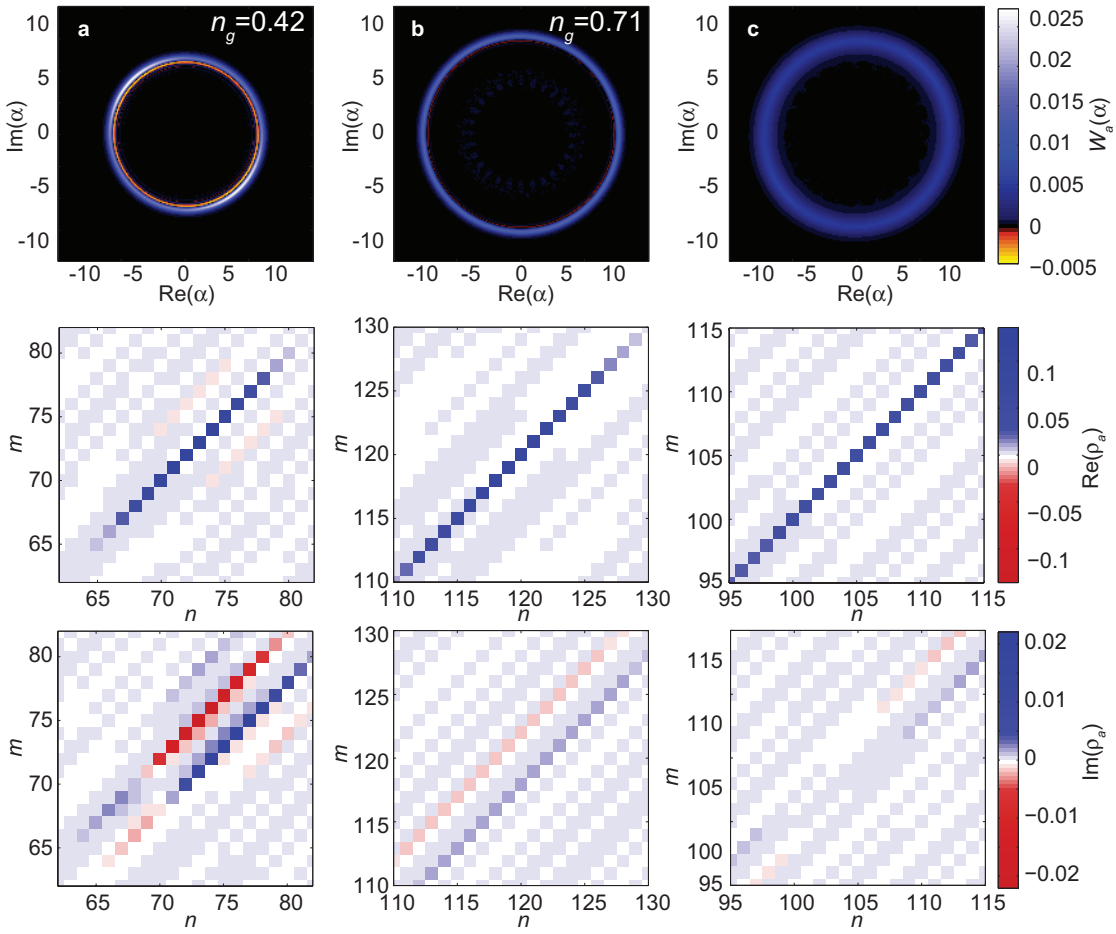

FIGURE 7.11: Quantum state tomography of the cavity field. We shown the Wigner distribution $W_a(\alpha)$ of the cavity mode (top panels) along with the real and imaginary parts of the density matrix ρ_a (bottom panels) for three different states of the cavity field. a, Cavity biased on the $\omega_d = \omega_0/2$ resonance at $n_g = 0.42$; for the reconstruction shown $F = 0.12$. b, Cavity biased on the $\omega_d = \omega_0$ resonance at $n_g = 0.71$; for the reconstruction shown, $F = 0.16$. c. Cavity biased off resonance so that cavity emission does not occur. In this case the cavity is driven by a coherent state such that it contains roughly $n_p h = 106$ photons. For the reconstruction shown $F = 1.6$. The transmitted photons were collected and analyzed in the same fashion as the internally generated photons in a and b. In all cases the cavity field quadratures were sampled in a 1024×1024 grid at a rate of 5 MHz by using digital homodyne detection. In all cases data was collected for approximately 26 min, giving a total of 7.8×10^9 data points per histogram.

presence of the amplifier noise. The density matrix ρ_a is in turn used to calculate the Wigner quasi-probability distribution $W_a(\alpha)$ for the cavity field.

Results of these calculations are shown for three different cavity states are shown in Fig. 7.11 . For the $\omega_d = \omega_0/2$ resonance in Fig. 7.11(a), we see that the Wigner function $W_a(\alpha)$ is sharply peaked near $|\alpha| = 8.7$, in agreement with the estimated photon number $n_{\rm ph} \approx 73$. Notably, there are regions for which $W_a(\alpha)$ is negative, an indication of the quantum state of the cavity field. Interestingly, $W_a(\alpha)$ is not circularly symmetric despite being a time average. This lack of symmetry can also be seen in $\mathrm{Im}(\rho_a)$, for which substantial non-zero off- diagonal components exist, primarily in the matrix elements $\mathrm{Im}(\rho_a)_{n,n\pm2}$. For the $\omega_d = \omega_0$ resonance shown in Fig. 7.11(b), the behavior of $W_a(\alpha)$ is similar, with a sharp peak occurring at $|\alpha| = 10.9$. There is again a small negative region in $W_a(\alpha)$, though less so than for the $\omega_d = \omega_0/2$ resonance. Some asymmetry is present in $W_a(\alpha)$, as are non-zero off-diagonal components in $\mathrm{Im}(\rho_a)$, though neither is as pronounced as for $\omega_d = \omega_0/2$.

In general, due to the large number of cavity photons $n_{\rm ph} \approx 70$ and noise photons $n_h = k_B T_n/\hbar\omega_0 \approx 123$ we find that the probability space for ρ_a is relatively flat, making it difficult to determine the optimal ρ_a and there- fore the cavity Fano factor with precision. For instance, for $\omega_d = \omega_0/2$ we find that ρ_a corresponding to states with Fano factors in the range $F \approx 0.1 - 0.3$ describe the data equally well. The asymmetry in $W_a(\alpha)$ shown in Fig. 7.11(a)(b) is present in all reconstructions, regardless of the resulting value of F. Finally, some negativity is present in $W_a(\alpha)$ in all reconstructions for the $\omega_d = \omega_0/2$ resonance with F in the range given above, although the negativity

weakens for larger values of F. These results, in combination with the supporting theoretical calculations mentioned above, provide strong evidence of the presence of a continually generated non-classical state of light in the cavity that can be maintained for minutes at a time.

While we cannot determine the precise value of the Fano factor for the cavity emission, we note that can distinguish between quantum and classical states of the cavity field. To demonstrate this, in Fig. 7.11(c) we drive the cavity with an external microwave signal, producing a cavity state that is very nearly a coherent state. During this measurement the cCPT was biased far from any resonances so that no measurable dc current flowed and there was no detectable emission from the cCPT itself. Here, in contrast to the cases for internally generated photons in Fig. 7.11(a)(b), best results are obtained for a significantly broader Wigner function that is everywhere positive. Furthermore, there is little sign of the asymmetry in $W_a(\alpha)$, and the off-diagonal elements of $\mathrm{Im}(\rho_a)$ are significantly smaller.

In conclusion of this section, we demonstrated generation of non-classical microwave photons in the cCPT by means of a new quantum coherent transport process involving the interaction of Cooper pairs and photons. The cCPT may serve as a convenient, easy to use source of amplitude squeezed light, and could form the basis of a new class of electrical or photonic amplifiers. It could also serve as an important platform for the study of the quantum dynamics of strongly nonlinear systems.

7.4 Conclusions

Non-classical states of light, ranging from photon number states to quantum superposition states and squeezed light, are an important consequence of the nonlinear interaction of light with matter. Such non-classical states are essential for the use of continuous variables for quantum information processing, and could allow for quantum-enhanced measurement sensitivity. Ideally, one would like to produce large numbers of non-classical photons in a steady stream and in a simple fashion.

In this dissertation, we presented evidence for continual production of such non-classical states of light by means of simultaneous quantum coherent transport of Cooper pairs and microwave photons. By applying a dc voltage to a superconducting artificial atom, the Cooper pair transistor embedded in a superconducting microwave cavity, we use the ac Josephson effect to inject photons into the cavity. The back reaction of the photons on the artificial atom results in new regime of strongly correlated electronic- photonic transport.

We performed full quantum state tomography of the cavity electromagnetic field using maximum likelihood estimation of the photon density matrix, finding strong evidence of the existence of an amplitude-squeezed state. The cavity-embedded Cooper pair transistor (cCPT) offers great potential for study of the quantum dynamics of nonlinear systems, and may lead to new paths for strong coupling between photons and other quantum systems such as spins [105] or nanomechanical resonators [106].

Bibliography

[1] E. Schrodinger. Die gegenwartige Situation in der Quantenmechanik. *Die Naturwissenschaften*, 23(48):807–812, November 1935. ISSN 0028-1042. doi: 10.1007/BF01491891. URL http://adsabs.harvard.edu/abs/1935NW.....23..807S.

[2] T Bhattacharya, S Habib, and K Jacobs. The Emergence of Classical Dynamics in a Quantum World. *Los Alamos Science*, (27):110–125, 2002. URL http://books.google.com/books?hl=en&lr=&id=x7rj83I98yMC&oi=fnd&pg=PP9&dq=Classical+Dynamics&ots=uq_Q2P-iro&sig=-d_klA3iU0P-GG_BKwG5FZ4zfaMhttp://arxiv.org/abs/quant-ph/0407096.

[3] Hermann Wimmel. *Quantum Physics and Observed Reality: A Critical Interpretation of Quantum Mechanics*. World Scientific, 1992. ISBN 9810210108. URL http://books.google.com/books?id=-4sJ_fgyZJEC&pgis=1.

[4] Dhatfield. File:Schrodingers cat.svg - Wikipedia, the free encyclopedia, 2008. URL http://en.wikipedia.org/wiki/File:Schrodingers_cat.svg.

[5] Christopher Gerry and Peter Knight. *Introductory Quantum Optics*. Cambridge University Press, 2005. URL http://books.google.com/books/about/Introductory_Quantum_Optics.html?id=CgByyoBJJwgC.

[6] William B. Case. Wigner functions and Weyl transforms for pedestrians. *American Journal of Physics*, 76(10):937, 2008. ISSN 00029505. doi: 10.1119/1.2957889. URL http://link.aip.org/link/AJPIAS/v76/i10/p937/s1&Agg=doi.

[7] J. Jun John Sakurai and Jim J. Napolitano. *Modern Quantum Mechanics*. Addison-Wesley, 2011. ISBN 0321503368. URL http://books.google.com/books?id=2zm-bwAACAAJ&pgis=1.

[8] S Habib. Nonlinear quantum dynamics. *Non-Linear Dynamics and Fundamental Interactions*, 2006. URL http://link.springer.com/chapter/10.1007/1-4020-3949-2_4.

[9] Itamar Katz, Ron Lifshitz, Alex Retzker, and Raphael Straub. Classical to quantum transition of a driven nonlinear nanomechanical resonator. *New Journal of Physics*, 10(12):125023, December 2008. ISSN 1367-2630. doi: 10.1088/1367-2630/10/12/125023. URL http://stacks.iop.org/1367-2630/10/i=12/a=125023?key=crossref.2e4da75407cc8be3129cbf943320035b.

[10] MI Dykman. Quantum Measurements with Dynamically Bistable Systems. *Applications of Nonlinear Dynamics*, pages 1–12, 2009. URL http://link.springer.com/chapter/10.1007/978-3-540-85632-0_30.

[11] M. Dykman. Critical exponents in metastable decay via quantum activation. *Physical Review E*, 75(1):1–4, January 2007. ISSN 1539-3755. doi: 10.1103/PhysRevE.75.011101. URL http://link.aps.org/doi/10.1103/PhysRevE.75.011101.

[12] I. Siddiqi, R. Vijay, F. Pierre, C. M. Wilson, M. Metcalfe, C. Rigetti, L. Frunzio, and M. H. Devoret. RF-Driven Josephson Bifurcation Amplifier for Quantum Measurement. *Physical Review Letters*, 93(20):1–4, November 2004. ISSN 0031-9007. doi: 10.1103/PhysRevLett.93.207002. URL http://link.aps.org/doi/10.1103/PhysRevLett.93.207002.

[13] Michael A. Nielsen and Isaac L. Chuang. *Quantum Computation and Quantum Information*. Cambridge University Press, 2000. ISBN 0521635039. URL http://books.google.com/books?id=aai-P4V9GJ8C&pgis=1.

[14] Richard P. Feynman. Simulating physics with computers. *International Journal of Theoretical Physics*, 21(6-7):467–488, June 1982. ISSN 0020-7748. doi: 10.1007/BF02650179. URL http://link.springer.com/10.1007/BF02650179.

[15] D. Deutsch and R. Jozsa. Rapid Solution of Problems by Quantum Computation. *Proceedings of the Royal Society A: Mathematical, Physical and Engineering Sciences*, 439(1907):553–558, December 1992. ISSN 1364-5021. doi: 10.1098/rspa.1992.0167. URL http://rspa.royalsocietypublishing.org/content/439/1907/553.

[16] Peter W. Shor. Polynomial-Time Algorithms for Prime Factorization and Discrete Logarithms on a Quantum Computer. *SIAM Review*, 41(2):303–332, January 1999.

ISSN 0036-1445. doi: 10.1137/S0036144598347011. URL http://epubs.siam.org/doi/abs/10.1137/S0036144598347011.

[17] Lov K. Grover. A fast quantum mechanical algorithm for database search. In *Proceedings, 28th Annual ACM Symposium on the Theory of Computing*, page 212, May 1996. URL http://arxiv.org/abs/quant-ph/9605043.

[18] MH Devoret and J. M. Martinis. Implementing qubits with superconducting integrated circuits. *Quantum Information Processing*, 3(October):163–203, 2004. URL http://link.springer.com/article/10.1007/s11128-004-3101-5.

[19] R J Schoelkopf and S M Girvin. Wiring up quantum systems. *Nature*, 451(7179): 664–9, February 2008. ISSN 1476-4687. doi: 10.1038/451664a. URL http://www.ncbi.nlm.nih.gov/pubmed/18256662.

[20] A Wallraff, DI Schuster, A Blais, and L Frunzio. Strong coupling of a single photon to a superconducting qubit using circuit quantum electrodynamics. *Nature*, 431(September):162–167, 2004. doi: 10.1038/nature02831.1. URL http://www.nature.com/nature/journal/v431/n7005/abs/nature02851.html.

[21] DI Schuster. *Circuit quantum electrodynamics*. PhD thesis, Yale University, 2007. URL http://adsabs.harvard.edu/abs/2007PhDT.....167S.

[22] S M Girvin, M H Devoret, and R J Schoelkopf. Circuit QED and engineering charge-based superconducting qubits. *Physica Scripta*, T137:014012, December 2009. ISSN 0031-8949. doi: 10.1088/0031-8949/2009/T137/

014012. URL http://stacks.iop.org/1402-4896/2009/i=T137/a=014012?key=crossref.db99a09abacc8f928b9fe1ff634e972d.

[23] Alexandre Blais, Ren-Shou Huang, Andreas Wallraff, S. Girvin, and R. Schoelkopf. Cavity quantum electrodynamics for superconducting electrical circuits: An architecture for quantum computation. *Physical Review A*, 69(6):062320, June 2004. ISSN 1050-2947. doi: 10.1103/PhysRevA.69.062320. URL http://link.aps.org/doi/10.1103/PhysRevA.69.062320.

[24] Mika a Sillanpää, Jae I Park, and Raymond W Simmonds. Coherent quantum state storage and transfer between two phase qubits via a resonant cavity. *Nature*, 449(7161):438–42, September 2007. ISSN 1476-4687. doi: 10.1038/nature06124. URL http://www.ncbi.nlm.nih.gov/pubmed/17898762.

[25] J Majer, J M Chow, J M Gambetta, Jens Koch, B R Johnson, J a Schreier, L Frunzio, D I Schuster, a a Houck, a Wallraff, a Blais, M H Devoret, S M Girvin, and R J Schoelkopf. Coupling superconducting qubits via a cavity bus. *Nature*, 449(7161):443–7, September 2007. ISSN 1476-4687. doi: 10.1038/nature06184. URL http://www.ncbi.nlm.nih.gov/pubmed/17898763.

[26] L DiCarlo, J M Chow, J M Gambetta, Lev S Bishop, B R Johnson, D I Schuster, J Majer, a Blais, L Frunzio, S M Girvin, and R J Schoelkopf. Demonstration of two-qubit algorithms with a superconducting quantum processor. *Nature*, 460 (7252):240–4, July 2009. ISSN 1476-4687. doi: 10.1038/nature08121. URL http://www.ncbi.nlm.nih.gov/pubmed/19561592.

[27] a a Houck, D I Schuster, J M Gambetta, J a Schreier, B R Johnson, J M Chow, L Frunzio, J Majer, M H Devoret, S M Girvin, and R J Schoelkopf. Generating single microwave photons in a circuit. *Nature*, 449(7160):328–31, September 2007. ISSN 1476-4687. doi: 10.1038/nature06126. URL http://www.ncbi.nlm.nih.gov/pubmed/17882217.

[28] L Dicarlo, M D Reed, L Sun, B R Johnson, J M Chow, J M Gambetta, L Frunzio, S M Girvin, M H Devoret, and R J Schoelkopf. Preparation and measurement of three-qubit entanglement in a superconducting circuit. *Nature*, 467(7315):574–8, September 2010. ISSN 1476-4687. doi: 10.1038/nature09416. URL http://www.ncbi.nlm.nih.gov/pubmed/20882013.

[29] D I Schuster, a a Houck, J a Schreier, a Wallraff, J M Gambetta, a Blais, L Frunzio, J Majer, B Johnson, M H Devoret, S M Girvin, and R J Schoelkopf. Resolving photon number states in a superconducting circuit. *Nature*, 445(7127):515–8, February 2007. ISSN 1476-4687. doi: 10.1038/nature05461. URL http://www.ncbi.nlm.nih.gov/pubmed/17268464.

[30] T. Frey, P. J. Leek, M. Beck, a. Blais, T. Ihn, K. Ensslin, and a. Wallraff. Dipole Coupling of a Double Quantum Dot to a Microwave Resonator. *Physical Review Letters*, 108(4):046807, January 2012. ISSN 0031-9007. doi: 10.1103/PhysRevLett.108.046807. URL http://link.aps.org/doi/10.1103/PhysRevLett.108.046807.

[31] M. R. Delbecq, V. Schmitt, F. D. Parmentier, N. Roch, J. J. Viennot, G. Fève, B. Huard, C. Mora, a. Cottet, and T. Kontos. Coupling a Quantum Dot, Fermionic Leads, and a Microwave Cavity on a Chip. *Physical Review Letters*, 107(25): 256804, December 2011. ISSN 0031-9007. doi: 10.1103/PhysRevLett.107.256804. URL http://link.aps.org/doi/10.1103/PhysRevLett.107.256804.

[32] D. I. Schuster, a. P. Sears, E. Ginossar, L. DiCarlo, L. Frunzio, J. J. L. Morton, H. Wu, G. a. D. Briggs, B. B. Buckley, D. D. Awschalom, and R. J. Schoelkopf. High-Cooperativity Coupling of Electron-Spin Ensembles to Superconducting Cavities. *Physical Review Letters*, 105(14):140501, September 2010. ISSN 0031-9007. doi: 10.1103/PhysRevLett.105.140501. URL http://link.aps.org/doi/10.1103/PhysRevLett.105.140501.

[33] T Rocheleau, T Ndukum, C Macklin, J B Hertzberg, a a Clerk, and K C Schwab. Preparation and detection of a mechanical resonator near the ground state of motion. *Nature*, 463(7277):72–5, January 2010. ISSN 1476-4687. doi: 10.1038/nature08681. URL http://www.ncbi.nlm.nih.gov/pubmed/20010604.

[34] C. a. Regal, J. D. Teufel, and K. W. Lehnert. Measuring nanomechanical motion with a microwave cavity interferometer. *Nature Physics*, 4(7):555–560, May 2008. ISSN 1745-2473. doi: 10.1038/nphys974. URL http://www.nature.com/doifinder/10.1038/nphys974.

[35] David M. Pozar. *Microwave engineering*. Wiley, 1997. ISBN 0471170968. URL http://books.google.com/books?id=IDxTAAAAMAAJ&pgis=1.

[36] L. Frunzio, a. Wallraff, D. Schuster, J. Majer, and R. Schoelkopf. Fabrication and Characterization of Superconducting Circuit QED Devices for Quantum Computation. *IEEE Transactions on Appiled Superconductivity*, 15(2):860–863, June 2005. ISSN 1051-8223. doi: 10.1109/TASC.2005.850084. URL http://ieeexplore.ieee.org/lpdocs/epic03/wrapper.htm?arnumber=1439774.

[37] M. Goppl, a. Fragner, M. Baur, R. Bianchetti, S. Filipp, J. M. Fink, P. J. Leek, G. Puebla, L. Steffen, and a. Wallraff. Coplanar waveguide resonators for circuit quantum electrodynamics. *Journal of Applied Physics*, 104(11):113904, 2008. ISSN 00218979. doi: 10.1063/1.3010859. URL http://link.aip.org/link/JAPIAU/v104/i11/p113904/s1&Agg=doi.

[38] Brian C. Wadell. *Transmissión line design handbook*. Artech House, 1991. ISBN 0890064369. URL http://books.google.com/books?id=MyxTAAAAMAAJ&pgis=1.

[39] K. Yoshida, K. Watanabe, T. Kisu, and K. Enpuku. Evaluation of magnetic penetration depth and surface resistance of superconducting thin films using coplanar waveguides. *IEEE Transactions on Appiled Superconductivity*, 5(2): 1979–1982, June 1995. ISSN 10518223. doi: 10.1109/77.402973. URL http://ieeexplore.ieee.org/lpdocs/epic03/wrapper.htm?arnumber=402973.

[40] Michael Tinkham. *Introduction to Superconductivity: Second Edition*. Dover Publications, Incorporated, 2012. ISBN 0486134725. URL http://books.google.com/books?id=VpUk3NfwDIkC&pgis=1.

[41] Charles Kittel. *Introduction to solid state physics*. Wiley, 1996. ISBN 0471111813. URL http://books.google.com/books?id=1X8pAQAAMAAJ&pgis=1.

[42] BA Mazin. *Microwave Kinetic Inductance Detectors*. PhD thesis, California Institute of Technology, 2005. URL http://adsabs.harvard.edu/abs/2005PhDT.....5M.

[43] Gheorghe Stan, Stuart Field, and John Martinis. Critical Field for Complete Vortex Expulsion from Narrow Superconducting Strips. *Physical Review Letters*, 92(9):1–4, March 2004. ISSN 0031-9007. doi: 10.1103/PhysRevLett.92.097003. URL http://link.aps.org/doi/10.1103/PhysRevLett.92.097003.

[44] C. Song, T. Heitmann, M. DeFeo, K. Yu, R. McDermott, M. Neeley, John Martinis, and B. Plourde. Microwave response of vortices in superconducting thin films of Re and Al. *Physical Review B*, 79(17):1–9, May 2009. ISSN 1098-0121. doi: 10.1103/PhysRevB.79.174512. URL http://link.aps.org/doi/10.1103/PhysRevB.79.174512.

[45] M P Blencowe and a D Armour. Probing the quantum coherence of a nanomechanical resonator using a superconducting qubit: II. Implementation. *New Journal of Physics*, 10(9):095005, September 2008. ISSN 1367-2630. doi: 10.1088/1367-2630/10/9/095005. URL http://stacks.iop.org/1367-2630/10/i=9/a=095005?key=crossref.7c25fa93f215b956cfcd8f2a95eeff2f.

[46] Fei Chen, a. J. Sirois, R. W. Simmonds, and a. J. Rimberg. Introduction of a dc bias into a high-Q superconducting microwave cavity. *Applied Physics Letters*,

98(13):132509, January 2011. ISSN 00036951. doi: 10.1063/1.3573824. URL http://link.aip.org/link/APPLAB/v98/i13/p132509/s1&Agg=doi.

[47] AWR. Microwave Office - RF/Microwave Circuit Design Software, . URL http://www.awrcorp.com/products/microwave-office.

[48] U Fano. Effects of Configuration Interaction on Intensities and Phase Shifts. *Physical Review*, 124(6):1866–1878, December 1961. ISSN 0031-899X. doi: 10.1103/PhysRev.124.1866. URL http://prola.aps.org/abstract/PR/v124/i6/p1866_1http://link.aps.org/doi/10.1103/PhysRev.124.1866.

[49] Hermann Grabert and Michel H. Devoret. *Single charge tunneling: Coulomb blockade phenomena in nanostructures*. Plenum Press, 1992. ISBN 0306442299. URL http://books.google.com/books?id=5mEsAAAAYAAJ&pgis=1.

[50] B.D. Josephson. Supercurrents through barriers. *Advances in Physics*, 14(56): 419–451, October 1965. ISSN 0001-8732. doi: 10.1080/00018736500101091. URL http://dx.doi.org/10.1080/00018736500101091.

[51] B.D. Josephson. Possible new effects in superconductive tunnelling. *Physics Letters*, 1(7):251–253, July 1962. ISSN 00319163. doi: 10.1016/0031-9163(62)91369-0. URL http://dx.doi.org/10.1016/0031-9163(62)91369-0.

[52] A Cottet. Implementation of a quantum bit in a superconducting circuit. *PhD thesisUniversité Paris VI*, 2002. URL http://scholar.google.com/scholar?hl=en&btnG=Search&q=intitle:Implementation+of+a+quantum+bit+in+a+superconducting+circuit#1.

[53] Vinay Ambegaokar and Alexis Baratoff. Tunneling Between Superconductors. *Physical Review Letters*, 10(11):486–489, June 1963. ISSN 0031-9007. doi: 10.1103/PhysRevLett.10.486. URL http://link.aps.org/doi/10.1103/PhysRevLett.10.486.

[54] SL Pohlen. *The superconducting single-electron transistor*. PhD thesis, Harvard University, 1999. URL http://adsabs.harvard.edu/abs/1999PhDT.....189P.

[55] T. Fulton, P. Gammel, D. Bishop, L. Dunkleberger, and G. Dolan. Observation of combined Josephson and charging effects in small tunnel junction circuits. *Physical Review Letters*, 63(12):1307–1310, September 1989. ISSN 0031-9007. doi: 10.1103/PhysRevLett.63.1307. URL http://link.aps.org/doi/10.1103/PhysRevLett.63.1307.

[56] M P Blencowe, J Imbers, and a D Armour. Dynamics of a nanomechanical resonator coupled to a superconducting single-electron transistor. *New Journal of Physics*, 7:236–236, November 2005. ISSN 1367-2630. doi: 10.1088/1367-2630/7/1/236. URL http://stacks.iop.org/1367-2630/7/i=1/a=236?key=crossref.dd86ce691052cc6c0d9229b373c23ced.

[57] Zhongqing Ji. *Towards the Quantum Limit : A Single Electron Transistor Analysis*. PhD thesis, Rice University, 2008. URL http://adsabs.harvard.edu/abs/2008PhDT.....25J.

[58] D. V. Averin and K. K. Likharev. *Mesoscopic phenomena in solids*. North-Holland Publ., 1991. ISBN 0444884548. URL http://books.google.com/books?id=CJFlQgAACAAJ&pgis=1.

[59] Mika Sillanpää. *Quantum Device Applications of Mesoscopic Superconductivity*. PhD thesis, Helsinki University of Technology, 2005.

[60] Mika Sillanpää, Leif Roschier, and Pertti Hakonen. Inductive Single-Electron Transistor. *Physical Review Letters*, 93(6):2–5, August 2004. ISSN 0031-9007. doi: 10.1103/PhysRevLett.93.066805. URL http://link.aps.org/doi/10.1103/PhysRevLett.93.066805.

[61] Joel Stettenheim, Madhu Thalakulam, Feng Pan, Mustafa Bal, Zhonqing Ji, Wei-wei Xue, Loren Pfeiffer, K W West, M P Blencowe, and a J Rimberg. A macroscopic mechanical resonator driven by mesoscopic electrical back-action. *Nature*, 466(7302):86–90, July 2010. ISSN 1476-4687. doi: 10.1038/nature09123. URL http://www.ncbi.nlm.nih.gov/pubmed/20596016.

[62] Miles Blencowe, Andrew Armour, and Alex Rimberg. Quantum-classical correspondence for a dc-biased cavity resonator–Cooper-pair transistor system. *. . . : From Nanomechanics to . . .*, pages 1–35, June 2011. URL http://books.google.com/books?hl=en&lr=&id=vt9PAFCwbT8C&oi=fnd&pg=PA33&dq=Quantum-classical+correspondence+for+a+dc-biased+cavity+resonator%E2%80%93Cooper-pair+transistor+system&ots=GIBqspspXo&sig=MAxgeHO_CiMii77ANhePLZ4Kic4http://arxiv.org/abs/1106.5945.

[63] Miles Blencowe and Erind Brahimi. Notes on the CPT-Cavity System. *Unpublished*.

[64] Todd I. Smith. Superconducting microwave cavities and Josephson junctions. *Journal of Applied Physics*, 45(4):1875, April 1974. ISSN 00218979. doi: 10.1063/1.1663507. URL http://link.aip.org/link/?JAPIAU/45/1875/1.

[65] J. E. Zimmerman. Recent Developments in Superconducting Devices. *Journal of Applied Physics*, 42(1):30, January 1971. ISSN 00218979. doi: 10.1063/1.1659587. URL http://link.aip.org/link/?JAPIAU/42/30/1.

[66] N. Werthamer and Sidney Shapiro. Analog-Computer Studies of Josephson Radiation Effects. *Physical Review*, 164(2):523–535, December 1967. ISSN 0031-899X. doi: 10.1103/PhysRev.164.523. URL http://link.aps.org/doi/10.1103/PhysRev.164.523.

[67] O Astafiev, K Inomata, a O Niskanen, T Yamamoto, Yu a Pashkin, Y Nakamura, and J S Tsai. Single artificial-atom lasing. *Nature*, 449(7162):588–90, October 2007. ISSN 1476-4687. doi: 10.1038/nature06141. URL http://www.ncbi.nlm.nih.gov/pubmed/17914393.

[68] M. Hofheinz, F. Portier, Q. Baudouin, P. Joyez, D. Vion, P. Bertet, P. Roche, and D. Esteve. Bright Side of the Coulomb Blockade. *Physical Review Letters*, 106 (21):217005, May 2011. ISSN 0031-9007. doi: 10.1103/PhysRevLett.106.217005. URL http://link.aps.org/doi/10.1103/PhysRevLett.106.217005.

[69] JB Hertzberg. *BACK-ACTION EVADING MEASUREMENTS OF NANOMECHANICAL MOTION APPROACHING QUANTUM LIMITS*. PhD thesis, University of Maryland, College Park in, 2009. URL http://adsabs.harvard.edu/abs/2009PhDT.....193H.

[70] Avago. AppCAD. URL http://www.hp.woodshot.com/.

[71] AWR. TX-Line: Transmission Line Calculator, . URL http://www.awrcorp.com/products/optional-products/tx-line-transmission-line-calculator.

[72] ANSYS. ANSYS Maxwell. URL http://www.ansys.com/Products/Simulation+Technology/Electromagnetics/Electromechanical+Design/ANSYS+Maxwell.

[73] Sonnet. EM Analysis and Simulation - High Frequency Electromagnetic Software Solutions- Sonnet Software. URL http://www.sonnetsoftware.com/.

[74] A J Rimberg. Mapping a DC-Biased Cavity Near Resonance onto a Simple Lumped Model. *Unpublished*.

[75] C.P. Yue. *ON-CHIP SPIRAL INDUCTORS FOR SILICON-BASED RADIO-FREQUENCY INTEGRATED CIRCUITS*. PhD thesis, Stanford University, 1998.

[76] CP Yue and SS Wong. On-chip spiral inductors with patterned ground shields for Si-based RF ICs. *Solid-State Circuits, IEEE Journal of*, 33(5):743–752, 1998. URL http://ieeexplore.ieee.org/xpls/abs_all.jsp?arnumber=668989.

[77] S.S. Mohan, M. del Mar Hershenson, S.P. Boyd, and T.H. Lee. Simple accurate expressions for planar spiral inductances. *IEEE Journal of Solid-State Circuits*, 34(10):1419–1424, 1999. ISSN 00189200. doi: 10.1109/4.792620. URL http://ieeexplore.ieee.org/lpdocs/epic03/wrapper.htm?arnumber=792620.

[78] Stanford Microwave Integrated Circuits Laboratory. URL http://www-smirc.stanford.edu/spiralCalc.html.

[79] Wei Lu. *Single-Electron Transistor : Effects of the Environment and Detecting Electron Motion in Real Time*. PhD thesis, Rice University, 2003. URL http://adsabs.harvard.edu/abs/2003PhDT.....76L.

[80] N a Court, a J Ferguson, and R G Clark. Energy gap measurement of nanostructured aluminium thin films for single Cooper-pair devices. *Superconductor Science and Technology*, 21(1):015013, January 2008. ISSN 0953-2048. doi: 10.1088/0953-2048/21/01/015013. URL http://stacks.iop.org/0953-2048/21/i=1/a=015013?key=crossref.20199f399e6c894d7fcab7f775d10389.

[81] W. W. Xue, Z. Ji, Feng Pan, Joel Stettenheim, M. P. Blencowe, and a. J. Rimberg. Measurement of quantum noise in a single-electron transistor near the quantum limit. *Nature Physics*, 5(9):660–664, July 2009. ISSN 1745-2473. doi: 10.1038/nphys1339. URL http://www.nature.com/doifinder/10.1038/nphys1339.

[82] Amuneal. Magnetic Shielding Materials. URL http://amuneal.com/magnetic-shielding/theory-design/magnetic-shielding-materials.

[83] a. I. Lvovsky. Continuous-variable optical quantum-state tomography. *Reviews of Modern Physics*, 81(1):299–332, March 2009. ISSN 0034-6861. doi: 10.1103/RevModPhys.81.299. URL http://link.aps.org/doi/10.1103/RevModPhys.81.299.

[84] George Orwell. *Animal Farm.: A Fairy Story*. Signet Classics, 1996. ISBN 0451526341. URL http://books.google.com/books?id=SGAZdjNfruYC&pgis=1.

[85] C. Eichler, D. Bozyigit, C. Lang, L. Steffen, J. Fink, and a. Wallraff. Experimental State Tomography of Itinerant Single Microwave Photons. *Physical Review Letters*, 106(22):3–6, June 2011. ISSN 0031-9007. doi: 10.1103/PhysRevLett.106.220503. URL http://link.aps.org/doi/10.1103/PhysRevLett.106.220503.

[86] C Eichler, D Bozyigit, and A Wallraff. Characterizing Quantum Microwave Radiation and its Entanglement with Superconducting Qubits using Linear Detectors. pages 1–14, 2012.

[87] M. Kim. Quasiprobability functions measured by photon statistics of amplified signal fields. *Physical Review A*, 56(4):3175–3179, October 1997. ISSN 1050-2947. doi: 10.1103/PhysRevA.56.3175. URL http://link.aps.org/doi/10.1103/PhysRevA.56.3175.

[88] Z Hradil. Quantum-state estimation. *Physical Review A*, 55(3):1561–1564, 1997. URL http://link.aps.org/doi/10.1103/PhysRevA.55.R1561.

[89] J. eháček, Z. Hradil, and M. Ježek. Iterative algorithm for reconstruction of entangled states. *Physical Review A*, 63(4):1–4, March 2001. ISSN 1050-2947.

doi: 10.1103/PhysRevA.63.040303. URL http://link.aps.org/doi/10.1103/PhysRevA.63.040303.

[90] D. Mogilevtsev, J. eháček, and Z. Hradil. Objective approach to biased tomography schemes. *Physical Review A*, 75(1):1–14, January 2007. ISSN 1050-2947. doi: 10.1103/PhysRevA.75.012112. URL http://link.aps.org/doi/10.1103/PhysRevA.75.012112.

[91] Z. Hradil, D. Mogilevtsev, and J. eháček. Biased Tomography Schemes: An Objective Approach. *Physical Review Letters*, 96(23):1–4, June 2006. ISSN 0031-9007. doi: 10.1103/PhysRevLett.96.230401. URL http://link.aps.org/doi/10.1103/PhysRevLett.96.230401.

[92] Jaroslav eháček, Zdeněk Hradil, E. Knill, and a. Lvovsky. Diluted maximum-likelihood algorithm for quantum tomography. *Physical Review A*, 75(4):1–5, April 2007. ISSN 1050-2947. doi: 10.1103/PhysRevA.75.042108. URL http://link.aps.org/doi/10.1103/PhysRevA.75.042108.

[93] DISCOVERY. DISCOVERY Home. URL http://discovery.dartmouth.edu:8080/display/Discovery/DISCOVERY+Home.

[94] QuTiP. QuTiP - Quantum Toolbox in Python. URL http://code.google.com/p/qutip/.

[95] W. Lu, K. Maranowski, and a. Rimberg. Charge transport processes in a superconducting single-electron transistor coupled to a microstrip transmission line. *Physical Review B*, 65(6):2–5, January 2002. ISSN 0163-1829. doi: 10.1103/PhysRevB.

65.060501. URL http://link.aps.org/doi/10.1103/PhysRevB.65.060501.

[96] YA Pashkin, H Im, and J Leppäkangas. Charge transport through ultrasmall single and double Josephson junctions coupled to resonant modes of the electromagnetic environment. *Physical Review B*, 020502(83):020502, 2010. doi: 10.1103/PhysRevB.83.020502. URL http://arxiv.org/abs/1010.3617.

[97] P.-M. Billangeon, F. Pierre, H. Bouchiat, and R. Deblock. ac Josephson Effect and Resonant Cooper Pair Tunneling Emission of a Single Cooper Pair Transistor. *Physical Review Letters*, 98(21):1–4, May 2007. ISSN 0031-9007. doi: 10.1103/PhysRevLett.98.216802. URL http://link.aps.org/doi/10.1103/PhysRevLett.98.216802.

[98] Sidney Shapiro. Josephson Currents in Superconducting Tunneling: The Effect of Microwaves and Other Observations. *Physical Review Letters*, 11(2):80–82, July 1963. ISSN 0031-9007. doi: 10.1103/PhysRevLett.11.80. URL http://link.aps.org/doi/10.1103/PhysRevLett.11.80.

[99] D. D. Coon and M. D. Fiske. Josephson ac and Step Structure in the Supercurrent Tunneling Characteristic. *Physical Review*, 138(3A):A744–A746, May 1965. ISSN 0031-899X. doi: 10.1103/PhysRev.138.A744. URL http://link.aps.org/doi/10.1103/PhysRev.138.A744.

[100] MILAN FISKE. Temperature and Magnetic Field Dependences of the Josephson Tunneling Current. *Reviews of Modern Physics*, 36(1):221–222, January 1964.

ISSN 0034-6861. doi: 10.1103/RevModPhys.36.221. URL http://link.aps.org/doi/10.1103/RevModPhys.36.221.

[101] D. Rodrigues, J. Imbers, and a. Armour. Quantum Dynamics of a Resonator Driven by a Superconducting Single-Electron Transistor: A Solid-State Analogue of the Micromaser. *Physical Review Letters*, 98(6):1–4, February 2007. ISSN 0031-9007. doi: 10.1103/PhysRevLett.98.067204. URL http://link.aps.org/doi/10.1103/PhysRevLett.98.067204.

[102] M. Marthaler, Gerd Schön, and Alexander Shnirman. Photon-Number Squeezing in Circuit Quantum Electrodynamics. *Physical Review Letters*, 101(14):147001, September 2008. ISSN 0031-9007. doi: 10.1103/PhysRevLett.101.147001. URL http://link.aps.org/doi/10.1103/PhysRevLett.101.147001.

[103] Michael Marthaler, Juha Leppäkangas, and Jared H. Cole. Lasing, trapping states, and multistability in a circuit quantum electrodynamical analog of a single-atom injection maser. *Physical Review B*, 83(18):180505, May 2011. ISSN 1098-0121. doi: 10.1103/PhysRevB.83.180505. URL http://link.aps.org/doi/10.1103/PhysRevB.83.180505.

[104] Andrew Armour. Theoretical description of the CPT-cavity system Hamiltonian. *Unpublished*, 2013.

[105] K D Petersson, L W McFaul, M D Schroer, M Jung, J M Taylor, A A Houck, and J R Petta. Circuit quantum electrodynamics with a spin qubit. *Nature*, 490

(7420):380–3, October 2012. ISSN 1476-4687. doi: 10.1038/nature11559. URL http://dx.doi.org/10.1038/nature11559.

[106] J D Teufel, Dale Li, M S Allman, K Cicak, a J Sirois, J D Whittaker, and R W Simmonds. Circuit cavity electromechanics in the strong-coupling regime. *Nature*, 471(7337):204–8, March 2011. ISSN 1476-4687. doi: 10.1038/nature09898. URL http://www.ncbi.nlm.nih.gov/pubmed/21390127.